

**NASA Technical Memorandum 104559**

**NASA Sea Ice Validation Program for  
the Defense Meteorological Satellite  
Program Special Sensor Microwave  
Imager: Final Report**

**Donald J. Cavalieri, Editor**  
*Goddard Space Flight Center*  
*Greenbelt, Maryland*



National Aeronautics and  
Space Administration

**Goddard Space Flight Center**  
Greenbelt, MD  
1992



## CONTRIBUTORS

Donald J. Cavalieri  
Laboratory for Hydrospheric Processes  
NASA Goddard Space Flight Center  
Greenbelt, Maryland 20771

John P. Crawford  
Jet Propulsion Laboratory  
California Institute of Technology  
Pasadena, California 91109

Mark R. Drinkwater  
Jet Propulsion Laboratory  
California Institute of Technology  
Pasadena, California 91109

William J. Emery  
Colorado Center for Astrodynamics Research  
University of Colorado  
Boulder, Colorado 80309

Duane T. Eppler  
Naval Oceanographic and Atmospheric  
Research Laboratory  
Hanover, New Hampshire 03755

L. Dennis Farmer  
Naval Oceanographic and Atmospheric  
Research Laboratory  
Hanover, New Hampshire 03755

Charles W. Fowler  
Colorado Center for Astrodynamics Research  
University of Colorado  
Boulder, Colorado 80309

Mark Goodberlet  
Department of Electrical and  
Computer Engineering  
University of Massachusetts  
Amherst, Massachusetts 01003

Robert R. Jentz  
Environmental Research Institute of Michigan  
Ann Arbor, Michigan 48107

Andrew Milman  
Environmental Research Institute of Michigan  
Ann Arbor, Michigan 48107

Charles S. Morris  
Jet Propulsion Laboratory  
California Institute of Technology  
Pasadena, California 91109

Robert G. Onstott  
Environmental Research Institute of Michigan  
Ann Arbor, Michigan 48107

Axel J. Schweiger  
Cooperative Institute for Research in Environmental  
Sciences  
University of Colorado  
Boulder, Colorado 80302

Robert Shuchman  
Environmental Research Institute of Michigan  
Ann Arbor, Michigan 48107

Konrad Steffen  
Cooperative Institute for Research in Environmental  
Sciences  
University of Colorado  
Boulder, Colorado 80302

Calvin T. Swift  
Department of Electrical and Computer Engineering  
University of Massachusetts  
Amherst, Massachusetts 01003

Chris C. Wacherman  
Environmental Research Institute of Michigan  
Ann Arbor, Michigan 48107

Ronald L. S. Weaver  
National Snow and Ice Data Center  
University of Colorado  
Boulder, Colorado 80302



## EXECUTIVE SUMMARY

In 1982, NASA established a program to process, archive, and distribute to the user community gridded Defense Meteorological Satellite Program (DMSP) Special Sensor Microwave/Imager (SSM/I) microwave radiances and derived sea ice concentrations for both polar regions. A key element of this effort was the initiation of a sea ice validation program in 1987 for the purpose of providing the user with a measure of the precision and accuracy of the derived sea ice products. Sea ice remote sensing specialists were invited to serve on the NASA sea ice validation team to define and implement the program. A parallel program, which included additional geophysical parameters, was established by the Department of Defense under the leadership of Dr. James P. Hollinger at the Naval Research Laboratory (NRL). This report summarizes the results of the NASA sea ice validation program, including a description of the SSM/I calibration and geolocation correction procedures, distribution of SSM/I data on polar grids, and the results of satellite and aircraft sea ice parameter comparisons.

The objective of the NASA validation program and the approach taken to meet this objective are outlined in Chapter 1. The objective was to establish quantitative relationships between the sea ice parameters derived from the SSM/I using the NASA Team sea ice algorithm and those same parameters derived from other sources covering as many geographical areas as possible for different seasons. These sea ice parameters include the location of the ice edge, the total sea ice concentration for both north and south polar regions, and the multiyear sea ice concentration for the north polar region only. The ancillary data sets used in the validation consist of visible and infrared imagery from the Advanced Very High Resolution Radiometer (AVHRR) on the National Oceanic and Atmospheric Administration (NOAA) satellites, the Multispectral Scanner (MSS) on Landsat, and high-resolution active and passive microwave imagery from coordinated NASA and Navy aircraft underflights over regions of the Bering, Beaufort, and Chukchi seas in March 1988.

A summary of the SSM/I instrument characteristics and calibration is provided in Chapter 2. The first SSM/I was launched on DMSP F-8 in June 1987. A second and third SSM/I were launched on DMSP F-10 in December 1990 and on DMSP F-11 in November 1991. The SSM/I measures microwave radiances at 19.4, 37.0, and 85.5 GHz at horizontal and vertical polarizations, and at 22.2 GHz at vertical polarization only. The sensor, operating from a near-polar orbit, conically scans the surface of the earth, providing a swath width of 1400 km, and thus provides near-global coverage every day. The spatial resolution in kilometers (along- x cross-track) of the sensor varies with frequency ranging from 69 x 43 at 19.4 GHz to 15 x 13 at 85.5 GHz.

Analysis of the DMSP F-8 SSM/I data at NRL showed that the SSM/I radiometer sensitivity is very good with the noise equivalent temperature differential less than 0.75 K for the lowest three frequencies. Since the instrument was turned back on in January 1988 after being shut off in December 1987, the 85-GHz channels have degraded significantly with large increases in the noise equivalent temperature differential, presumably because of problems associated with instrument heating effects. Except for the 85-GHz channels, the SSM/I absolute calibration is also quite good and is estimated to be within 2 to 4 K, which is consistent with the  $\pm 3$  K obtained by the NRL group. Initial problems with geolocation have been partly rectified, and correction algorithms provide geolocation to an accuracy estimated to be better than 10 km, although larger errors may occur occasionally.

The processing and distribution of the SSM/I data and sea ice products are described in Chapter 3. The SSM/I data are received at the Navy Fleet Numerical Oceanography Center (FNOC), where initial processing takes place before the data are sent to NOAA NESDIS Satellite Data Services Division for archival and distribution of antenna temperature, brightness temperature, and Navy-produced environmental data records. The antenna temperature data are received by Remote Sensing Systems, Inc. where they are converted into a compact format and distributed to the National Snow and Ice Data Center (NSIDC) through the WETNET organization at NASA Marshall Space Flight Center in Huntsville, Alabama. At NSIDC brightness temperatures are converted into sea ice products, and both gridded brightness temperatures and sea ice parameters are distributed on compact discs.

The algorithm used to convert from SSM/I radiances to sea ice concentrations is the NASA Team algorithm, which was also used to process the Nimbus 7 SMMR data set, and is described in Chapter 4. The input radiances to the

algorithm are from the SSM/I 19.4-GHz H and V, and the 37.0-GHz V channels. These radiances are used to calculate two ratios of radiances which are then used as the algorithm independent variables. The two output parameters are the total sea ice concentration and the multiyear ice concentration. A weather filter is used to reduce spurious sea ice concentrations that result from wind-roughened seas, and atmospheric microwave emission from cloud liquid water and atmospheric water vapor over areas of ice-free ocean. While the weather filter is particularly effective at polar latitudes during winter, the filter eliminates sea ice concentrations less than 15% - corresponding, on average, to the position of the outer ice bands at the ice edge.

Satellite and aircraft comparisons that serve as the basis for the validation of the NASA SSM/I sea ice parameters are presented in Chapters 5 through 9. In Chapter 5, the results of over 100 SSM/I-Landsat total ice concentration comparisons spanning all four seasons and covering areas in both the Arctic and Antarctic are described. The estimated accuracy of the Landsat ice concentrations is 4%. The SSM/I-Landsat comparisons reveal that under winter conditions the SSM/I accuracy is 7% with a negative bias of 4% indicating that the SSM/I underestimates sea ice concentration relative to Landsat. Although larger errors were found to occur during summer when melt conditions bias the calculations, the summer comparisons themselves are suspect because of errors in Landsat-SSM/I data registration caused by ice motion during the time between SSM/I and Landsat overpasses. In all the Landsat comparisons, higher accuracy was obtained through the use of locally defined algorithm tie-points.

Comparisons between SSM/I sea ice concentrations and concentrations obtained with the AVHRR on the NOAA 9 and 10 satellites are presented in Chapter 6. Three different techniques were used to derive sea ice concentrations from the AVHRR imagery. The fact that these techniques lead to very different concentrations underscores the considerable uncertainty in the precision and accuracy of current AVHRR ice concentration algorithms. Previous work has also shown that the root-mean-square differences between coincident AVHRR and Landsat MSS sea ice concentrations range from 7% to 18%. Uncertainties of this magnitude severely limit the usefulness of AVHRR as a validation tool for the SSM/I.

Results from the NASA and Navy SSM/I aircraft underflights are provided in Chapters 7, 8, and 9. The validity of using high-resolution, active and passive microwave images from aircraft underflights for validating multiyear sea ice concentrations over areas as large as SSM/I footprints is established in Chapter 7. In addition, coincident data from the GSFC fixed-beam aircraft multifrequency microwave radiometers (AMMR) and the JPL synthetic aperture radar (SAR) on the NASA DC-8, and from the Naval Oceanographic and Atmospheric Research Laboratory (NOARL) Ka-band Radiometer Mapping System (KRMS) imaging radiometer on the NRL P-3 were used to verify that the SSM/I correctly maps the large-scale multiyear (MY) ice distribution in the central Arctic, including zones of first-year (FY) ice, mixed FY and MY ice, and mostly MY ice. Relative to the KRMS multiyear concentrations, both the SSM/I and the AMMR with the NASA Team algorithm gave concentrations up to 25% over areas of FY ice, but gave lower concentrations in a shear zone north of Ellesmere Island. These differences are discussed in the context of the character of the ice as deduced from the KRMS imagery. The correlation between the MY sea ice concentrations derived from spatially and temporally coincident radiances and backscatter intensities from the GSFC AMMR and JPL SAR for a region in the Beaufort Sea was 0.89. The mean  $\pm 1$  standard deviation (SD) difference was  $-6\% \pm 14\%$ , indicating that the AMMR concentrations derived from an SSM/I type algorithm gave lower concentrations on average.

Bering Sea ice-edge crossings made with the NASA DC-8, which carried two global positioning system (GPS) receivers, provided the precise location of ice-edge features required for determining the appropriate SSM/I ice concentration contour to use for locating the ice edge on the SSM/I grid. On average, the SSM/I ice concentration for the grid containing the initial ice band is about 15%, whereas the concentration corresponding to the position of the main pack is about 38%. This result suggests that the SSM/I 15% ice-concentration contour, on average, locates the outer ice-edge position, defined as the location of the initial ice band. These results also suggest that the use of the spectral gradient ratio (GR) weather filter, which eliminates ice concentrations of less than 15% on SSM/I grid maps, really eliminates only the spurious ice concentrations associated with the smearing of the ice edge by the finite width of the SSM/I antenna pattern.

Direct comparisons of total and MY ice concentrations derived from the KRMS imagery with the corresponding SSM/I values are presented in Chapter 8, and direct comparisons using the Naval Air Development Center (NADC)/Environmental Research Institute of Michigan (ERIM) C-band SAR are presented in Chapter 9. For total ice cover, the mean difference between aircraft concentrations (consistently 100%) and those calculated from the SSM/I radiances is  $-2.4\% \pm 2.4\%$ , which is consistent with the results obtained from the March 1988 Landsat-SSM/I comparisons ( $-2.1\% \pm 3.1\%$ ) for the same region. Comparison of SSM/I and aircraft MY concentrations shows that the NASA SSM/I algorithm overestimates MY ice concentration by  $12\% \pm 11\%$ , on average, in the Chukchi and Beaufort seas. Spurious MY ice concentrations of up to 25% are found in areas of known FY ice. From the direct comparisons between aircraft and SSM/I, the overall accuracy of MY ice concentration is taken to be 11%. Potential causes for this large uncertainty include the variability of MY ice emissivity, metamorphized snow cover over FY ice, and residual physical temperature dependency of the GR parameter.

Based both on the results of the NASA multisensor validation effort and on user community feedback, several algorithm problems have been identified (Chapter 10). These problems arise from two basic sources of error. The first source is the sensitivity of the 19.35 GHz SSM/I channels to atmospheric water vapor. The algorithm weather filter is less effective for the SSM/I than it was for the Nimbus 7 SMMR because the SSM/I 19.35 GHz channels are closer to the peak of the 22.2 GHz water vapor line than are the 18.0 GHz SMMR channels. During winter, the weather-related errors are most pronounced at low latitudes, but are serious at all latitudes during summer. The second source of error results from the inability of the algorithm to distinguish more than two radiometrically different sea ice types and ice-surface conditions.

It is strongly recommended that a focused effort be made to address these problems using existing data sets and, if needed, newly acquired field and laboratory data. Specific goals include algorithm corrections for: (1) false indications of sea ice over open ocean and near the ice edge at high latitudes during summer, (2) negative biases in sea ice concentration resulting from the presence of new and young sea ice types, (3) false indications of multiyear ice concentration resulting from a deep or aged snow cover and from variable surface conditions, and (4) negative biases in summer ice concentration resulting from the presence of melt ponds. Potential for achieving these goals exists through the use of additional SSM/I channels in the algorithm and of combined SSM/I and ERS-1 SAR spaceborne observations that have recently become available.



## PREFACE

This document summarizes the results of the NASA Sea Ice Validation Program for the DMSP SSM/I. The successful completion of this program is the result of the efforts of the contributors to this report and to many other individuals cited in the acknowledgements. A parallel SSM/I Calibration/Validation Program had been established by the Department of Defense under the leadership of Dr. James P. Hollinger at NRL. During the first year of SSM/I operation, both teams focused on monitoring sensor performance and quality control of the SSM/I data and shared information and compared notes, particularly on the early work related to sensor calibration and geolocation error corrections.

The first three chapters of this report provide a description of the SSM/I, the calibration and geolocation correction procedures implemented by NASA, and a summary of the flow of SSM/I data from satellite to the NSIDC, which distributes the NASA-processed data to the research community. The next six chapters are devoted to a description of the NASA Team SSM/I sea ice algorithm used for processing the SSM/I data set and to the major comparative studies utilizing Landsat and NOAA satellite imagery and aircraft data from coordinated NASA and Navy SSM/I underflights. The last chapter provides a summary of the accuracy of the NASA sea ice parameters, identifies needed algorithm improvements, and makes recommendations for additional validation studies.

The sea ice validation results reported here provide the most comprehensive measure, to date, of the accuracy of sea ice parameters derived from a single sensor with a single processing sea ice algorithm. The Landsat-SSM/I comparisons, in particular, provide a high level of confidence in the use of the SSM/I total ice concentrations for climatologic and large-scale oceanographic studies. This confidence is based on over 100 comparisons covering regions in both the Arctic and Antarctic and spanning all four seasons. The results presented in this report can also be extended to the Nimbus 7 SMMR sea ice data set, since an independent study has shown that concentration differences (SMMR-SSM/I) during the 2 months of SMMR and SSM/I overlap are  $0.2\% \pm 2.5\%$  during the austral winter and  $0.5\% \pm 5\%$  during boreal summer. It is hoped that this measure of consistency will encourage the further use of these data, which provide well over a decade of continuous, global sea ice measurements.

The NASA Sea Ice Validation Program for the DMSP SSM/I was sponsored by the NASA Oceanic Processes Branch, NASA Headquarters, Washington, D.C., through the support of Drs. Robert Thomas and Kenneth Jezek, who served as Polar Ocean Program Managers during the lifetime of this program.

PRECEDING PAGE BLANK NOT FILMED

## ACKNOWLEDGEMENTS

The authors thank the following individuals for their contribution to the successful completion of this validation program.

**AMES RESEARCH CENTER:** John Reller, Leo DeGreef, Earl Petersen, Dean Jaynes, Bruce Barney, Gordon Hardy, Gene Moniz, and the ground crew of the NASA DC-8 for their full support and cooperation in the planning and execution of each of the SSM/I underflights.

**ENVIRONMENTAL RESEARCH INSTITUTE OF MICHIGAN:** Jim Lyden and Erik Kasischka for assistance and guidance in the planning of the coordination of the NADC P-3 flights with the NASA DC-8.

**GEOPHYSICAL INSTITUTE, UNIVERSITY OF ALASKA, FAIRBANKS:** Cindy Wilson, administrative assistant to Gunter Weller, for assistance in receiving the near-real time SSM/I data.

**JET PROPULSION LABORATORY:** Walt Brown and Tim Miller and their team of engineers for the operation of the JPL SAR on the NASA DC-8.

**NASA GODDARD SPACE FLIGHT CENTER:** Tom Wilheit, Tom Dod, Dick Kutz, and John Fuchs of the Microwave Sensors Branch; Don Williams of Scientific Technology, Inc., for the preparation and operation of the microwave radiometers on the NASA DC-8; Per Gloersen and Steve Schweinfurth for acquiring and processing the near real-time SSM/I sea ice data; Daya Gilra of STX Corp. for postflight calibration of the aircraft radiometer data set.

**NASA OCEAN DATA SYSTEM/JPL:** J. Charles Klose, Carol Miller, Harold Ashby, John Robles, Theodore Pavlovitch, Daniel Bonbright, and Stephen Ritchie for developing the NASA SSM/I processing system.

**NATIONAL SNOW AND ICE DATA CENTER, UNIVERSITY OF COLORADO:** Vince Troisi, David Hendrix, Claire Hanson, Nick Sandoval, Victor Gurule and Roger Barry for contributing significantly to the processing and archiving of the SSM/I data and for the development of the Cryospheric Data Management System.

**NAVAL AIR DEVELOPMENT CENTER:** CDR Feierabend and LCDR Letarte for their cooperation in coordinating the NADC P-3 and NASA DC-8 underflights.

**NAVAL RESEARCH LABORATORY:** CDR Wnuk, LCDR Schoulda, and LCDR Thornburg for their cooperation in coordinating the NRL P-3 and DC-8 underflights.

**NAVAL WEAPONS CENTER:** Bruce Heydlauff for operation and maintenance of the KRMS and related support equipment.

**NAVY/NOAA JOINT ICE CENTER:** Gary Wohl for serving both as weather forecaster and ice observer during each of the underflights.

**NOAA'S OCEAN APPLICATION GROUP:** Otto Steffin and Warren Yogi for providing near-real time SSM/I data during the underflights.

## TABLE OF CONTENTS

### 1. Introduction

Donald J. Cavalieri

1.1 Brief History .....	1
1.2 Validation Objective and Approach .....	1
1.3 References .....	3

### 2. DMSP SSM/I Sensor Description and Calibration

Mark Goodberlet and Calvin T. Swift

2.1 Sensor Description .....	5
2.2 Radiometer Precision and Absolute Accuracy .....	7
2.3 Antenna Pattern Correction .....	11
2.4 Antenna Beam Width and Side Lobe Level .....	12
2.5 Geolocation Problems .....	15
2.6 References .....	20

### 3. DMSP SSM/I Data Processing and Archive

Charles S. Morris and Ronald L. S. Weaver

3.1 Overview .....	21
3.2 SSM/I Data Flow .....	22
3.3 Data Problems .....	22
3.4 Data Archiving Activities .....	23
3.5 References .....	24

### 4. Sea Ice Algorithm

Donald J. Cavalieri

4.1 Algorithm Description .....	25
4.2 SSM/I Tie-points .....	26
4.3 Algorithm Sensitivity and Sources of Error .....	28
4.4 References .....	30

### 5. SSM/I-Landsat Comparison

Konrad Steffen and Axel J. Schweiger

5.1 Landsat Imagery .....	33
5.2 Method .....	34
5.3 Accuracy .....	35
5.4 Ice Classification .....	36
5.5 Results .....	37

5.6 Conclusions .....	44
5.7 References .....	46

## 6. SSM/I-AVHRR Comparison

William J. Emery and Charles W. Fowler

6.1 Introduction .....	47
6.2 AVHRR and SSM/I Imagery .....	47
6.3 Ice-Concentration Methods .....	48
6.4 Sample Images .....	49
6.5 Statistical Comparisons and Conclusions .....	51
6.6 References .....	53

## 7. SSM/I AIRCRAFT UNDERFLIGHTS: Introduction and Aircraft Sensor Comparisons

Donald J. Cavalieri, John P. Crawford, Mark R. Drinkwater,  
Duane T. Eppler, and L. Dennis Farmer

7.1 Introduction .....	55
7.2 Aircraft Instrumentation .....	56
7.3 Aircraft Data Sets .....	57
7.4 Discussion of Results .....	58
7.5 Conclusions .....	66
7.6 References .....	67

## 8. SSM/I AIRCRAFT UNDERFLIGHTS: SSM/I-KRMS Comparison

Duane T. Eppler, L. Dennis Farmer, and Donald J. Cavalieri

8.1 Introduction .....	69
8.2 KRMS Instrument Description .....	69
8.3 SSM/I-KRMS Comparison .....	72
8.4 Discussion .....	76
8.5 Conclusions .....	78
8.6 References .....	79

## 9. SSM/I AIRCRAFT UNDERFLIGHTS: SSM/I-NADC/ERIM SAR Comparison

Robert R. Jentz, Chris C. Wacherman, Robert Shuchman  
Robert G. Onstott, and Andrew Milman

9.1 Introduction .....	81
9.2 NADC/ERIM SAR Instrument and Mission Description .....	81
9.3 SSM/I-SAR Comparison .....	84
9.4 Discussion .....	87

9.5 Conclusions .....	88
9.6 References .....	89

10. Summary, Conclusions, and Recommendations

Donald J. Cavalieri

10.1 Summary and Conclusions .....	91
10.2 Recommendations .....	94
10.3 References .....	95

Appendix A: Geolocation Correction Software

Mark Goodberlet and Calvin T. Swift

A.1 PIXFIX .....	A-1
------------------	-----



## Chapter 1

### INTRODUCTION

Donald J. Cavalieri  
Laboratory for Hydrospheric Processes  
NASA Goddard Space Flight Center  
Greenbelt, Maryland 20771

1.1 Brief History .....	1
1.2 Validation Objective and Approach .....	1
1.3 References .....	3

#### 1.1 Brief History

On June 19, 1987, the Special Sensor Microwave Imager (SSM/I) was launched as part of the Defense Meteorological Satellite Program (DMSP). The SSM/I is a passive microwave imager which operates at four frequencies (19.4, 22.2, 37.0, and 85.5 GHz) with orthogonal (horizontal and vertical) polarizations measured at each frequency except 22 GHz, which has only a vertical polarization channel. Its spatial resolution is frequency-dependent and ranges from about 50 km at 19 GHz to better than 15 km at 85 GHz. With a swath width of almost 1400 km, the SSM/I provides near-global coverage every day. A detailed description of the sensor and its radiometric performance is given by Hollinger et al. (1987). The SSM/I provides the microwave radiances which will extend the record of polar sea ice observations that began with the Nimbus 5 electrically scanning microwave radiometer (ESMR) in 1972 and continued until August 1987 with the Nimbus 7 scanning multichannel microwave radiometer (SMMR).

In recognition of the importance of SSM/I data to the polar science community, NASA established a program to acquire, process, validate and archive both the calibrated SSM/I microwave radiances and the derived sea ice parameters. The NASA Ocean Data System at the Jet Propulsion Laboratory in Pasadena, California was assigned the task of developing software to process and map the sea ice parameters, and of transferring the system to the National Snow and Ice Data Center at the University of Colorado in Boulder, Colorado. Because the determination of the accuracy of the ice parameters is critical to the development of a scientifically useful data set, a key component of the NASA SSM/I program is the validation of the derived ice parameters. A comprehensive validation plan was defined in 1987 (Cavalieri and Swift, 1987) and implemented in 1988 and 1989.

This report summarizes the results of the validation program. Chapter 2 describes the sensor characteristics and details the procedure developed for correcting the SSM/I antenna pattern and for reducing the geolocation error. Chapter 3 provides an update on the processing and archiving of the SSM/I data. Chapter 4 describes briefly the nature of the sea ice algorithm. Chapters 5 and 6 discuss the results from the Landsat MSS and NOAA AVHRR total ice concentration comparisons with the SSM/I. Chapter 7 lays the foundation for the aircraft-SSM/I intercomparisons presented in Chapters 8 and 9. Chapter 8 presents the results of a comparative analysis between high-resolution passive microwave imagery and SSM/I ice concentrations in the Chukchi Sea, while Chapter 9 provides an intercomparison of SAR mosaics and SSM/I ice concentrations in the Beaufort Sea. Finally, Chapter 10 provides a summary of results and a discussion of needed algorithm improvements and additional validation studies.

#### 1.2 Validation Objective and Approach

The objective of the validation program is to establish statistical relationships between the sea ice parameters derived from the SSM/I and those same parameters derived from other data sets covering as many geographical areas as possible for different seasons. These parameters include the position of the sea ice edge and the total sea ice concentration for both northern and southern polar regions and the multiyear sea ice concentration for the northern polar

region only. Monthly-mean sea ice concentrations are illustrated in Color Plates 1 and 2. The underlying philosophy taken in meeting this objective was that confidence in the SSM/I algorithm products is achieved not so much by detailed comparison with localized surface observations as by consistency with independent spatially and temporally coincident data sets.

The approach for meeting the validation objective was one of compiling and analyzing spatially and temporally coincident data sets for comparison with the SSM/I ice parameters. Coincident or nearly coincident observations were obtained from other satellite sensors and from coordinated NASA and Navy aircraft underflights covering several SSM/I footprints. This multisensor/multispacial approach is illustrated schematically in Figure 1.1. Data sets acquired include Landsat MSS and TIROS N AVHRR imagery and high-resolution active and passive microwave data from NASA and Navy aircraft underflights. The spatial resolutions of the comparison data sets range from the 3-m aircraft SAR data, the 80-m MSS Landsat imagery, 100-m (at nadir) aircraft passive microwave imagery, and 1-km resolution of the AVHRR imagery. The SSM/I has spatial resolutions that are wavelength dependent ranging from 15 to 70 km (Table 1.1).

## MULTISENSOR/MULTISPATIAL VALIDATION OF SEA ICE PARAMETERS

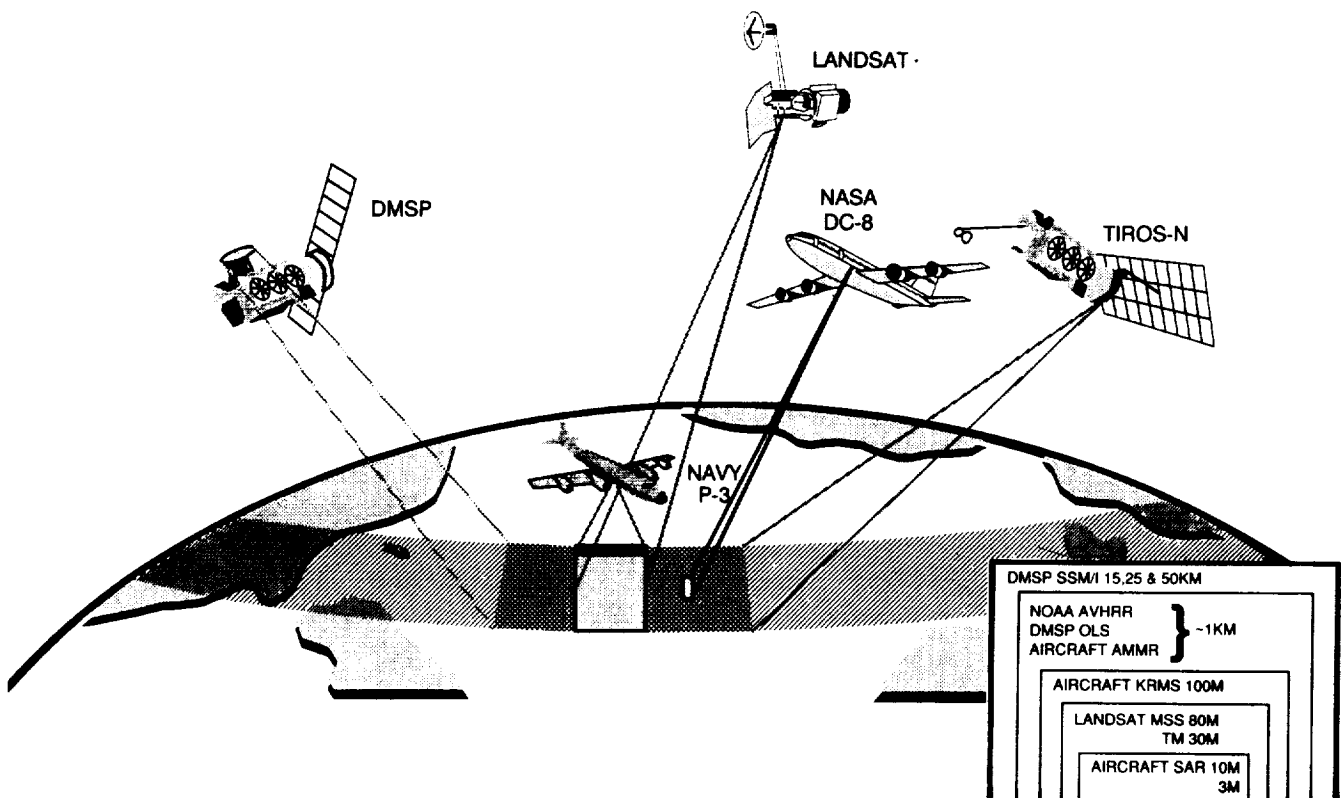


Figure 1.1. A schematic of the multispatial/multisensor validation approach.

Table 1.1. Spatial Resolution of the DMSP SSM/I Channels

SSM/I channel frequency (GHz)	Effective field-of-view (km)	
	Along-track	Cross-track
19.35 (H- and V-pol.)	69	43
22.24 (V-pol.)	50	40
37.0 (H- and V-pol.)	37	29
85.5 (H- and V-pol.)	15	13

### 1.3 References

- Cavalieri, D.J., and C. T. Swift, *NASA Sea Ice and Snow Validation Plan for the Defense Meteorological Satellite Program Special Sensor Microwave/Imager SSM/I*, NASA, NASA Technical Memorandum 100683, National Aeronautics and Space Administration, Goddard Space Flight Center, Greenbelt, Maryland, September 1987.
- Hollinger, J., R. Lo, G. Poe, R. Savage, and J. Pierce, *Special Sensor Microwave User's Guide*, Naval Research Laboratory, Washington, D.C., 1987.



## Chapter 2

### DMSP SSM/I SENSOR DESCRIPTION and CALIBRATION

Mark Goodberlet and Calvin T. Swift  
Department of Electrical and Computer Engineering  
University of Massachusetts  
Amherst, Massachusetts 01003

2.1 Sensor Description .....	5
2.2 Radiometer Precision and Absolute Accuracy .....	7
2.3 Antenna Pattern Correction .....	11
2.4 Antenna Beam Width and Side Lobe Level .....	12
2.5 Geolocation Problems .....	15
2.6 References .....	20

#### 2.1 Sensor Description

The Hughes Aircraft designed SSM/I (Hollinger, et al., 1987) was launched on June 19, 1987, and is the result of a joint Navy/Air Force operational program. Its purpose is to obtain synoptic maps of critical atmospheric, oceanographic, and selected land parameters on a global scale. The SSM/I is in a near polar earth orbit making 14.1 revolutions per day and sweeping out a 1400-km-wide swath every 1.9 seconds with its scanning antenna. Typical global coverage achieved in a single day is shown in Figure 2.1. The blackened diamond-shaped areas near the equator represent areas not "seen" by the sensor on this particular day but which will be seen in the next 2 or 3 days. Also,

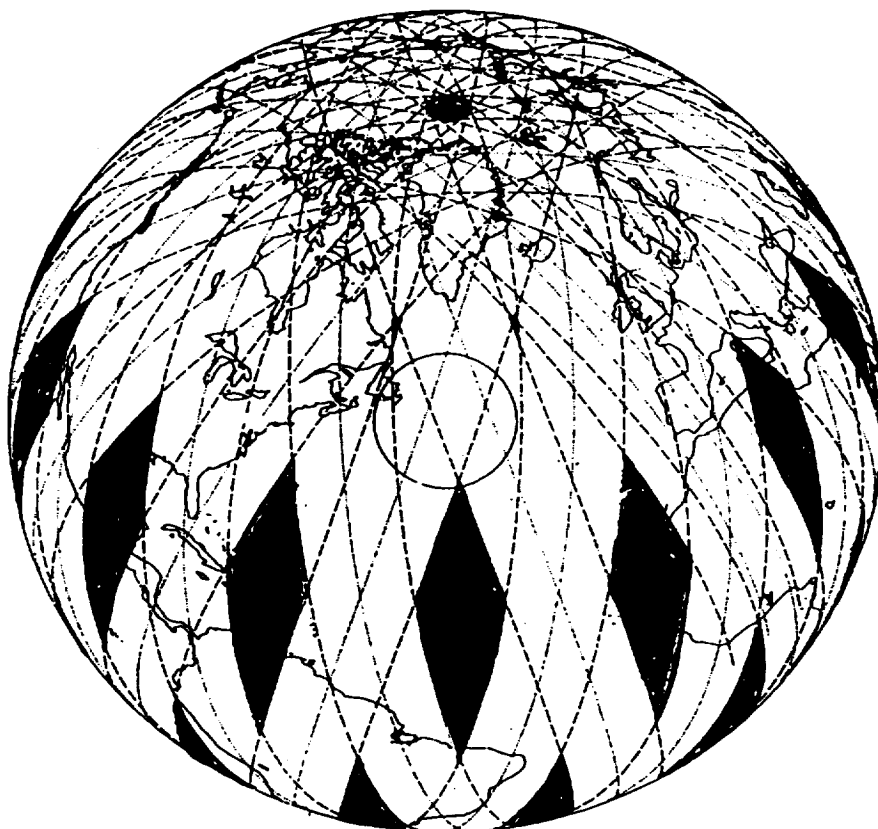


Figure 2.1. Global coverage of the SSM/I during a 24-hour period (from Hollinger et al., 1987).

surrounding both the north and south poles are small circular sectors of  $2.4^\circ$  latitude that are never seen, since the plane of the SSM/I orbit is tilted with respect to the Earth's axis of rotation.

The SSM/I employs a conical scan to achieve its 1400-km-wide swath. For this particular scanning geometry, the antenna is tilted so as to look out at a  $45^\circ$  angle from its spin axis. Satellite navigation instruments keep the antenna spin axis continually pointing at the Earth's center so that the antenna boresight traces out a circle on the Earth's surface. An additional advantage of the conical scan is that the boresight vector angle of incidence at the Earth's surface remains constant over the entire swath. Coordination of the antenna spin rate with the satellite forward motion and the fact that the sensor's receiver is allowed to view the earth during only  $102^\circ$  of the circular scan result in uninterrupted data collection over the 1400-km-wide swath.

The SSM/I directly measures microwave emission at 19.35, 37.0, and 85.5 GHz with both horizontal and vertical polarization and at 22.235 GHz with only vertical polarization. Henceforth, these seven channels will be referred to as 19H, 19V, 22V, 37V, 37H, 85V, and 85H. Collection of the data is accomplished using alternating "A" and "B" scanning modes (see Figure 2.2). During the B-scan, 128 radiometric measurements at 85.5 GHz are made, each separated along the scan by 12.5 km. The 128 measurements (pixels) of the B-scan are repeated in the A-scan, which is displaced 12.5

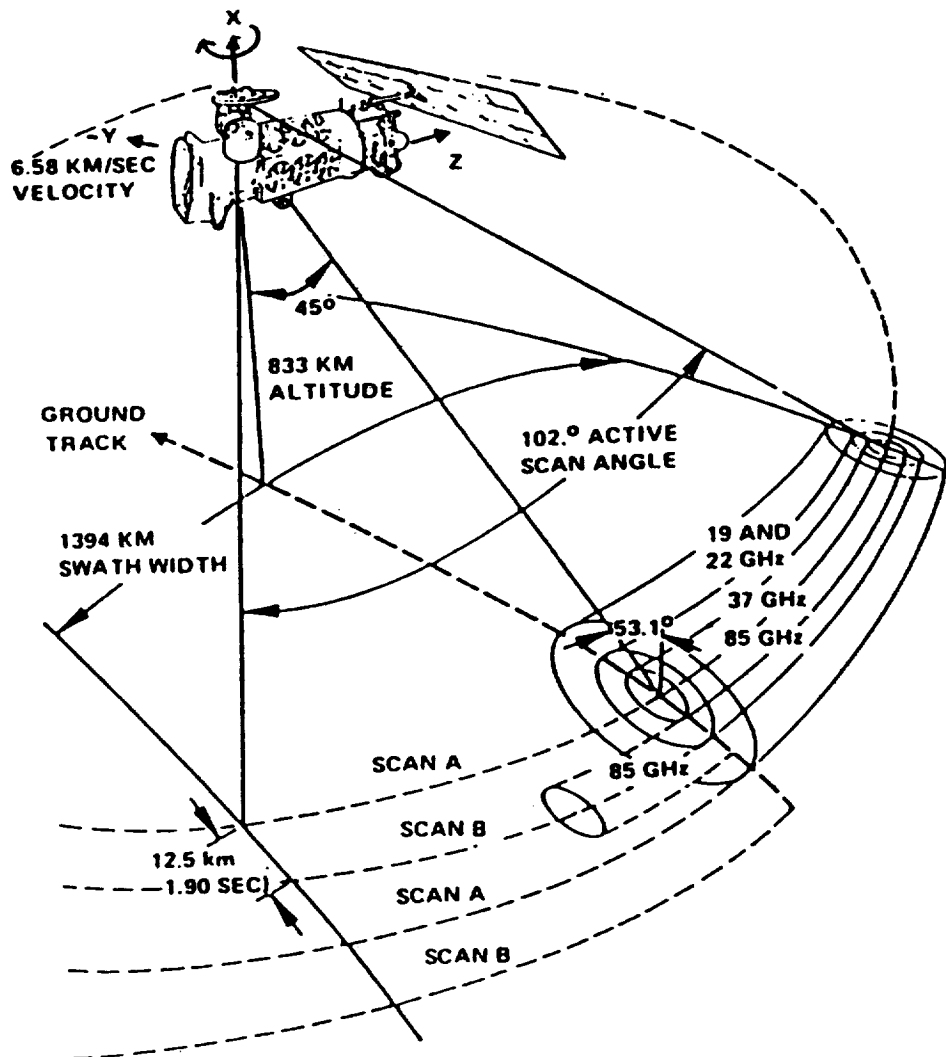


Figure 2.2. SSM/I scan geometry (from Hollinger et al., 1987).

km in the direction of satellite motion. In addition, 19-, 22-, and 37-GHz measurements are made at the odd-numbered pixel locations in the A-scan. Resolution, or what is also called footprint size, of the 19-, 22-, 37-, and 85-GHz channels are approximately 55, 49, 32, and 13 km, respectively.

The SSM/I is a total-power radiometer (Ulaby, et al., 1986) which calibrates once every scan (i.e., 1.9 seconds) by viewing both "hot" and "cold" internal calibration loads (see Figure 2.3). Recall, from the discussion above, that only during 102° of the circular scan is the receiver viewing the Earth. During part of the remaining 258° the receiver makes measurements of the hot load heated plate which is mounted on the sensor and has known radiometric emission. The cold load consists of a small reflector antenna which allows the receiver to look at the constant radiometric emission of cold space. These hot and cold load measurements enable the receiver to set up a linear calibration curve with which electrical measurements, made during the active part of the following scan, are converted into units of radiometric emission.

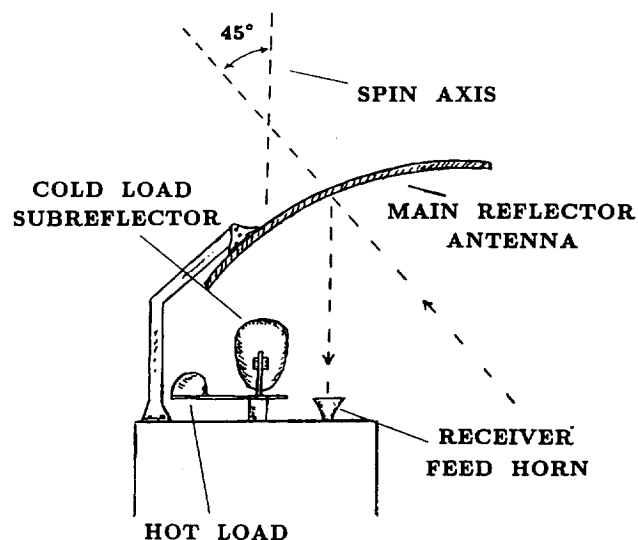


Figure 2.3. Sketch of the SSM/I. Note that the feed horn and main antenna rotate about the spin axis, while the assembly containing the hot and cold load is stationary.

## 2.2 Radiometer Precision and Absolute Accuracy

The SSM/I radiometer is designed to measure the power of microwave thermal emission received through its antenna and to convert the measurement, by means of calibration, into the radiometric antenna temperature  $T_A$  measured in Kelvins (K). If the characteristic antenna pattern for the SSM/I is given by  $G(\Theta, \Phi)$ , then  $T_A$  can be calculated using Equation 2.1.

$$T_A(\theta_o, \phi_o) = \int_0^\pi d\theta \int_0^{2\pi} \sin(\theta) d\phi TB(\theta, \phi) \cdot G(\theta_o - \theta, \phi_o - \phi) \quad (2.1)$$

Equation 2.1 indicates that the radiometric antenna temperature  $T_A$  is a weighted [by  $G(\Theta, \Phi)$ ] average of the emitting material's brightness temperature profile,  $TB(\Theta, \Phi)$ , over the radiometer antenna's field-of-view.

### 2.2.1 Brightness Temperature Precision

The SSM/I internal calibration is performed immediately preceding every scan (i.e., about once every 2 seconds), at which time the sensor makes five measurements of microwave emission from each calibration load. Associated with each of these five measurements is a voltage value that appears at the output of the SSM/I receiver. In turn, these voltage readings are quantized and stored by digital circuitry using a digital unit-of-measure called "counts." The quantization error or minimum separation between consecutive count values is approximately 0.1 K. The objective of the calibration is to associate the count values, CC and CH, corresponding to the SSM/I measurements of the cold and hot calibration loads with the known calibration load brightness temperatures, TC and TH, respectively. The points (CC,TC) and (CH,TH) define a calibration line with which any subsequent count, C, can be converted to a calibrated value, TA. Thus

$$TA = a \cdot C + b \quad (2.2)$$

where

$$a = (TH - TC) / (CH - CC)$$

$$b = TC - a \cdot CC$$

Both calibration loads emit a very constant amount of microwave energy during the time (approx 0.1 seconds) that the five calibration measurements are being made. The major reason for this stability is that the thermal inertia of each load precludes any large changes in emission over the time period of 0.1 second. Therefore, any difference between the five measurements of a particular load must be caused by contamination of the measurement by the SSM/I thermal noise. Thermal noise is characterized approximately by a zero-mean Gaussian distribution, and one can estimate the power of the noise by calculating the sample variance of the set of five calibration counts. Actually, such a measurement provides an estimate of the total count noise, which consists of both thermal noise and the count quantization noise. A more accurate measurement of the noise can be obtained by using measurements from many calibration cycles and plotting a histogram of the difference between each count measurement and the mean of the five-sample group containing the measurement. Examples of these histograms are shown in Figures 2.4 and 2.5 for both the hot and cold calibration load. Note that the shape of these histograms is approximately Gaussian. Also note the different widths of these histograms, which indicate that the variance,  $\text{var}(CH)$ , or noise-power associated with TA measurements made near the hot-load brightness temperature are different from the variance,  $\text{var}(CC)$ , associated with TA measurements made in the range of TC.

From Equation 2.2, one can calculate the TA variance,  $\text{var}(TA)$ , in terms of the count variance,  $\text{var}(C)$ , as follows:

$$\text{var}(TA) = a^2 \cdot \text{var}(C) \quad (2.3)$$

We now assume that the noise power on the count measurements varies linearly between the observed noise-power values associated with the hot and cold load count measurements. This assumption can be mathematically interpreted as follows:

$$\text{var}(C) = (1-d) \cdot \text{var}(CC) + d \cdot \text{var}(CH) \quad (2.4)$$

where

$$d = (C - CC) / (CH - CC)$$

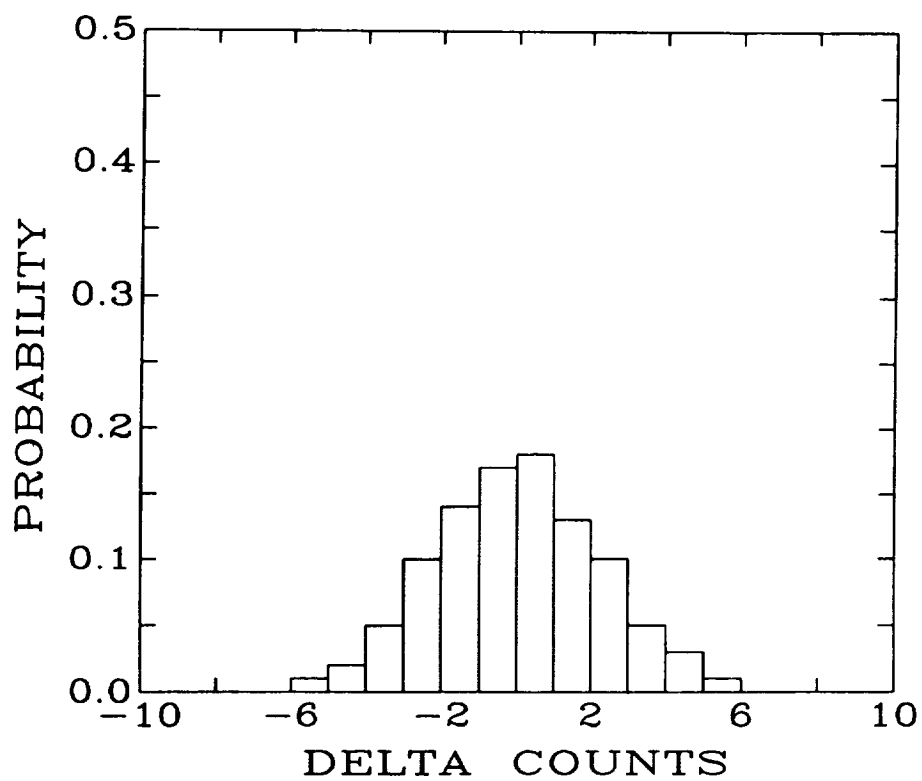


Figure 2.4. Histogram of SSM/I 19H hot-load calibration count deviations from the mean. Data from 24 April 1988.

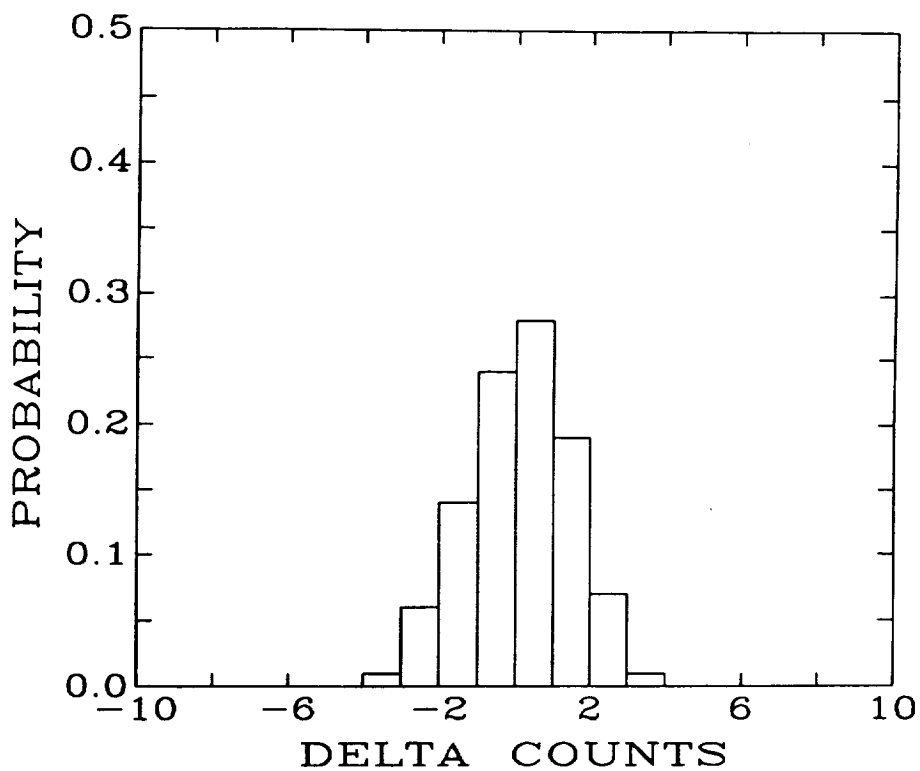


Figure 2.5. Histogram of SSM/I 19H cold-load calibration count deviations from the mean. Data from 24 April 1988.

Equation 2.4, together with Equation 2.3, can be used to calculate  $\text{var}(\text{TA})$  in terms of  $\text{var}(\text{CC})$  and  $\text{var}(\text{CH})$  as follows:

$$\text{var}(\text{TA}) = a^2 \cdot [(1-d) \cdot \text{var}(\text{CC}) + d \cdot \text{var}(\text{CH})] \quad (2.5)$$

The quantity,  $\text{var}(\text{TA})$ , is the SSM/I brightness temperature precision which was monitored at the University of Massachusetts (UMASS) during the months of July 1987 through May 1988. The results for all seven SSM/I channels along with the prelaunch specifications given by the Hughes Aircraft Company are shown in Table 2.1. Note that all measurements of brightness temperature precision, except that of the 85V channel, compare favorably with the specifications. The 85V channel failed in late 1988 because of what is believed to be a faulty mixer diode.

Table 2.1. Standard Deviation of the Instrument Noise for Each SSM/I Channel in Degrees Kelvin

Date	<u>CHANNEL</u>						
	19V	19H	22V	37V	37H	85V	85H
<u>Specifications at <math>T_B = 300K</math></u>							
	0.45	0.42	0.74	0.37	0.38	0.69	0.73
<u>Measured Values at <math>T_B = 300K</math></u>							
7/9/87	0.41	0.41	0.71	0.33	0.36	0.86	0.75
8/13/87	0.41	0.43	0.70	0.37	0.41	0.89	0.75
9/5/87	0.44	0.41	0.70	0.36	0.39	0.88	0.73
9/28/87	0.44	0.38	0.72	0.36	0.38	0.83	0.72
10/28/87	0.44	0.40	0.71	0.37	0.42	0.84	0.73
11/24/87	0.44	0.40	0.67	0.36	0.46	0.87	0.71
1/24/88	0.43	0.39	0.69	0.38	0.47	1.04	0.74
2/25/88	0.45	0.43	0.74	0.36	0.41	1.49	0.77
3/24/88	0.45	0.42	0.75	0.36	0.41	1.74	0.79
4/24/88	0.46	0.43	0.74	0.35	0.40	1.97	0.76
5/28/88	0.46	0.52	0.74	0.35	0.41	1.87	0.76

## 2.2.2 Brightness Temperature Accuracy

Two limitations of the internal calibration procedure make some additional calibration necessary. One limitation is that measurements of the hot and cold load emission do not make use of the main reflector antenna; therefore, spillover effects remain unaccounted for. Secondly, the hot and cold loads are unpolarized targets. That is, the amounts of horizontally and vertically polarized emission from the load are equal. Therefore, cross-polarization effects cannot be accounted for and will remain to contaminate operational antenna temperature measurements. Calibration tests done by the Hughes Aircraft Company prior to the SSM/I launch resulted in cross-polarization,  $C_p$ , and spillover,  $C_s$ , corrections, which are currently being applied to all the SSM/I measurements of TA. Calculation of the uncontaminated value of TA from the contaminated like-polarization value,  $TA_L''$ , and oppositely-polarized value,  $TA_O''$ , is given by

$$TA_L \equiv (1 + C_p)(1 - C_s)TA_L'' - (1 + C_s) \cdot C_p \cdot TA_O'' \quad (2.6)$$

The values for  $C_p$  and  $C_s$  supplied by Hughes Aircraft Company (Hollinger et al., 1987) are given in Table 2.2. There is reason to suspect that these correction coefficients may have been affected by the SSM/I launch or by its new operating environment.

Table 2.2. The Hughes Cross-Polarization,  $C_p$ , and Spillover,  $C_s$ , Coefficients for the SSM/I

Channel	$C_s$	$C_p$
19V	0.0320	0.00475
19H	0.0320	0.00417
22V	0.0267	0.01082
37V	0.0142	0.02218
37H	0.0142	0.02682
85V	0.0121	0.01402
85H	0.0121	0.01986

The procedure for verifying  $C_p$  and  $C_s$  is to select two Earthly scenes for which TA(V) and TA(H) are known. The SSM/I measurements of  $TA_V^i$  and  $TA_H^i$  over two different scenes at, for example, 19V and 19H, together with Equation 2.6, result in four equations, from which one can solve for the three unknowns,  $C_p(19V)$ ,  $C_p(19H)$  and  $C_s(19\text{ GHz})$ . In theory, this procedure is sufficient, however, in practice one has trouble obtaining accurate estimates of TA(V) and TA(H). The usual method is to calculate TA(V) and TA(H) using the equation of radiative transfer and independent measurements of key environmental parameters. The above procedure was used at the UMASS and in light of the inaccuracies in our radiative transfer model, it seems inappropriate to make any definite statements about the SSM/I absolute calibration. However, our comparisons indicate an absolute brightness temperature accuracy of about 2 K to 4 K. This is consistent with the work of the DMSP group (Hollinger, 1989), who concluded that the absolute calibration of the SSM/I is  $\pm 3$  K.

### 2.3 Antenna Pattern Correction

Antenna pattern correction (APC) (Stogryn, 1978) is a means by which antenna patterns can effectively be made more peaked near the center of the footprint (called beam sharpening). In addition APC can improve multi-peaked antenna patterns by reducing the level of the peaks which are not centered on the footprint (called side lobe reduction). In the discussions that follow, the angular variables,  $\Theta$  and  $\Phi$  will be replaced by the spatial variables,  $x$  and  $y$ , which locate a point on the "flat-Earth" surface. Furthermore, for clarity in our APC discussion, the three-dimensional problem of measuring  $TA(x_0, y_0)$  has been reduced to a one-dimensional problem where the relevant quantities are  $TA(x)$ ,  $G(x)$  and  $TB(x)$ .

A precondition for using APC is that the radiometer must make near simultaneous measurements over an area much larger than a footprint and that the footprints associated with these measurements have some spatial overlap with each other. Consider three overlapping footprints whose centers are separated by the distance,  $L$ . Performing a weighted [by  $c(i)$ ] sum of the three measurements associated with these three footprints allows us to write an expression for an "effective" value of TA called  $TA_e$ .

$$\begin{aligned}
 TA_e(x_0) &= \sum_i c(i) \cdot TA(x_0 - iL) \\
 &= \sum_i c(i) \int_{AF} dx G(x_0 - iL - x) \cdot TB(x) \\
 &= \int_{AF} dx \left[ \sum_i c(i) \cdot G(x_0 - iL - x) \right] \cdot TB(x)
 \end{aligned} \tag{2.7}$$

In Equation 2.7, the integration is over the footprint area, AF, and the term in square braces will be called the effective antenna pattern,  $G_e(x)$ , for reasons to be explained below. Therefore, by performing a weighted sum of a group of radiometric measurements centered on the point,  $x_0$ , one has effectively created a new measurement of the microwave radiation being emitted by bodies near  $x_0$ , made by a hypothetical radiometer with effective antenna pattern  $G_e(x)$ . Proper selection of the weights,  $c(i)$ , can produce an effective antenna pattern which is either more peaked (beam sharpened) or has lower side lobe levels than the radiometer's actual antenna pattern function. A fundamental limitation of any APC is that beam sharpening correction results in higher side lobe levels and conversely that reducing side lobe levels will simultaneously widen the beam; i.e., one problem is solved at the expense of aggravating the other.

A restriction on the selection of the  $c(i)$  in Equation 2.7 is that they must sum to 1. This restriction is apparent when considering a scene where  $TB(x)$  is constant. Under this condition one knows that  $TA_e(x_0) = TA(x_0) = TB(x_0)$ , and from Equation 2.7, this can only be true if the  $c(i)$  sum to unity. Finally, one should note a potential disadvantage of APC called noise amplification. Suppose, for example, that the variance of the noise associated with all measurements of  $TA(x)$  is  $\text{var}(TA)$  and all such measurements are uncorrelated. From Equation 2.7, one can calculate the variance,  $\text{var}(TA_e)$ , of the noise on  $TA_e(x)$  as follows:

$$\text{var}(TA_e) = \text{var}(TA) \cdot \sum_i c^2(i) \quad (2.8)$$

Therefore, if the sum of the squares of the weighting coefficients is larger than unity, which it almost always is for useful APC, then the noise of the measurement used to approximate  $TB(x_0)$  has increased.

The APC for the SSM/I is exactly given by Equation 2.7, and the three values of  $TA(x)$  are obtained from three consecutive footprints of the SSM/I scan. The values of  $c(i)$ , determined by Hughes were found to give an almost insignificant amount of beam sharpening as well as a slight amount of noise amplification. As will be shown in the next section, we found that the side lobe level and the resolution of the SSM/I need no adjustment, and recommended that the Hughes APC not be used.

## 2.4 Antenna Beam Width and Side Lobe Level

Although the antenna pattern functions for each of the seven SSM/I channels were measured before its launch (Hollinger et al., 1987), there is reasonable concern that such things may be affected by the stress of the launch and the severe operating environment of outer space. For this reason UMASS devised a method for determining antenna beam width and side lobe levels using "in-orbit" measurements of  $TA(x,y)$  made by the SSM/I near land/ocean boundaries. Since the brightness temperature of land differs considerably from that of ocean, the  $TB(x,y)$  profile along a land/ocean boundary can be accurately approximated as a step function. As the SSM/I passes over these coastal regions, one can predict the behavior of the measured values of  $TA(x,y)$  using Equation 2.1. If, for example, one can approximate  $G(x,y)$  as a two-dimensional Gaussian function with characteristic standard deviations,  $(\sigma_x, \sigma_y)$ , then  $TA(x,y)$  is calculated from Equation 2.1 to be dependent on  $x$  and  $y$  through the Gaussian error function.

More specifically, the procedure used to measure  $G(x,y)$  was first to make some assumption about the shape of the pattern (e.g., it is Gaussian). Unless the antenna pattern is perfectly symmetric (i.e., in the case of Gaussian,  $\sigma_x = \sigma_y$ ), then the rise time of  $TA(x,y)$  during the SSM/I coastal overpass will depend on the orientation of  $G(x,y)$  with respect to the boundary edge. Therefore, the second part of the procedure is to select two coastal overpasses for which the orientation of  $G(x,y)$  with respect to the coastal boundary is different. The two sets of  $TA(x,y)$  measurements made during the two coastal overpasses, together with their descriptive Equation 2.1 and the step function assumption for  $TB(x,y)$ , can be used to solve for the two unknown beam width parameters  $(\sigma_x, \sigma_y)$  in the case of Gaussian).

In practice, the procedure for measuring  $G(x,y)$  becomes quite complicated since the orientation of  $G(x,y)$  depends upon its position in the SSM/I scan and upon the direction at which the SSM/I is approaching the coastal boundary. Furthermore, linear coastal boundaries without offshore islands are needed to insure that the step-function

assumption for  $TB(x,y)$  is reasonably accurate, and such boundaries are somewhat difficult to find. Finally, the Gaussian beam assumption used in our description above works reasonably well for measuring antenna beam width, but this pattern function is not double peaked and, by our definition, has no side lobes. Therefore, to investigate the SSM/I side lobe levels, we used antenna pattern functions of the form,  $(\sin(a \cdot x) \cdot (\sin(b \cdot y)/(a \cdot b \cdot x \cdot y)))^N$ , which will be referred to as  $\text{sinc}^N$  patterns. In Figure 2.6, we compare the coastal overpass variation of  $TA(x,y)$  for the Gaussian and  $\text{sinc}^2$  antenna pattern functions. In order to make a fair comparison, these hypothetical pattern functions were designed to have the same half-power beam width and therefore differ only in shape and side lobe level. The  $\text{sinc}^2$  side lobe effects are most noticeable in the reduced slope of the leading and trailing edges on the rise curve of  $TA(x,y)$ .

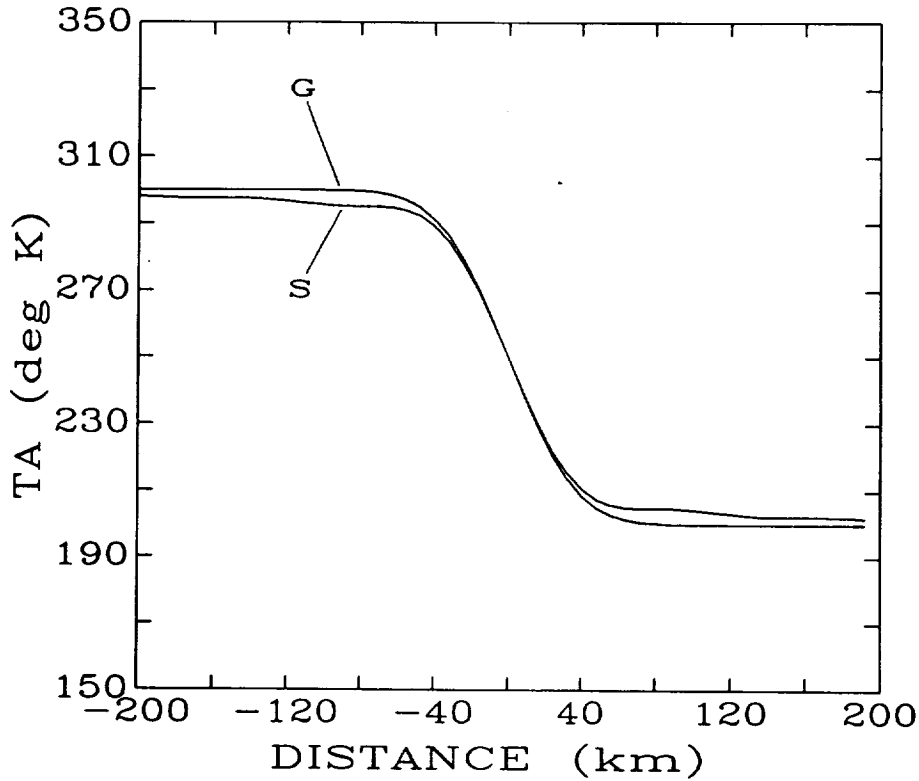


Figure 2.6. Variation in  $TA$  as a function of footprint distance from a land/ocean boundary for gaussian,  $G$ ,  $\text{sinc}^2$ ,  $S$ , antenna beams.

Detailed geometry of the problem is given in Figure 2.7, where  $TB_w$  is the brightness temperature of water,  $TB_L$  is the brightness temperature of land,  $\alpha$  is the angle at which  $G(x,y)$  is oriented with respect to the linear boundary, and  $d_0$  is the distance from the boundary to the center of the SSM/I footprint along a line that is perpendicular to the boundary and intersects the center of the footprint. Using Equation 2.1, one can write the expression of  $TA(x,y)$  during the coastal overpass as follows:

$$TA(d_0(x,y)) = (TB_L - TB_w) \cdot I + (TB_L + TB_w)/2 \quad (2.9)$$

where

$$I = \int_0^{d_0/\sigma_e} dz f(z)$$

Gaussian:

$$f(z) = e^{-z^2/2} / \int_{-\infty}^{\infty} dz e^{-z^2/2}$$

$$\sigma_e^2 = \sigma_x^2 \cdot \cos^2(\alpha) + \sigma_y^2 \cdot \sin^2(\alpha)$$

sinc<sup>4</sup>:

$$f(z) = \left( \frac{\sin^4(z)}{z^4} \right) / \int_{-\infty}^{\infty} dz \left( \frac{\sin^4(z)}{z^4} \right)$$

$$\sigma_e^2 = a^{-2} \cdot \cos^2(\alpha) + b^{-2} \cdot \sin^2(\alpha)$$

The TA(x,y) measurements from each coastal overpass, together with Equation 2.9, comprise a set of equations which can be solved using a Newton-Raphson minimum squared error (NRMSE) (Carnahan, 1964) procedure to obtain values for the unknowns, TB<sub>L</sub>, TB<sub>w</sub>, and  $\sigma_e$ . Several other sets of overpass data taken at different orientation angles result in several other values for  $\sigma_e$ , each of which represents an equation in the two unknowns, ( $\sigma_x$ ,  $\sigma_y$ ) or (a,b). The NRMSE technique was again used to solve this second system of equations and obtain values for the beam pattern function parameters, ( $\sigma_x$ ,  $\sigma_y$ ) or (a,b). Finally these parameters, together with the corresponding mathematical expressions for G(x,y), were used to calculate the footprint size (i.e., half-power beam width).

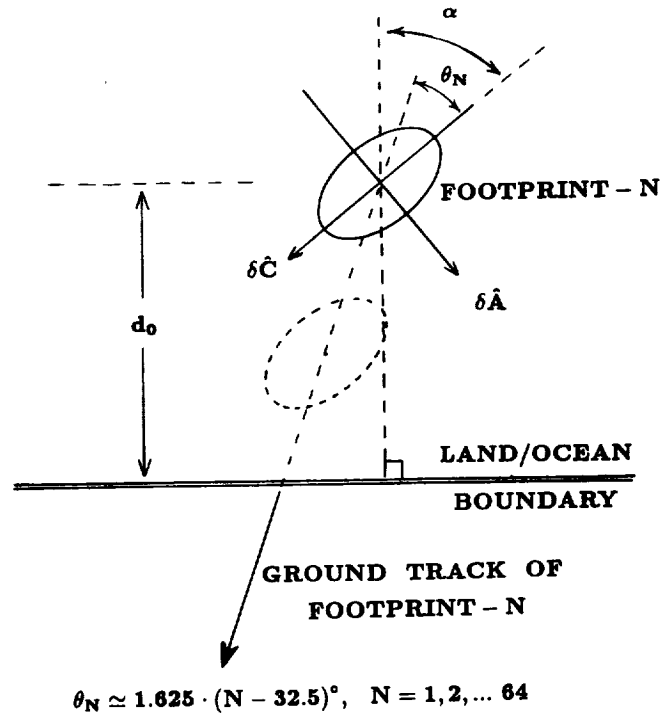


Figure 2.7. Geometry of SSM/I footprint approaching a land/ocean boundary showing the cross-scan axis,  $\delta\hat{C}$ , along-scan axis,  $\delta\hat{A}$ , and the Nth footprint of the 64-footprint area.

Results of this work are listed in Table 2.3, and one should note that all beam widths were measured to be no farther than one standard deviation of the measurement error from the prelaunch specifications except for the 19H and 22V channels. From the shapes of the leading and trailing edges of the TA(x,y) rise curve, we also concluded that side lobe levels were about 24 decibels below the main lobe of the antenna beam for all channels. These side lobe levels are within the Hughes specifications, and we therefore conclude that a side lobe reducing APC is unnecessary. Furthermore, we recommend against using a beam sharpening APC, since we consider the resulting noise amplification to be an unacceptable tradeoff for increased resolution.

Table 2.3. Measurements of SSM/I Antenna Half-Power Beam Widths in Kilometers

Error indicated is the measurement error.

Channel	Cross-Scan		Along-Scan		Error
	Specs*	Measured	Specs*	Measured	
19V	69	68.5	43	42.8	2.7
19H	69	65.0**	43	41.3	2.3
22V	50	57.6**	40	39.1	4.3
37V	37	39.5	28	27.9	3.7
37H	37	38.6	29	26.2	4.1
85V	15	17.1	13	12.0	3.0
85H	15	18.6	13	11.0	5.0

\*Hughes aircraft specifications

\*\*Measured values which differ from specified values by more than the measurement error

## 2.5 Geolocation Problems

Mislocation of the SSM/I footprints by as much as 30 km has been observed. This geolocation error appears to consist of a predictable (hence removable) component and a random (i.e., not currently predictable) component with an rms magnitude of about 8 km. Measurement and removal of the predictable component of the geolocation error is discussed below. Despite the good results, users of the SSM/I data should bear in mind that occasionally the random geolocation error can become quite large, as shown by Wentz (1989).

The discussion to follow will focus on the UMASS methods used to measure and correct the geolocation error. Geolocation correction software developed by UMASS is currently being used by a number of agencies to relocate the SSM/I data. Its popularity seems to be a result of the algorithm's simplicity, computational efficiency, and ability to reduce the geolocation error to a more acceptable  $\pm 8$  km. The problem has more recently been studied by researchers at Remote Sensing Systems (RSS) (Wentz, 1989) and the Naval Research Laboratory (NRL) (Hollinger, 1989). The NRL results will be discussed first, followed by those of UMASS and RSS.

The SSM/I brightness temperature measurements are tagged with latitude and longitude by an orbit prediction program being run at the Fleet Numerical Oceanography Center (FNOC) in Monterey, California (Hollinger, 1989). This software, called TRACE66, can accurately calculate SSM/I footprint locations for about 7 days, after which the program must be reinitialized with a new location and time fix for the SSM/I. This reinitialization is necessary because of the limitations of the orbit model used in creating TRACE66, which can only approximate the forces acting upon an Earth-orbiting satellite. The NRL investigation suggested the following causes of the geolocation problem. First, the

TRACE66 program failed to account sufficiently for the gravitational variations with Earth latitude; hence, the geolocation error exhibited a latitude dependence. Second, the 7th-day location and time fix were often inaccurate, resulting in a fixed geolocation error that would persist for the next 7 days. Third, NRL found that the above two errors could not account for the total geolocation error. The remaining error was attributed to a pitch, yaw, and roll of the satellite attitude or of the SSM/I mount to the satellite. As a result of the NRL study, the 7-day location/time updates are now more accurate and more frequent. Also, the 1966 TRACE66 program has been updated, but the pitch, yaw, and roll problem continues to cause mislocation of the SSM/I data.

The UMASS effort began with the assumption that the geolocation errors were attributable only to a pitch, yaw, and roll of the SSM/I, and that these three attitude angles may be functions of both latitude and time. This basic assumption was not very restrictive since, in the small angle limit, spacecraft translational errors caused by inaccurate location/time fixes could approximately be accounted for by pitch and roll adjustments. Also, the latitude variations caused by inaccuracies in the TRACE66 software could be accounted for by making the pitch, yaw, and roll adjustments latitude-dependent.

The first objective of the UMASS investigation was to measure the geolocation error as a function of latitude, time, and scan position. This was done by using a correlation scheme wherein gridded SSM/I brightness temperature measurements were correlated with accurate maps of small ocean islands. Ocean islands about 50 km in diameter were used instead of coastal boundaries, so that the mislocation of individual footprints in the SSM/I scan could be studied. The 15 islands used for the study are listed in Table 2.4.

Table 2.4. Islands Used to Geolocate the SSM/I Data

Name	Latitude	Longitude(E)	Size(km)
Malta & Gozo	35.9	14.4	20 x 50
Oahu	21.5	202.0	50 x 50
Kauai	22.1	200.4	50 x 50
Seguam	52.3	187.5	15 x 20
Mauritius	-20.3	57.5	50 x 75
Le Reunion	-21.2	55.5	50 x 75
Palma	28.7	342.2	25 x 50
Gran Canaria	27.9	344.4	50 x 50
Madeira	32.7	343.0	25 x 50
Fogo	14.9	335.5	25 x 25
Boavista	16.1	337.2	35 x 35
Tome	0.2	6.6	35 x 50
Attu	52.9	173.0	20 x 40
S. Georgia	-54.4	323.0	30 x 60
Bornholm	55.1	15.0	20 x 30

The shift needed for maximum correlation of the island maps and gridded SSM/I brightness temperatures was expressed in terms of a coordinate system referenced to the SSM/I scan whose orthogonal axes are labelled cross-scan and along-scan (see Figure 2.8). Plots of the measured cross-scan and along-scan shifts for each island as a function of scan position were made as shown in Figures 2.9 and 2.10. Since the islands are at different latitudes, each set of plots for a particular island gives a measure of the geolocation error at that particular island's latitude. The plots were also made using only a single months data so that the time variation (from month to month) of the geolocation error could be studied.

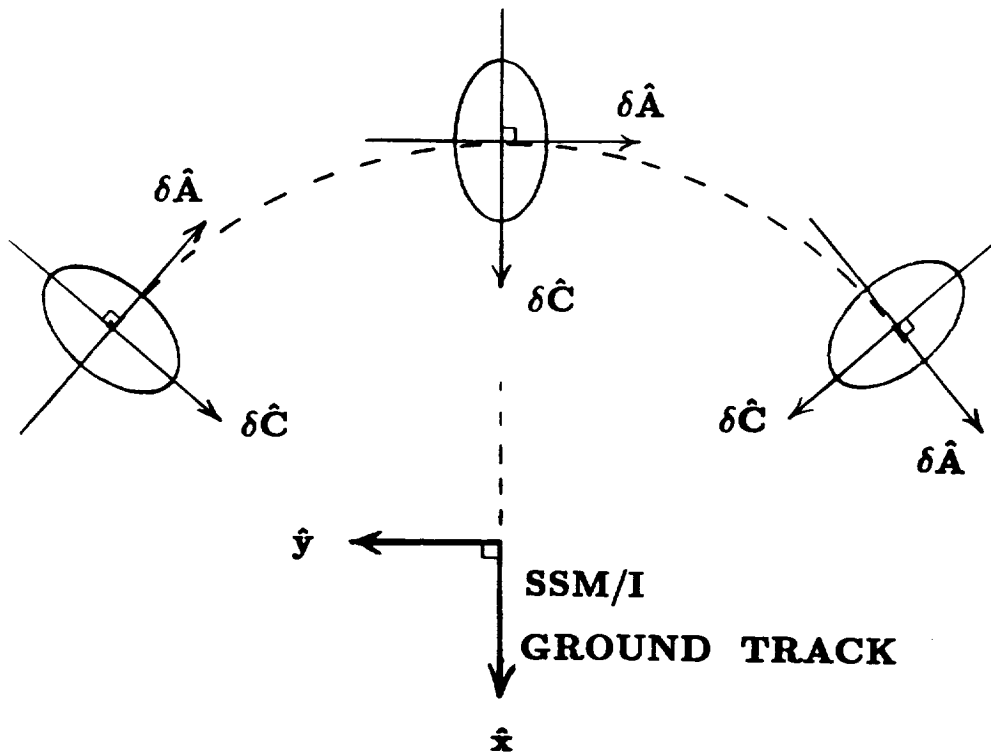


Figure 2.8. Cross-scan,  $\sigma \hat{C}$ , and along-scan,  $\sigma \hat{A}$ , axes for three footprints in the SSM/I scan.

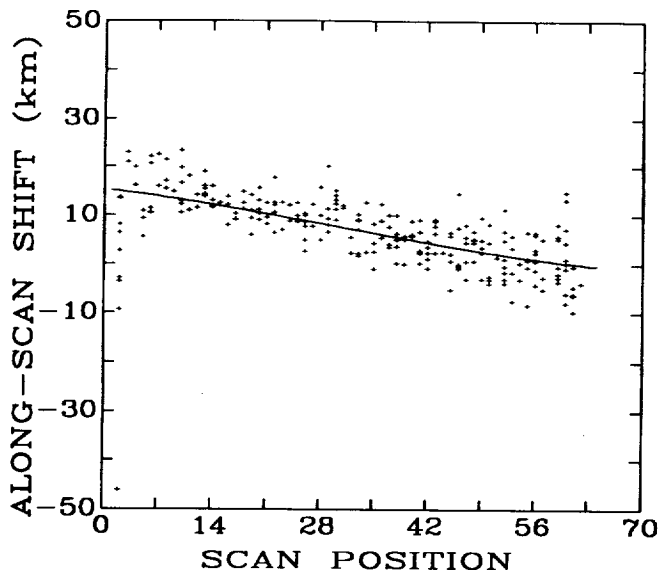


Figure 2.9. Dependence of the SSM/I along-scan geolocation shift upon position within the scan. Data from July 1987.

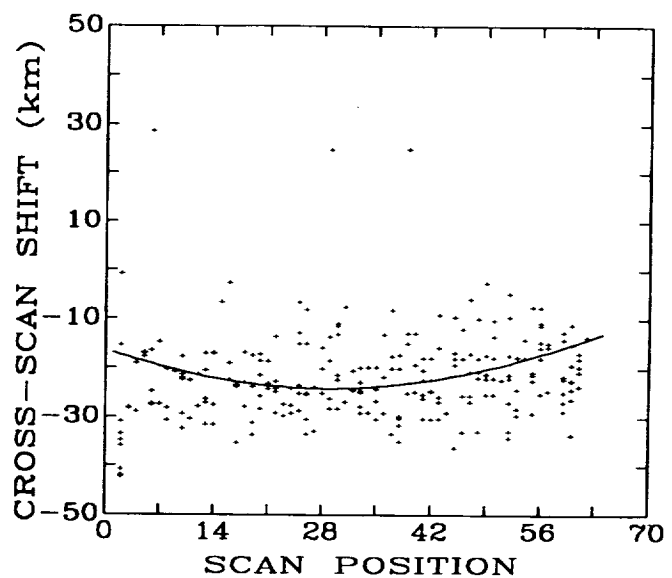


Figure 2.10. Dependence of the SSM/I cross-scan geolocation shift upon position within the scan. Data from July 1987.

The measurements described previously indicated that the geolocation error was largest near the Earth's equator and became smaller as one moved toward either the North or South polar regions. Also, the error seemed to be largest during the months of December and January and became smaller as one moved toward the month of July, thereafter, increasing as one moved toward January again. This time dependence may have resulted from thermal expansion of SSM/I mounting parts caused by an unexpected solar heating problem which has resulted in brief SSM/I shut-downs during the months of December and January.

The second objective of the UMASS investigation was to identify pitch, yaw, and roll angles which could account for the geolocation errors that were revealed in the plots of cross-scan and along-scan shift versus scan position. Using the geometry shown in Figure 2.11 and small angle approximations, UMASS found that the cross-scan shift,  $\delta C$ , and the along-scan shift,  $\delta A$ , could be expressed as follows:

$$\delta C \equiv -R \left\{ \frac{\alpha - \beta}{\beta} \right\} \delta \theta \quad (\text{kilometers}) \quad (2.10)$$

$$\delta A \equiv R \{ \alpha - \beta \} \sin(\theta_c) \delta \phi \quad (\text{kilometers}) \quad (2.11)$$

where

$$\alpha = \left( 1 + \frac{H}{R} \right) \cos \theta_c, \quad \beta = \sqrt{1 + \left( 1 + \frac{H}{R} \right)^2 \sin^2 \theta_c}$$

$$\delta \theta \equiv \theta_p \cos \phi - \theta_r \sin \phi$$

$$\delta \phi \equiv \theta_y - \{ \theta_r \cos \phi + \theta_p \sin \phi \} \cot \theta_c$$

$$R = \text{Earth radius} \equiv 6371 \text{ km}$$

$$H = \text{SSM/I Altitude} \equiv 833 \text{ km}$$

$$\theta_c = \text{Half-angle of SSM/I scan cone} = 45^\circ$$

$$\phi = \text{Scan angle from } 128.8^\circ \text{ to } 231.2^\circ$$

$$\theta_p = \text{Satellite pitch angle}$$

$$\theta_r = \text{Satellite roll angle}$$

$$\theta_y = \text{Satellite yaw angle}$$

Positive pitch, yaw, and roll are defined by the "right-hand rule" with thumb along the Y, Z, and X axes, respectively. See Figure 2.11 for orientation of the SSM/I XYZ coordinate system.

Using the above equations and plots like those shown in Figures 2.9 and 2.10, a Newton-Raphson minimum squared error (NRMSE) solution for corrections to the SSM/I pitch, yaw, and roll angles was obtained. One set of attitude correction angles for each island (i.e., latitude) was obtained for each month during the period July 1987 thru July 1988. Using this large data set, a NRMSE solution for the latitude and time dependence of each attitude correction angle was obtained and is summarized in Equation 2.12.

$$\theta_j = C_{j1} + C_{j2} \cdot \text{JDAY} + C_{j3} \cdot |\text{LAT}| + C_{j4} \cdot (\text{JDAY})^2 \quad (2.12)$$

where the coefficients  $C_{ji}$  are given in Table 2.5.

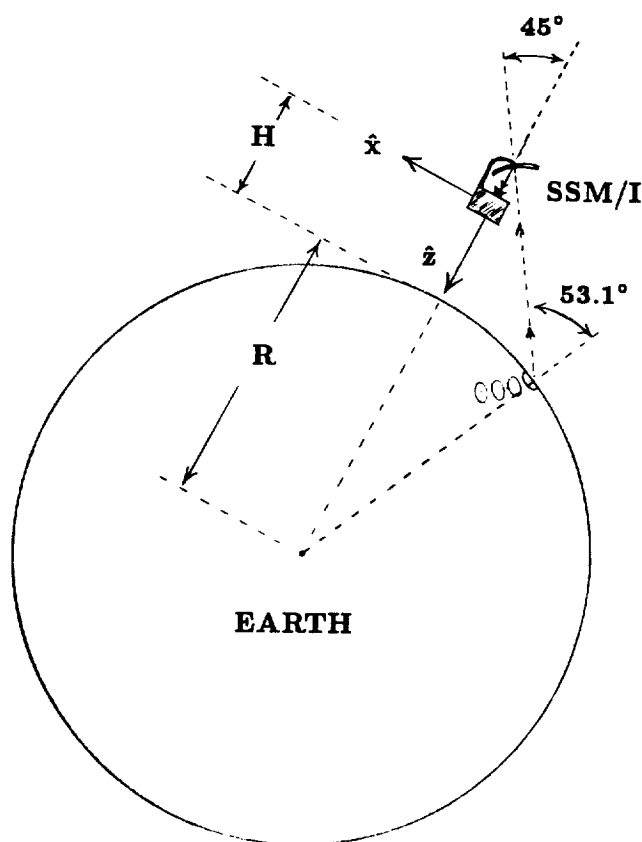


Figure 2.11. Sketch of the SSM/I orbiting the earth.

Table 2.5. Regression Coefficients for Satellite Pitch, Roll, and Yaw

j	$C_{j1}$	$C_{j2}$	$C_{j3}$	$C_{j4}$
1 (PITCH)	-1.108	0.0025	0.0036	-0.0299
2 (YAW)	0.653	-0.0007	-0.0026	0.0111
3 (ROLL)	-0.240	0.0004	0.0026	-0.0043

In Equation 2.12, the term JDAY is the number of days after December 31, 1986. For example, JDAY=1 corresponds to January 1, 1987, and JDAY=366 corresponds to January 1, 1988. Scatterplots like those shown in Figures 2.9 and 2.10 indicate that these attitude correction angles can account for all but an RMS geolocation error of 8 km both along and across the SSM/I scan. A short FORTRAN program for implementing this correction is given in an appendix to this report and is called PIXFIX. PIXFIX was independently tested by Konrad Steffen of the University of Colorado at Boulder and tested to a lesser degree by several other researchers since.

Frank Wentz (1989) of RSS has also studied the SSM/I geolocation problem using a different method. Both he and UMASS have found variations along-scan in the SSM/I measured brightness temperatures over scenes where the brightness temperatures should be constant. This particular problem has been seen in the data of other satellites (Njoku, et al., 1980) and is called a "cross-track" bias, since it is a bias that varies along a direction perpendicular to the satellite ground track. The angle between the SSM/I antenna boresight and a normal to the Earth's surface at the footprint location is called the "local incidence angle." Changes in the local incidence angle will cause predictable changes in the measured

brightness temperature. Since changes in the local incidence angle can be caused by both pitch and roll (not yaw) of the SSM/I, Wentz was able to verify independently the pitch and roll problem by studying the cross-track brightness temperature bias. His results are in agreement with the work done at UMASS.

A number of users are obtaining SSM/I data in the compact-TA format produced by Frank Wentz at RSS. Beginning with the January 1989 SSM/I data, RSS is supplying corrected latitude and longitude data on all the compact-TA tapes. These corrections reduce the geolocation error to less than 10 km (Wentz, 1989). The geolocation software described previously should not be applied to SSM/I data from the 1989 compact-TA tapes, since this would result in a double correction and erroneous results.

## 2.6 References

- Carnahan, J. B., H. A. Luther, and J. O. Wilkes, *Applied Numerical Methods*, p. 421, John Wiley and Sons, Inc., New York, 1964.
- Hollinger, J., R. Lo, G. Poe, R. Savage, and J. Peirce, *Special Sensor Microwave/Imager User's Guide*, Naval Research Labs, Washington D.C., 1987.
- Hollinger J. P., *DMSP Special Sensor Microwave/Imager Calibration/Validation*, Naval Research Labs, Washington D.C., 1989.
- Njoku, E. G., J. M. Stacey, and F. T. Barath, The SEASAT Scanning Multichannel Microwave Radiometer (SMMR): Instrument Description and Performance, *IEEE Jour. Oceanic Engr.*, OE-5, 2, pp. 100-115, 1980.
- Ulaby, F. T., R. K. Moore, and A. K. Fung, *Microwave Remote Sensing Active and Passive*, vol. 1, Artech House, Norwood, Massachusetts, 1986.
- Wentz, F. J., Mislocated Orbits and Out-of-Bounds Data, Remote Sensing Systems SSM/I Memo 061589, Santa Rosa, California, 1989.

## Chapter 3

### DMSP SSM/I DATA PROCESSING and ARCHIVE

Charles S. Morris  
Jet Propulsion Laboratory  
California Institute of Technology  
Pasadena, California 91109

and

Ronald L. S. Weaver  
National Snow and Ice Data Center  
University of Colorado  
Boulder, Colorado 80302

3.1 Overview .....	21
3.2 SSM/I Data Flow .....	22
3.3 Data Problems .....	22
3.4 Data Archiving Activities .....	23
3.5 References .....	24

#### 3.1. Overview

The Jet Propulsion Laboratory (JPL) node of the NASA Ocean Data System (NODS) and the National Snow and Ice Data Center (NSIDC) were tasked by NASA to develop and implement a computer system to process and archive sea ice products derived from SSM/I data. This cooperative effort began in 1983 and culminated in October 1989 with the successful transfer of all processing, archiving, and data distribution responsibilities to NSIDC, which will remain the long-term archive for the NASA sea ice products.

The original concept of the NASA SSM/I sea ice archive was to have a centralized computer-based system which users could access to extract different archive products interactively. The products that were recommended by the NASA Science Working Group for the SSM/I (NASA-SWG, 1984) included global swath brightness temperatures (TB), 1-day average temperatures on 12.5-km (85-GHz channels only) and 25-km (other five channels) polar grids, 3-day average ice concentration (FY, MY, and total) on a 50-km polar grid, ice extent based on the 85-GHz channels, and selected "monitor areas" to track the health of the sensor. Several changes have been made to this list. The ice concentrations are now computed as 1-day averages on a 25-km grid, and the last two products, the ice extent and monitor areas, have been eliminated.

Rapidly improving technology has made it cost effective to provide data to users in ways that were not originally envisioned when the computer-based NSIDC Cryospheric Data Management System (CDMS) was originally designed (see Weaver et al., 1987). The emphasis has shifted from an on-line data archive and delivery system to mass distribution of data provided to researchers at their home institutions. For NASA polar SSM/I data distribution, the gridded polar 1-day average TB and 1-day average ice-concentration grids are available on CD-ROM. The CD-ROMs contain about 3 months of data and are issued four times a year.

The software developed by JPL/NODS has been transferred to NSIDC where it is called the Cryospheric Data Management System (CDMS) (see Weaver et al., 1987).

### 3.2. SSM/I Data Flow

The DMSP F-8 satellite was launched on June 19, 1987, into a polar orbit. After the initial instrument checkout, the first sensor data from SSM/I were taken on July 9, 1987. The first several months of data were impounded by the Navy so that their Calibration/Validation (CAL/VAL) Team could review the performance of the SSM/I instrument. On November 17, 1987, the Navy officially released the SSM/I swath antenna and TBs. JPL/NODS began receiving SSM/I swath antenna temperatures via the Satellite Data Services Division (SDSD) of NOAA-National Environmental Satellite, Data and Information Service (NESDIS) in mid-March, 1988, 9 months after launch. The data used by JPL/NODS and NSIDC are produced by the Fleet Numerical Oceanography Center (FNOC). Direct data receipt from FNOC was not possible because of prior arrangements between NOAA-NESDIS-SDSD, the Navy, and the Air Force. NASA has negotiated an agreement with RSS for delivery of data in a more compact format. The RSS-formatted data is being delivered to NSIDC under the auspices of the WETNET program at Marshall Space Flight Center. The SSM/I data flow from acquisition at FNOC to the distribution of the gridded sea ice products by CDMS is illustrated in Figure 3.1.

### 3.3. Data Problems

It was anticipated that the initial 2 months of data processing at JPL/NODS would be spent testing out the software system. However, even before JPL/NODS had received any data, problems in the data, which would require modifications to the software system, began to become apparent to various researchers. These included an error in the

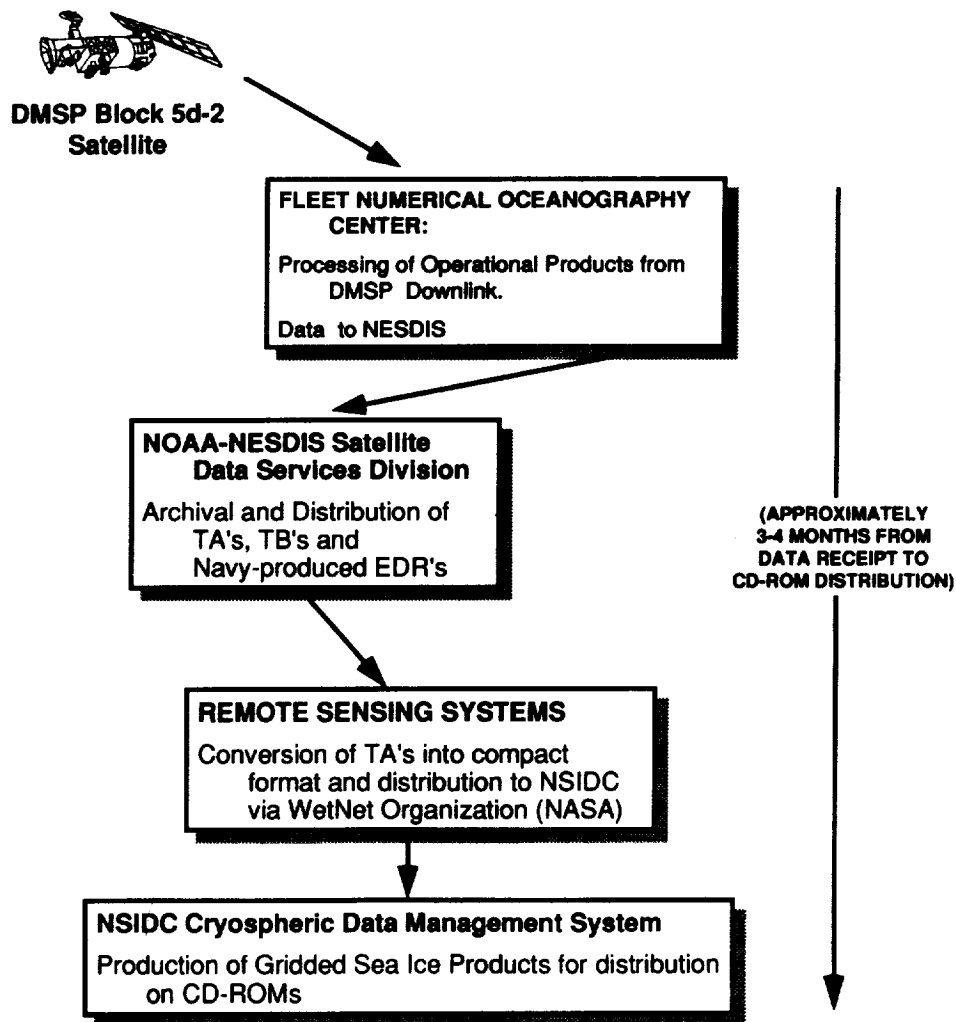


Figure 3.1. Cryospheric data management system data flow.

geolocation of the data, a satellite recorder anomaly, and apparent data transmission glitches. The latter two introduced spurious data into the data files.

The first system modification involved correcting the latitude and longitude values that are included with each observation. These values pinpoint the location on the Earth of the center of the observation footprint. By comparing the location of the coastline in the SSM/I data, which is denoted by a steep gradient in the brightness temperatures, it was discovered by several investigators that the latitude/longitude values given in the data were in error by approximately 25 km. Considering that the spatial resolution of the brightness temperature observation is of the same order or greater, depending on the channel, as the location error, this posed a significant obstacle to producing high-resolution products. The problem for gridded products is compounded in that the error will result in a 50-km smear, because the spacecraft passes over the grid cell from different directions.

At the recommendation of the NASA SSM/I Validation Team, JPL/NODS and NSIDC adopted a technique proposed by Mark Goodberlet and Calvin Swift, at the University of Massachusetts, and Konrad Steffen, at CIRES, University of Colorado, to correct the retrospective data. This technique, discussed in Section 2.5, assumes that the shift in the location values is caused by a pointing error, which can be compensated for after the fact by adjusting the roll, pitch, and yaw angles of the spacecraft. Islands are used as targets, and a regression analysis is used to determine the yaw, pitch, and roll values that provide the best agreement between the islands and their antenna temperature images. These yaw, pitch, and roll values are then used to correct the latitude and longitude of each swath scene station. This correction is expected to improve the geolocation accuracy to better than 10 km.

Because of the empirical nature of the geolocation correction, it was decided that the swath data archive would not include the corrected locations. The routine to perform the correction is available to researchers who wish to use the swath data. The corrections will be applied to the swath data prior to producing the gridded products so that the 50-km smear will be minimized.

It should be noted that the Navy also investigated the geolocation problem. Corrections were implemented in early 1990 in the processing performed at FNOC. Thus, the need to apply a geolocation correction to the SSM/I data may eventually be eliminated. The second system change was required to detect and manage data anomalies created as a result of a problem with the spacecraft recorder. On an average, more than one swath data file per day (each file is about one orbit) would have spurious data appended to the beginning of the file. This would often show up as a few scans of bad data followed by a time gap or regression, after which the "good" data would be given. The situation was further complicated by the fact that the bogus data could masquerade as good data and the date tag on the good data might have been changed by a day when the spurious data were added. Fortunately, this problem was corrected by the Navy by the beginning of February, 1988. Losing more than 10% of the available data during 1987 and early 1988 was not acceptable. Thus, software and operational procedures were developed to detect potential problem files and edit them so that the good data could be retained while maintaining the appropriate quality control.

The last major problem was discovered in data beginning in January, 1988. Apparently, more than ten percent of the FNOC data files suffer from a transmission problem that causes antenna/brightness temperature values in the lower five channels to alternate between reasonable values and values that are either extremely high (by hundreds of degrees Kelvin) or unrealistically low. This effect usually begins at the start of an FNOC data file and can last a few scans or a complete orbit. Although a significant percentage of FNOC files have this problem, only a few percent of the data are actually questionable. The software developed by JPL/NODS to deal with the data recorder problem was modified to detect and remove the corrupted data resulting from the suspected transmission problem.

### 3.4. Data Archiving Activities

During the validation period, JPL/NODS distributed more than 700 tapes of SSM/I data to the NASA SSM/I validation team. The active involvement of JPL/NODS in the processing and archiving of SSM/I sea ice data ended in September 1989 with the transfer of all processing, archiving, and data distribution responsibilities to NSIDC. JPL/

NODS had completed loading nearly a year's worth of gridded and swath data (July 9, 1987 - May 14, 1988). In addition, major software changes had been made to the original system since the data loading was started. These included changes to permit the removal of suspect data, the loading of the compact antenna temperature data, and the correction of the geolocation values. In addition, procedures for loading the SSM/I data were significantly improved.

The NSIDC started processing the post May 1988 data into grids soon after delivery of the revised NODS software in October 1989. Since then NSIDC has completed grid production from May 1988 to December 1990. The rapid-access archive swath data sets produced by JPL/NODS were successfully merged with the NSIDC SSM/I archives in October 1989. As of August 1991, ten volumes of SSM/I gridded TB data have been issued.

### 3.5 References

National Aeronautics and Space Administration, Science Working Group for the Special Sensor Microwave Imager (NASA-SWG), *Passive Microwave Remote Sensing for Sea Ice Research*, 55 pp., Washington, D.C., 1984.

Weaver, R., C. Morris, and R. G. Barry, Passive Microwave Data for Snow and Ice Research: Planned Products from the DMSP SSM/I System, *Eos*, 776, September 29, 1987.

## Chapter 4

### SEA ICE ALGORITHM

Donald J. Cavalieri  
Laboratory for Hydrospheric Processes  
NASA Goddard Space Flight Center  
Greenbelt, Maryland 20771

4.1 Algorithm Description .....	25
4.2 SSM/I Tie-points .....	26
4.3 Algorithm Sensitivity and Sources of Error .....	28
4.4 References .....	30

#### 4.1 Algorithm Description

In 1985 the NASA Sea Ice Algorithm Working Group (NSAWG) reviewed the state of passive microwave sea ice algorithm development for the purpose of recommending an algorithm for deriving sea ice products from the new DMSP SSM/I. The NSAWG chose three candidate algorithms that had been developed and tested, and selected one of these for processing the SSM/I data. A description of each of the three candidate algorithms and the rationale for selecting the NASA Team algorithm are summarized in Swift and Cavalieri (1985).

The three SSM/I channels used in calculating sea ice concentration with the NASA algorithm are the 19.4-GHz horizontally (H) and vertically (V) polarized channels and the V-polarized 37.0-GHz channel. This algorithm is functionally the same as the Nimbus 7 SMMR algorithm described by Cavalieri et al. (1984) and Gloersen and Cavalieri (1986). The SSM/I radiances from each of the three channels are first mapped onto polar stereographic grids (the so-called SSM/I grid). The gridded radiances are then used to calculate grids for the two independent variables used in the algorithm. These are the polarization (PR) and spectral gradient ratio (GR) defined by

$$PR = [TB(19V) - TB(19H)] / [TB(19V) + TB(19H)] \quad (4.1)$$

$$GR = [TB(37V) - TB(19V)] / [TB(37V) + TB(19V)] \quad (4.2)$$

where TB is the observed brightness temperature at the indicated frequency and polarization. From these two parameters the first-year ice concentration ( $C_F$ ) and the multiyear ice concentration ( $C_M$ ) are calculated from the following equations:

$$C_F = (a_0 + a_1 PR + a_2 GR + a_3 PR \cdot GR) / D \quad (4.3)$$

$$C_M = (b_0 + b_1 PR + b_2 GR + b_3 PR \cdot GR) / D \quad (4.4)$$

$$\text{where } D = c_0 + c_1 PR + c_2 GR + c_3 PR \cdot GR \quad (4.5)$$

The total ice concentration ( $C_T$ ) is the sum of the first-year and multiyear concentrations

$$C_T = C_F + C_M \quad (4.6)$$

The coefficients  $a_i$ ,  $b_i$ , and  $c_i$  ( $i = 0, 3$ ) are functions of a set of nine TBs. These TBs, referred to as algorithm tie-points, are observed SSM/I radiances over areas of known ice-free ocean, first-year (FY) sea ice, and multiyear (MY) ice for

each of the three SSM/I channels. The algorithm tie-points, as well as the coefficients in Equations 4.3 to 4.5, are given in Table 4.1. The reasons for dropping the FY and MY ice nomenclature and for calculating only  $C_1$  for the Antarctic are discussed in the next section.

Table 4.1. NASA DMSP SSM/I Sea Ice Algorithm Tie-points and the Coefficients Used in the Calculation of Sea Ice Concentrations

Northern Hemisphere				
<u>Channel</u>	<u>OW</u>	<u>FYice</u>	<u>MYice</u>	
19.4H	100.8	242.8	203.9	
19.4V	177.1	258.2	223.2	
37.0V	201.7	252.8	186.3	
$a_0 = 3286.56$	$a_1 = -20764.9$	$a_2 = 23893.1$	$a_3 = 47944.5$	
$b_0 = -790.321$	$b_1 = 13825.8$	$b_2 = -33104.7$	$b_3 = -47720.8$	
$c_0 = 2032.20$	$c_1 = 9241.50$	$c_2 = -5655.62$	$c_3 = -12864.9$	
Southern Hemisphere				
<u>Channel</u>	<u>OW</u>	<u>Ice Type A</u>	<u>Ice Type B</u>	
19.4H	100.3	237.8	193.7	
19.4V	176.6	249.8	221.6	
37.0V	200.5	243.3	190.3	
$a_0 = 3055.00$	$a_1 = -18592.6$	$a_2 = 20906.9$	$a_3 = 42554.5$	
$b_0 = -782.750$	$b_1 = 13453.5$	$b_2 = -33098.3$	$b_3 = -47334.6$	
$c_0 = 2078.00$	$c_1 = 7423.28$	$c_2 = -3376.76$	$c_3 = -8722.03$	

In addition to constraining the solutions to concentrations between 0% and 100%, the algorithm also sets the total ice concentration to 0% for those SSM/I grid cells with GR greater than 0.05. This serves to reduce spurious ice concentrations caused by weather-related effects at polar latitudes. Wind-roughened seas, cloud-liquid water, and atmospheric water vapor all contribute to these spurious concentrations over the open ocean. This so-called weather filter also eliminates ice concentrations below 15%. This is not considered a serious limitation, since the ice edge has been defined previously for satellite passive-microwave imagery as the 15% ice concentration contour (e.g., Zwally et al., 1983, and Parkinson et al., 1987). Furthermore, a comparison of aircraft-determined ice-edge positions with SSM/I ice concentrations shows that the location of the ice-edge position is accurately determined by the 15% ice-concentration contour (see Chapter 7).

#### 4.2 SSM/I Tie-points

The monthly-mean sea ice concentrations illustrated in Color Plates 1 and 2 were calculated using the tie-points in Table 4.1. The selection of these tie-points was based on an analysis of SSM/I TBs, PR-GR distributions, and histograms of sea ice concentrations, and on comparisons with near simultaneous measurements from the Nimbus-7 SMMR during July and August 1987 (see Preface). The two sets of SSM/I tie-points (one for the northern hemisphere and one for the southern hemisphere) represent a "global" set designed for mapping global ice concentrations. While

this “global” set of tie-points provides a uniform measure of sea ice concentration on the large scale, improved accuracy is obtained with the use of regionally selected tie-points (Chapter 5).

The ice-free (open water) tie-points were chosen to be near minimum ice-free ocean TBs (corresponding to near maximum values of PR). By choosing near minimum TBs, the PR range between open water and FY ice is about an order of magnitude that permits greater algorithm sensitivity for detecting changes in ice concentration. Although the Arctic and Antarctic open water tie-points were selected independently, the TB difference for corresponding channels is no more than about 1 K (see Table 4.1).

The ice tie-point selection was more difficult, since the passive-microwave ice signatures depend on region and season. This is particularly true of MY ice. Even for a given region and season there is a certain amount of random variability for a given ice type. Thus, there is generally a range of TBs that could be used as tie-points. The series of SSM/I aircraft underflights helped in this regard. Mosaic patterns covering several SSM/I image pixels were flown in the central Arctic over a 2-week period in March 1988. Although the mosaicked aircraft data did not provide radiometric coverage at the SSM/I frequencies and polarizations, it did provide a constraint on the ice concentrations, which were calculated from passive- and active-microwave imagery (see Chapters 8 and 9). This allowed adjustment of the ice tie-points within the range of allowable values to improve the accuracy to within a few percent (relative to the aircraft data).

The need for different Arctic and Antarctic tie-points is best illustrated through the use of PR-GR plots. Figure 4.1 shows typical PR-GR plots for both the Arctic and Antarctic during winter. The PR-GR distributions in Figure 4.1, a (March 22, 1988), and in Figure 4.1, b (September 25, 1987), are typical of winter conditions. The Arctic and Antarctic tie-points are plotted on their respective distributions. For the Arctic (Figure 4.1, a), the points are labeled OW, FY, and MY and correspond to regions of open water, FY ice, and MY ice, respectively. In Figure 4.1, b, the tie-points are labeled

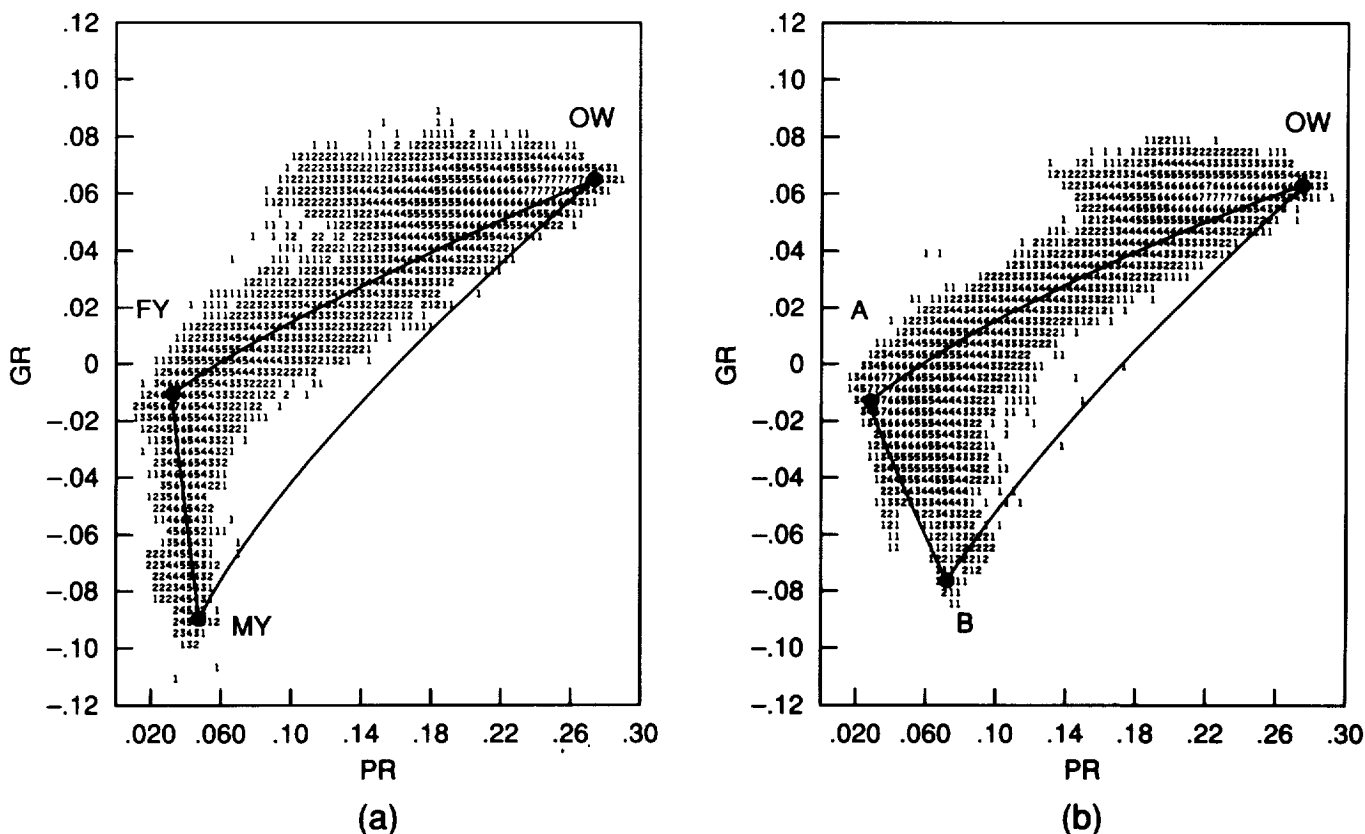


Figure 4.1. PR-GR distribution for (a) the Arctic on March 22, 1988, and (b) the Antarctic on September 25, 1987.

OW, A, and B for reasons described later. These tie-points define the vertices of nonlinear triangles which are representations of the algorithm in PR-GR space.

The Arctic FY-MY cluster (Figure 4.1, a) is almost vertical and extends to more negative GR values than does the corresponding Antarctic cluster (Figure 4.1, b), which is skewed to the right. There are also more points distributed along and scattered about the upper leg of the Antarctic algorithm triangle. This is caused, in part, to the greater amount of ocean area covered by the SSM/I grid and, in part, to the more diffuse nature of the Antarctic marginal ice zone. There are also many more points distributed within the Antarctic triangle at concentrations less than 90%, in contrast to the Arctic distribution.

The primary reason for the difference between the Arctic MY tie-point and the Antarctic Type B tie-point is that in the Antarctic, the radiometric distinction between first-year (seasonal) ice and multiyear (perennial) ice is lost. Unlike the Arctic, where the predominant source of negative gradient ratios is the volume scattering by the empty brine pockets in the freeboard portion of multiyear ice, in the Antarctic, the main source of volume scattering is from sources other than multiyear ice. One very likely source of volume scattering is the snow cover on the sea ice. Snow cover of sufficient depth and of sufficiently large grain size will mimic the signature of multiyear ice (see Chapter 7). It has been observed that the physical characteristics of Antarctic sea ice are different from those in the Arctic (Ackley et al., 1980; Wadhams et al., 1987), implying a corresponding difference in microwave radiance characteristics for the two polar regions.

### 4.3 Algorithm Sensitivity and Sources of Error

#### 4.3.1 Algorithm Sensitivity

The sensitivity of the algorithm to random errors has been described previously (Swift and Cavalieri, 1985) for the SMMR version of the algorithm. The sensitivity analysis was redone using the SSM/I algorithm coefficients in Table 4.1. The results are presented in Tables 4.2 and 4.3 for the Arctic and Antarctic sets of tie-points, respectively. The sensitivity coefficients given in Table 4.2 were calculated for regions of FY ice and MY ice in the Arctic at three different ice concentrations. This was repeated for the Antarctic with ice type regions labeled A and B. Each coefficient represents the uncertainty in concentration in units of percent per 1 K uncertainty in TB. The total root-summed-square (rss) sensitivity is also given for each concentration.

The coefficients given in Tables 4.2 and 4.3 may be used to obtain an estimate of the error incurred by variations in the radiometric properties of the ice surface. For example, a random variation in ice emissivity of  $\pm 0.01$  over 100% FY ice corresponds to a variation in TB of 2.5 K (assuming a value of 250 K for the physical temperature of the radiating portion of the ice), which, in turn, corresponds to an error of  $\pm 4.5\%$  ( $\pm 0.018 \times 2.5$ ) in total ice concentration, assuming all three channels are subject to this variation.

The sensitivity of the calculated ice concentrations to ice temperature variations is reduced through the use of radiance ratios PR and GR (Cavalieri et al., 1984; Swift and Cavalieri, 1985). Except at the onset of melt, there is no apparent correlation between PR and the increasing TBs resulting from seasonal warming. This is not the case for GR, which is correlated with the seasonal variation in TB. An estimated error of  $\pm 0.005$  in GR (Gloersen et al., 1992) corresponds to an uncertainty in total ice concentration of about  $\pm 1\%$ , while the error in MY ice concentration is about  $\pm 9\%$ . These estimated errors are consistent with the results obtained from the comparative studies presented in Chapters 5, 7, 8, and 9.

#### 4.3.2 Sources of Error

Errors in the derived sea ice concentrations arise from several sources. In order of importance, these are (1) the inability of the algorithm to discriminate among more than two radiometrically different sea ice types, (2) seasonal variations in sea ice emissivity, (3) nonseasonal variations in sea ice emissivity, (4) weather effects at concentrations greater than 15%, and (5) random and systematic instrument error.

Table 4.2. NASA SSM/I Algorithm Sensitivity Coefficients\* for Both First-year and Multiyear Ice Regions of the Arctic at Different Concentrations

First-year Ice						
	100%		50%		15%	
	$\delta C_T$	$\delta C_{MY}$	$\delta C_T$	$\delta C_{MY}$	$\delta C_T$	$\delta C_{MY}$
$\delta TB_{19H}$	1.4	1.2	1.1	1.2	0.9	1.2
$\delta TB_{19V}$	1.1	4.0	0.4	4.0	0.0	4.0
$\delta TB_{37V}$	0.3	2.9	0.4	2.9	0.5	2.9
$[\Sigma(\delta TB)^2]^{1/2}$	1.8	5.1	1.2	5.1	1.0	5.1
Multiyear Ice						
	100%		50%		15%	
	$\delta C_T$	$\delta C_{MY}$	$\delta C_T$	$\delta C_{MY}$	$\delta C_T$	$\delta C_{MY}$
$\delta TB_{19H}$	1.4	0.6	1.0	0.6	0.7	0.5
$\delta TB_{19V}$	1.1	2.8	0.4	2.5	0.0	2.2
$\delta TB_{37V}$	0.3	2.6	0.4	2.3	0.4	2.1
$[\Sigma(\delta TB)^2]^{1/2}$	1.8	3.9	1.2	3.4	0.8	3.1

\*Each coefficient represents the uncertainty in concentration in units of percent per 1-K uncertainty in brightness temperature.

Table 4.3. NASA SSM/I Algorithm Sensitivity Coefficients\* for Both Ice Type A and Ice Type B Regions of the Antarctic at Different Concentrations

Ice Type A				Ice Type B		
	100%	50%	15%	100%	50%	15%
	$\delta C_T$	$\delta C_T$	$\delta C_T$	$\delta C_T$	$\delta C_T$	$\delta C_T$
$\delta TB_{19H}$	1.2	0.9	0.8	1.2	0.8	0.6
$\delta TB_{19V}$	0.3	0.1	0.5	0.3	0.1	0.4
$\delta TB_{37V}$	0.8	0.8	0.9	0.8	0.8	0.8
$[\Sigma(\delta TB)^2]^{1/2}$	1.5	1.2	1.3	1.5	1.1	1.1

\*Each coefficient represents the uncertainty in concentration in units of percent per 1-K uncertainty in brightness temperature.

The largest source of error is the inability of the algorithm to discriminate among more than two radiometrically different sea ice types (including different surface conditions). The broad categories of radiometrically different sea ice types are new and young ice, FY ice, and MY ice types. Since the algorithm allows for both FY and MY ice types, the largest source of error in total ice concentration is caused by the presence of newly forming sea ice. New and young ice, most commonly found in leads and coastal polynyas during winter, is characterized by polarization differences

intermediate between open water and thick FY ice (Cavalieri et al., 1986). PR for thin ice will vary in proportion to ice thickness (Grenfell and Comiso, 1986) and will increase in proportion to the fraction of new ice filling the SSM/I FOV. For example, if we presume that an FOV contains 10% new ice (PR = 0.14) and 90% FY ice (PR = 0.03), then the increase in PR results in an underestimate of about 10% in total ice concentration. Larger areas of new ice within the sensor FOV will result in proportionally larger underestimates by the algorithm.

Seasonal variations in sea ice emissivities can be extremely large. MY ice, for example, loses its characteristic microwave spectral signature (negative GR) during spring and summer and becomes indistinguishable from FY ice. Another condition resulting in large errors in total ice concentration is the formation of melt ponds on the ice surface, making the ponded region indistinguishable from open water. While the areal extent of ponding is not well known, unpublished data (Carsey, 1982) show that for the summer of 1975, 20% or less of the Arctic ice pack was covered by ponds and that ponding reached maximum areal extent in early July. The extent to which surface moisture and ponding affects the summer ice concentrations remains uncertain without additional information. These melt effects vary spatially and temporally across the Arctic.

Nonseasonal variations in sea ice emissivity include local variations, resulting from fluctuations in the physical and chemical properties of sea ice, and regional variations resulting from environmental differences. Regional and hemispheric variability may be considerable, as indicated by previous studies (Comiso, 1983; Ackley, 1979). Differences between Arctic and Antarctic sea ice microwave signatures noted in Section 4.2 result in different sets of algorithm tie-points for each hemisphere. Algorithm errors can be reduced by using locally and seasonally chosen algorithm tie-points (e.g., see Chapter 5).

Weather effects resulting from atmospheric water vapor, cloud-liquid water, and sea-surface roughening by surface winds result in spurious sea ice concentrations over the open ocean. While these effects are reduced at polar latitudes in winter by the algorithm weather filter described in Chapter 4, there remain serious weather contamination problems at all latitudes in summer. These problems are more serious than they were with the Nimbus 7 SMMR because the 19.35-GHz SSM/I channels are about halfway up the wing of the water-vapor line at 22.2 GHz compared to the 18.0-GHz SMMR channels which are about a third of the way up.

Even in winter, weather effects may be a source of sea ice-concentration error at concentrations greater than 15%. Presuming that the atmospheric contribution is nearly zero at the FY ice end of the triangle in winter (Figure 4.1), and that the contribution at the open-water end results totally from atmospheric effects estimated to be up to 15%, then the error resulting from atmospheric effects for any intermediate concentration may be estimated by a linear interpolation.

Finally, errors in ice concentration also result from random and systematic instrument errors. Except for the 85-GHz channels, over the 2 years of SSM/I operation, no instrument drifts are apparent. Based on prelaunch measurements and on observed radiances over relatively stable targets where temporal and spatial geophysical variability is small, the error for each of the three SSM/I channels used in the algorithm is less than 1 K, and the absolute accuracy is estimated at 3 K (Hollinger, 1989). Assuming a 1-K level of random instrument noise in each channel, an upper limit to the r.s.s. uncertainty in the calculated concentrations, which depends on surface type and concentration, ranges from about 1% to 1.8% for total ice concentration and from 4.5% to 6% for MY ice concentration.

#### 4.4 References

- Ackley, S. F., Mass balance aspects of Weddell Sea pack ice, *J. Glaciol.*, 24, 391-406, 1979.
- Ackley, S. F., A. J. Gow, K. R. Buck, and K. M. Golden, Sea ice studies in the Weddell Sea aboard USCGC Polar Sea, *Antarctic J.* VV, 84-86, 1980.

- Carsey, F. D., Arctic sea ice distribution at end of summer 1973-1976 from satellite microwave data, *J. Geophys. Res.*, 87, 5809-5835, 1982.
- Cavalieri, D. J., P. Gloersen, and W. J. Campbell, Determination of sea ice parameters with the Nimbus 7 SMMR, *J. Geophys. Res.*, 89, 5355-5369, 1984.
- Cavalieri, D. J., P. Gloersen, and T. T. Wilheit, Aircraft and satellite passive microwave observations of the Bering Sea cover during MIZEX West, *IEEE Transactions on Geoscience and Remote Sensing*, GE-24, 368-377, 1986.
- Comiso, J. C., Sea ice effective microwave emissivities from satellite passive microwave and infrared observations, *J. Geophys. Res.*, 88, 7686-7704, 1983.
- Gloersen, P., W. J. Campbell, D. J. Cavalieri, J. C. Comiso, C. L. Parkinson, and H. Jay Zwally, *Arctic and Antarctic Sea Ice, 1978-1987: Satellite Passive-Microwave Observations and Analysis*, National Aeronautics and Space Administration, Washington, D.C., in press, 1992.
- Gloersen, P., and D. J. Cavalieri, Reduction of weather effects in the calculation of sea ice concentration from microwave radiance, *J. Geophys. Res.*, 91, 3913-3919, 1986.
- Grenfell, T. C., and J. C. Comiso, Multifrequency passive microwave observations of first-year sea ice grown in a tank, *IEEE Transactions on Geoscience and Remote Sensing*, GE-24, 826-831, 1986.
- Hollinger, J. P., *DMSP Special Sensor Microwave/Imager Calibration/Validation*, Naval Research Labs, Washington, D.C., 1989.
- Parkinson, C. L., J. C. Comiso, H. Jay Zwally, D. J. Cavalieri, P. Gloersen, W. J. Campbell, *Arctic Sea Ice, 1973-1976: Satellite Passive-Microwave Observations*, NASA SP-489, National Aeronautics and Space Administration, Washington, D.C., 1987.
- Swift, C. T., and D. J. Cavalieri, Passive Microwave Remote Sensing for Sea Ice Research, *Eos, Transactions, American Geophysical Union*, Vol. 66, No. 49, December 3, 1985.
- Wadhams, P., M. A. Lange, and S. F. Ackley, The ice thickness distribution across the Atlantic sector of the Antarctic ocean in midwinter, *J. Geophys. Res.*, 92, 14,535-14,552, 1987.
- Zwally H. J., J. C. Comiso, C. L. Parkinson, W. J. Campbell, F. D. Carsey, and P. Gloersen, *Antarctic Sea Ice, 1973-1976: Satellite Passive-Microwave Observations*, NASA SP-459, National Aeronautics and Space Administration, Washington, D.C., 1983.



## Chapter 5

### SSM/I-LANDSAT COMPARISON

Konrad Steffen and Axel J. Schweiger  
Cooperative Institute for Research in Environmental Sciences  
University of Colorado  
Boulder, Colorado 80302

5.1 Landsat Imagery .....	33
5.2 Method .....	34
5.3 Accuracy .....	35
5.4 Ice Classification .....	36
5.5 Results .....	37
5.6 Conclusions .....	44
5.7 References .....	46

#### 5.1 Landsat Imagery

An important component of the validation effort is the comparison of SSM/I total ice concentrations with nearly coincident Landsat MSS imagery for different regions and seasons. A total of 34 Landsat scenes have been received and archived at the National Snow and Ice Data Center (NSIDC) in Boulder, Colorado (Tables 5.1 and 5.2). A total of 28 Landsat scenes (Window L1A1 to L10) have been analyzed, and the results of the Landsat-SSM/I ice-concentration comparison are discussed in this chapter. For the two windows L4 and L5C, cloud cover exceeded 70%; therefore, no comparisons were carried out. For the ice-type classification, two methods were applied.

Table 5.1. Landsat Images for Comparison With DMSP-SSM/I

Window	Date/Path/Row	Type	Area
L1A	87-09-17/75/9,10	1	Beaufort Sea
L1B	87-11-10/77/9,10	1	Beaufort Sea
L2	87-11-29/195/112	2	Weddell Sea
L3A	88-03-12/74/6-8	1	Beaufort Sea Transect
L3B	88-03-16/70/9,10	1	Beaufort Sea Ice Station
L3C	88-03-19/75/9,10	1	Beaufort Sea Mosaic
L3D	88-03-25/77/8	2	Beaufort Sea
L5A	88-03-13/81/15-19	1	Bering Sea
L5B	88-03-21/89/15-17	1	Bering Sea (Soviet side)
L6A	88-06-29/85/11	1	Beaufort Sea
L6B	88-07-01/83/9-11	1	Beaufort/Chukchi Sea
L8	88-09-18/205/103	2	Greenland Sea
L9	88-10-20/84/9	2	Chukchi Sea
L10	90-12-29/20/110	2	Amundsen Sea

Type 1: Landsat MSS, band 5, transparency

Type 2: Landsat MSS, band 4,5,6,7, digital data on tape

Table 5.2. Coordinate and Ice Conditions for Landsat Images Used in Case Studies

Window	Center coordinate		Ice conditions
L1A1	72.15 N	147.09 W	IC(20%), SY MY, FS 80m-40km
L1A2	70.86 N	149.25 W	IC(2%), SY MY, FS 80m-10km
L1B1	72.18 N	150.28 W	IC(90%), MY(50%) YI(40%), FS 2-50km
L1B2	70.90 N	152.44 W	IC(98%), MY(30%) YI (68%), FS 2-5km
L2	73.27 S	38.37 W	IC(85%), FS 80m-10km
L3A1	75.89 N	137.16 W	IC(97%), FY MY, large fracture pattern
L3A2	74.69 N	140.45 W	same as L3A1
L3A3	73.46 N	143.28 W	same as L3A2
L3B1	72.19 N	139.56 W	IC(95%), FY MY, large fracture pattern
L3B2	70.90 N	141.71 W	IC(95%), FY MY, large fracture pattern
L3C1	72.19 N	147.29 W	IC(98%), FY MY, some fractures
L3C2	70.90 N	147.09 W	IC(87%), coastal fractures (polynya)
L3D	73.45 N	147.75 W	IC(95%), large fracture pattern
L5A1	64.22 N	166.41 W	IC(95%), NI(20%) YI(35%) FY(35%)
L5A2	62.85 N	167.54 W	IC(95%), NI(10%) YI(10%) FY(75%)
L5A3	61.47 N	168.59 W	IC(90%), YI(10%), FY(80%)
L5A4	60.09 N	169.55 W	IC(75%), FS 2-60m
L5A5	58.70 N	170.44 W	IC(50%), FS 2-60km, ice edge
L5B1	64.21 N	178.78 W	IC(95%), YI(60%) FY(35%), FS 80m-20km
L5B2	62.84 N	179.71 W	IC(85%), YI(15%) FY(70%), FS 80m-8km
L5B3	61.47 N	180.95 W	IC(60%), YI(40%) FY(20%), ice edge
L6A1	69.60 N	166.84 W	IC(60%), FS 0.5-10km
L6B1	72.20 N	159.70 W	IC(95%), large fracture pattern
L6B2	70.91 N	161.85 W	IC(70%), ice edge area
L6B3	69.60 N	163.74 W	IC(50%), ice edge area
L8	80.73 N	2.83 W	IC(95%), fractures partly frozen
L9	72.18 N	161.08 W	IC(95%), YI(5%), FY(90%)
L10	70.93 N	123.25 W	
Ice Nomenclature			
NI	New ice	YI	Young ice
FY	First-year ice	SY	Second-year ice
MY	Multiyear ice	FS	Floe size
IC	Ice concentrations		

## 5.2 Method

### 5.2.1 Threshold Techniques

Using training areas, the brightness value ranges for different ice types and open water are determined. By selecting appropriate brightness thresholds, an image can be classified into five different ice types. For the determination of ice concentration, the class spectrum comprised open water/dark nilas, light nilas, grey ice, grey-white ice, and white ice, corresponding to a categorization of ice thickness and stages of development commonly used in sea ice research (Steffen, 1986). During summer and fall, when only open water and white ice are present, a "subresolution" class was introduced. Pixels at intensity levels between open water and white ice were interpreted as containing ice floes of

subresolution sizes and put into this class. Following classification, ice concentrations are calculated for the corresponding SSM/I 50- by 50-km grid boxes.

### 5.2.2 Tie-point Algorithm

The algorithm procedure for sea ice concentration calculation from Landsat imagery developed by Comiso and Zwally (1982) is based on the idea that during periods where no new ice formation occurs, the spectrum of classes is reduced to open water and white ice. If open water and white ice are the only two classes that are present, the assumption can be made that all brightness values in between those classes must represent ice concentrations at subresolution. Locations where a known state is assumed (i.e., 100% ice, 100% open water) are known as tie-points. This algorithm thus more realistically accounts for the presence of ice floes smaller than the Landsat Multispectral Scanner (MSS) resolution of 80 m.

$$Ic = (Dx - Dl / Dh - Dl) \cdot 100 \quad (5.1)$$

Ic	=	Ice concentration
Dx	=	Brightness value representing ice concentration
Dl	=	Brightness value for open water
Dh	=	Brightness value for white ice

Tie-points were found using training areas for open water and large white ice floes, where Dh represents the mean brightness for that floe minus one standard deviation.

In the subsequent analysis the tie-point algorithm was used to calculate ice concentrations for images during summer and early fall conditions, when open water/black nilas and white ice were the only present surface classes. For other images, the threshold algorithm was applied.

### 5.3 Accuracy

The accuracy with which ice concentration can be derived from Landsat data is an important factor for the SSM/I validation. Four possible errors are assumed:

- Sensor noise
- Clouds
- Geolocation
- Resolution

#### 5.3.1 Sensor Noise Removal

Landsat MSS image reflectance values are very low because of the low illumination conditions during spring and fall in the Arctic. Despite the high albedo of sea ice surfaces, digital images (CCT) frequently display maximum digital numbers (DN) not exceeding 40. Signal-to-noise ratios, therefore, are enhanced and significant “stitching” interference patterns are noticeable on contrast-stretched digital imagery and photographic film products (Miller and Burger, 1986). A fast fourier transform (FFT) filter was used to remove sensor noise. Examples of this procedure are given by Steffen and Schweiger (1990). The error of derived Landsat ice concentration caused by sensor noise is estimated to be less than 1% after the FFT filter is used.

#### 5.3.2 Clouds

Areas with cloud cover were excluded from the analysis. For this procedure, a conservative approach was used, and, therefore, we assume no additional error caused by cloud cover.

### 5.3.3 Geolocation

Digital Landsat MSS imagery at 80-m resolution (field of view) is geometrically and radiometrically corrected. This imagery can easily be georeferenced, using ancillary information, and regridded to match the SSM/I grid format (polar stereographic projection). Photographic transparencies of Landsat MSS imagery are geometrically corrected for earth rotation, but the frame centerpoint geolocation is unreliable because of the lack of accurate ephemeris and satellite attitude data. Landsat MSS channel 7 data were therefore acquired in swaths so that at least one frame within each swath contains identifiable landmarks. Through point by point comparison with maps and digital coastline data (CIA World Data Bank 2), a geolocation correction can be approximated for the entire path. After application of this procedure, root-mean-square (RMS) differences between control-point locations on imagery and maps amounted to 1.5 km and could be attributed to the inaccuracy of map data in these northern areas. This is acceptable, considering the low resolution of the corresponding passive-microwave data. Transparencies were digitized using a high-resolution scanner and geolocated using the above-outlined procedure and projected to a polar stereographic projection (True at 70° latitude) used for the SSM/I gridded sea ice products. If we consider a geolocated error of 250 m for the Landsat image, the error in ice concentration would be 1% at most.

### 5.3.4 Resolution

Ice features such as leads or ice floes smaller than the Landsat field of view will be misinterpreted, and consequently an error in the derived ice concentration will result. Errors caused by subresolution ice features must be considered. The threshold method classifies different ice types based on different grey levels, which then are used to derive ice concentration. For subresolution ice features (e.g., open water lead in white ice), a young ice type will be classified based on the grey level. A theoretical error was calculated for different floe sizes and different lead frequencies. For simplicity, it is assumed that the leads are always parallel, and the ice floes are rectangular. In the model, it is assumed that the border pixel of ice floes or leads is misclassified as young ice instead of ice-free. Figure 5.1 shows the theoretical error in ice concentration for different floe sizes and for varying distances between leads. The maximum errors caused by subresolution ice features for all windows are given in the same graph for which the threshold method was applied. From this analysis, it can be assumed that the error caused by resolution does not exceed 3% to 4% at most. For the tie-point method, which includes subresolution information, the error is estimated to be 4 times less.

Landsat ice concentration can be derived with an accuracy of 2% to 4%, considering all possible errors such as sensor noise, geolocation, and resolution.

### 5.4 Ice Classification

Mapping of sea ice parameters using passive-microwave data is possible because of the large difference in emissivity between calm water and sea ice. In addition, the differences in emissivity of first-year versus old ice (sea ice that has survived at least one melt season) at different microwave frequencies provide a means of separating ice types. The capabilities of passive-microwave data in sea ice research have been discussed in a number of articles (Svendsen et al., 1983; Comiso, 1983; 1986; Cavalieri et al., 1984; Gloersen and Cavalieri, 1986). The derivation of ice concentrations from the SSM/I data was carried out using the algorithm described by Cavalieri et al. (1984), with the addition of the weather filter as discussed by Gloersen and Cavalieri (1986).

Tie-points, which are brightness temperature values of open water (TBW), first-year ice (TBF), and multiyear ice (TBM) as observed by the satellite, including atmospheric effects, are critical for the accurate performance of the ice-concentration retrieval algorithm. They are empirically determined based on statistics of hemispheric brightness temperatures (see Chapter 4). If such "globally" chosen tie-points are used for the calculation of ice concentration and multiyear ice fraction, the variation of TBW, TBF, and TBM over time and space are ignored. However, there are large variations in TBW along the ice edge and in open and very open pack ice areas, caused by various effects, including surface roughness, foam, and atmospheric water vapor content. A combination of these tends to increase the brightness temperature of the ocean by as much as 40 K. Also TBF is affected by spatial and temporal variations in physical

temperature (Steffen and Maslanik, 1988), characteristics of emitting surface, and atmospheric conditions. "Locally" derived tie-points were also applied in this study using the following procedure. At least ten 25- x 25-km grid cells of open water were averaged near the ice edge over 1 to 3 days and used as water tie-point (TBW). To select tie-points (TBF) the highest brightness temperature values for the two frequencies and two polarizations were chosen for a larger geographic region (e.g., Beaufort Sea). For the selection of multiyear tie-points (TBM), some local knowledge of the area is necessary, since multiyear ice is not always found in the marginal seas. It is best to select an area in the Arctic Ocean north of 80° and choose the region with the lowest brightness temperature values. In order to locate areas of first-year ice and multiyear ice, SSM/I brightness temperatures were displayed using the SSM/I image display software that was developed for this purpose. Ice concentrations were then calculated with the above-described NASA Team algorithm using "global" and "local" tie-points determined with the above-described procedure. Tie-points used for the individual case studies are listed in Table 5.3.

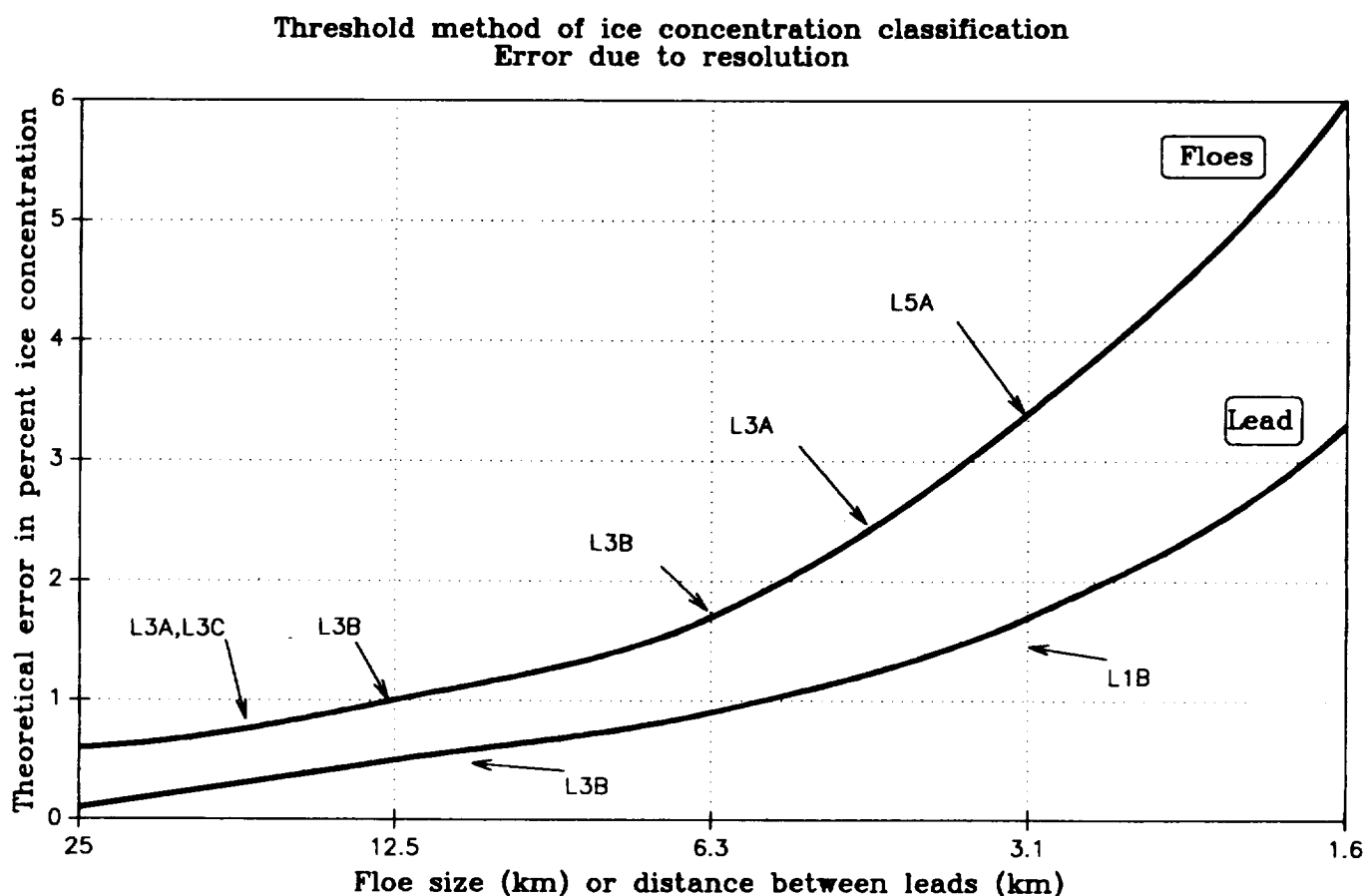


Figure 5.1. Maximum error for Landsat ice concentration derived with threshold method for different floe sizes and distances between leads. Individual case studies (windows) are given in graph (e.g. L5A, see also Table 5.1).

## 5.5 Results

SSM/I swath data were corrected for geolocation inaccuracy with the linear Swift/Steffen orbit correction procedure. The analysis was carried out for two different grid sizes, 25- x 25-km and 50- x 50-km; whereas, the 50-km grid is defined as standard for SSM/I ice-concentration products and will be presented in this report.

Table 5.3. Tie-Points Used in the Sensitivity Study of Passive-Microwave Sea Ice Concentration Algorithm to the Selection of Globally Versus Locally Adjusted Values

Channel	GLOBAL	L1A	L1B	L3A	L3B	L3C	GLOBAL	L2	L10
	N. H.						S.H.		
19V OW	177.1	187	185	177	182	182	176.6	177	178
19V FY	258.2	245	252	258	254	254	249.8	266	260
19V MY	223.2	222	222	228	218	225	221.6	222	222
19H OW	100.8	120	115	100	110	110	100.3	103	106
19H FY	242.8	230	232	241	238	238	237.8	254	240
19H MY	203.9	202	202	204	198	210	193.7	202	194
37V OW	201.7	205	205	200	204	206	200.5	202	200
37V FY	252.8	250	250	255	250	244	243.3	261	250
37V MY	186.3	184	184	196	188	210	190.3	184	190
Channel	GLOBAL	L3D	L5A	L5B	L6A	L6B	L8	L9	
	N.H.								
19V OW	177.1	178	184	178	185	184	178	178	
19V FY	258.2	248	257	256	258	255	251	256	
19V MY	223.2	224	222	222	248	245	224	223	
19H OW	100.8	106	102	100	108	106	107	102	
19H FY	242.8	234	238	236	248	246	234	236	
19H MY	203.9	204	202	202	238	235	203	203	
37V OW	201.7	200	204	202	205	202	205	202	
37V FY	252.8	242	254	254	254	254	250	254	
37V MY	186.3	185	184	184	246	246	190	186	

Nine case studies (in the following called "windows") were analyzed for the Beaufort Sea region covering an ice-concentration range from 0% to 100% during spring, summer, and fall, two windows from the Bering Sea in spring, and one window in fall from the Greenland Sea. Two additional windows for the southern hemisphere were analyzed, one in spring from the Weddell Sea, and one in summer from the Amundsen Sea. The results are subdivided by areas and season as indicated below. In the following statistical analyses, the Landsat ice concentrations were considered as the reference value, and the SSM/I-derived ice concentrations were the model input. The difference in ice concentration is defined as SSM/I ice concentration minus Landsat ice concentration, and the standard deviation represents the standard deviation of the differences.

#### 5.5.1 Beaufort and Chukchi Seas

Fall condition: The analysis shows a mean difference of SSM/I- and Landsat-derived ice concentrations for 50- x 50-km grid cells of 0.1% and a median of 0.0% along the ice edge of the Beaufort Sea during fall (Sept. 17, Nov. 10, 1987) and in the Chukchi Sea (Oct. 20, 1988) with local tie-points. The mean difference increases to 0.6% with a median of 2.0% using global tie-points (Figure 5.2). Ice concentrations derived with global tie-points overestimated at low concentrations and underestimated at high concentrations compared to Landsat-derived values.

Beaufort and Chukchi seas, fall 1987 and 1988

Statistics of SSM/I ice concentration minus Landsat ice concentration expressed as a percent for local and global tie-points (TP). (# cases: number of 50- x 50-km grid cells used in the comparison)

	mean	median	sd	min	max	# cases
Local TP	0.1	0.0	3.5	-9.7	5.9	21
Global TP	0.6	2.0	7.4	-13.7	13.8	21

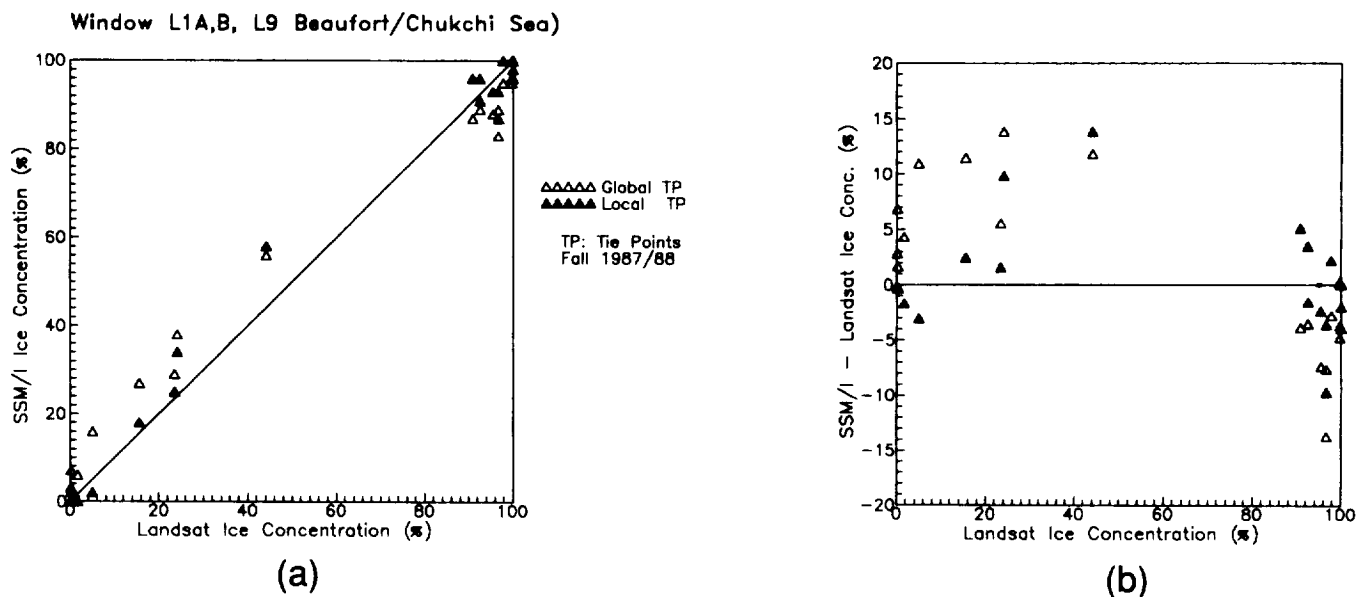


Figure 5.2. Comparison of Landsat sea ice concentrations for the Beaufort Sea under fall ice conditions (Windows L1A, L1B - Sept. 17 and Oct. 10, 1987; Window L9 - Oct. 20, 1988) with (a) SSM/I 50-km grid values using the NASA Team algorithm with local and global tie-points and (b) SSM/I minus Landsat concentrations.

Spring condition: For the spring ice cover in the Beaufort Sea (March 12, 16, 19, 25, 1988), the mean difference for 50-km grid cells in Landsat and SSM/I ice concentrations was -0.2%, and the median was 0.0% with locally chosen tie-points. The same comparison with globally chosen tie-points showed a mean difference of -2.1% with values between -9.7% and 2.9% (Figure 5.3).

#### Beaufort Sea, spring 1988

Statistics of SSM/I ice concentration minus Landsat ice concentration expressed as a percent for local and global tie-points (TP). (# cases: number of 50- x 50-km grid cells used in the comparison)

	mean	median	sd	min	max	# cases
Local TP	-0.2	0.0	2.9	-7.8	7.9	33
Global TP	-2.1	1.8	3.1	-9.7	6.0	33

Summer condition: The ice concentration of pack ice in summer is affected by strong surface winds that break up ice floes into ice fragments. Therefore, ice concentration may change within a few hours by several tenths of a percent. Landsat and DMSP satellite orbits over the Beaufort and Chukchi seas are 6 hours apart. A time series of DMSP Optical Line Scanner (OLS) images from the same time period over the area of investigation showed that ice floes moved as much as 50 km within 6 hours because of strong north-easterly winds. This explains part of the bad correlation of ice concentrations derived from Landsat and DMSP data (Figure 5.4). Locally chosen tie-points did improve the mean difference significantly; however, the standard deviation remained at 22%.

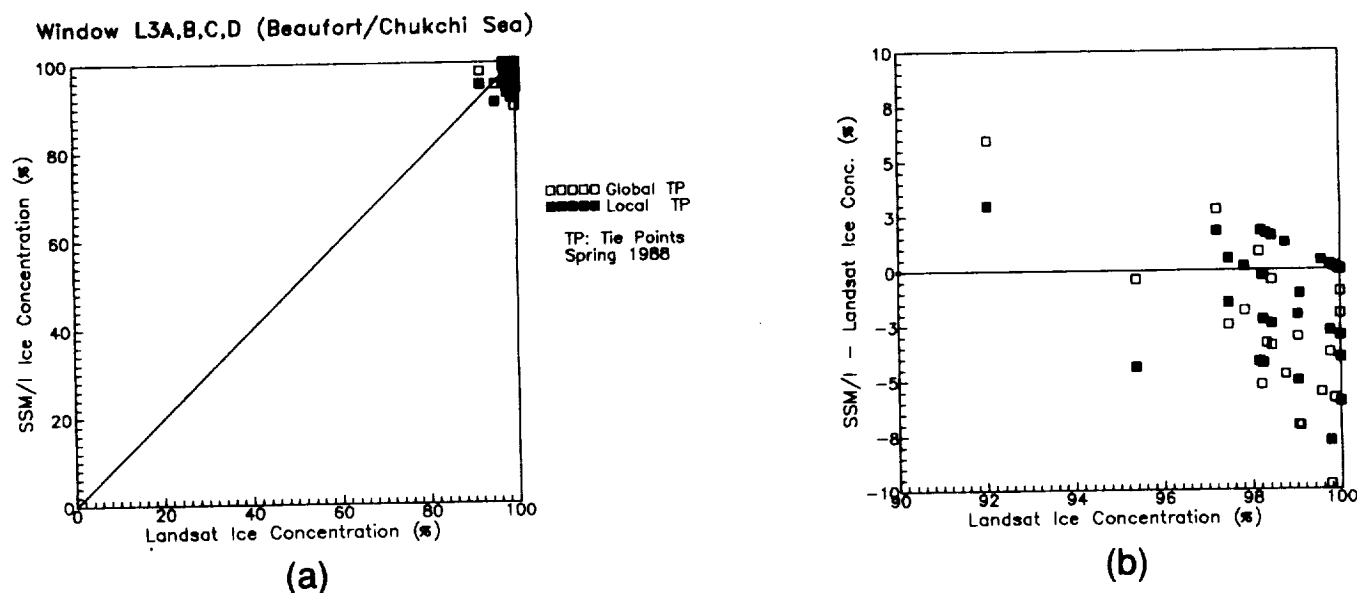


Figure 5.3. Comparison of Landsat sea ice concentrations for the Beaufort Sea under spring ice conditions (Windows L3A to L3D - March 12, 16, 19, and 25, 1988) with (a) SSM/I 50-km grid values using the NASA Team algorithm with local and global tie points and (b) SSM/I minus Landsat concentrations.

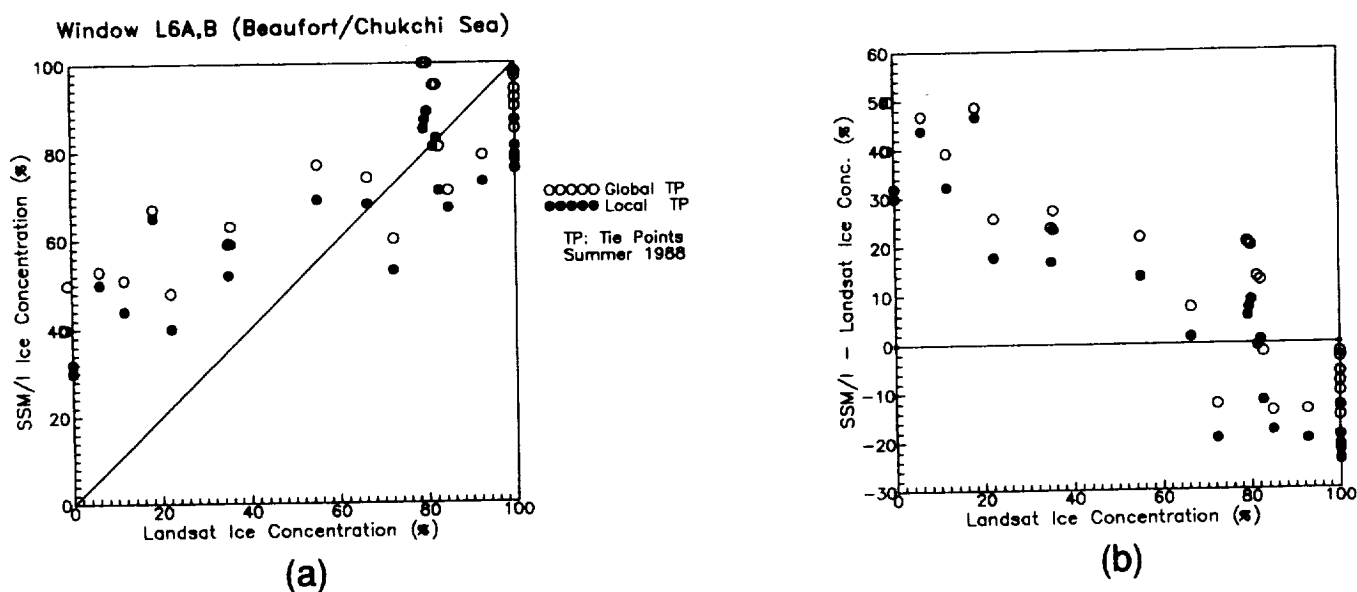


Figure 5.4. Comparison of ice concentration (50-km grid) between NASA Team algorithm using local and global tie-points versus Landsat values for the Beaufort and Chukchi Sea summer ice condition (Windows L6A, L6B - June 29 and July 1, 1988).

Beaufort and Chukchi seas, summer 1988

Statistics of SSM/I ice concentration minus Landsat ice concentration in percent for local and global tie-points (TP). (# cases: number of 50- x 50-km grid cells used in the comparison)

	mean	median	sd	min	max	# cases
Local TP	3.8	1.5	22.3	-24.0	46.6	25
Global TP	11.0	13.5	22.9	-20.0	50.1	25

### 5.5.2 Bering Sea

Spring condition: For the spring ice cover in the Bering Sea (March 13 and 21, 1988), a mean difference of -3.8% for local tie-points and of -9.4% for global tie-points was found for SSM/I and Landsat ice concentrations (Figure 5.5). This difference—even with locally chosen tie-points—reveals some limitations of the NASA Team algorithm under freeze-up condition. Polarization ratios of new ice and nilas range between 0.05 and 0.2 for 19 GHz (Steffen and Maslanik, 1988). Therefore, the NASA Team algorithm underestimates ice concentrations when new ice and nilas are covering large areas.

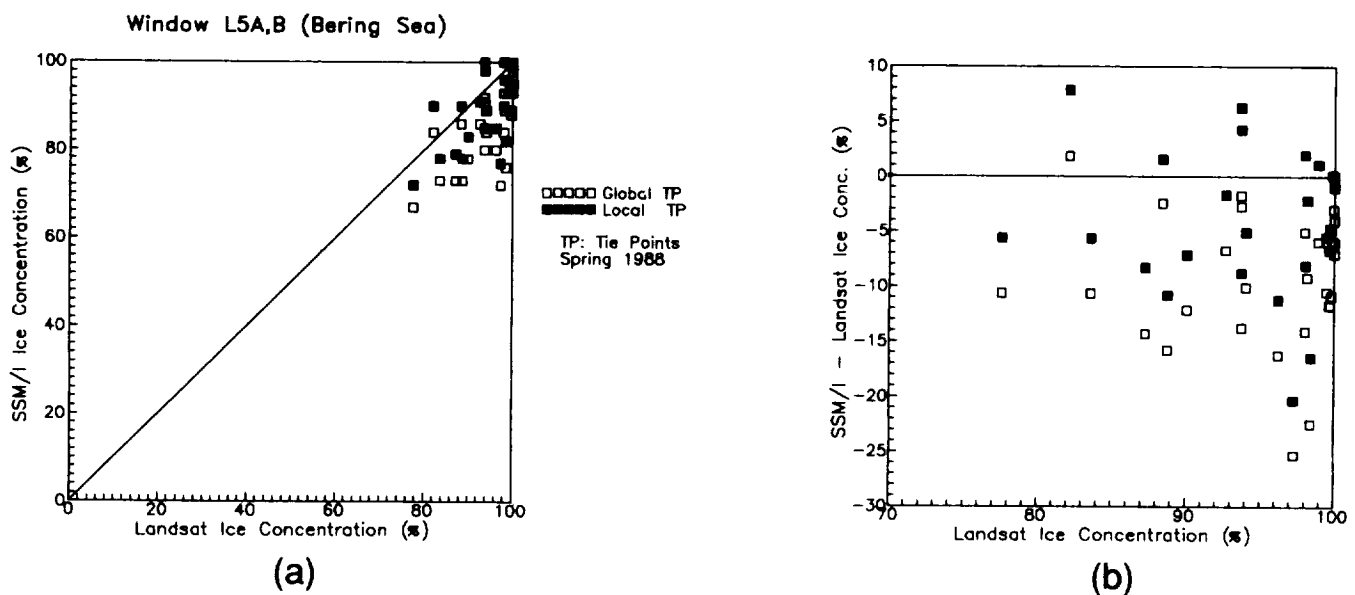


Figure 5.5. Comparison of ice concentration (50-km grid) between NASA Team algorithm using local and global tie-points versus Landsat values for the Bering Sea spring ice condition (Windows L5A, L5B - March 13 and 21, 1988).

### Bering Sea, young ice and first-year ice, spring 1988

Statistics of SSM/I ice concentration minus Landsat ice concentration expressed as a percent for local and global tie-points (TP). (# cases: number of 50- x 50-km grid cells used in the comparison)

	mean	median	sd	min	max	# cases
Local TP	-3.8	4.2	6.3	-20.3	7.9	29
Global TP	-9.4	-10.1	6.1	-25.3	1.9	29

### 5.5.3 Greenland Sea

Fall condition: In the Greenland Sea, SSM/I ice concentrations derived with locally chosen tie-points are, on the average, only -0.3% higher than Landsat-derived values. Ice concentrations calculated using global tie-points show a mean difference of -3.7% (Figure 5.6).

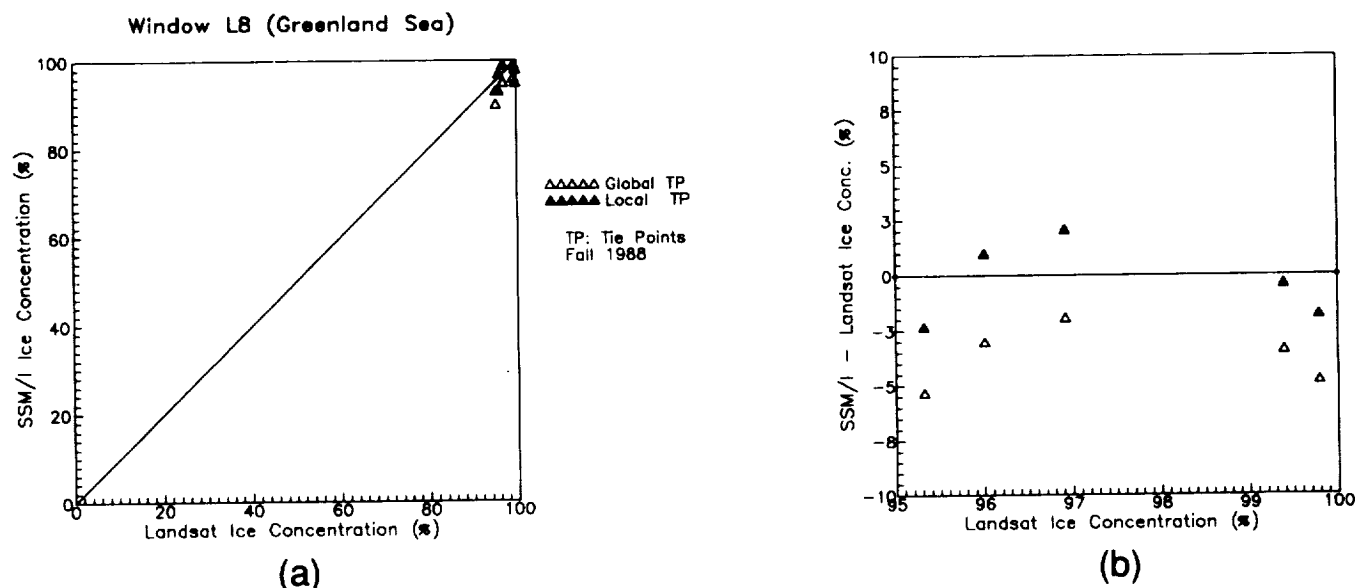


Figure 5.6. Comparison of ice concentration (50-km grid) between NASA Team algorithm using local and global tie-points versus Landsat values for the Greenland Sea fall ice condition (Window L8 - Sept. 25, 1988).

#### Greenland Sea, fall 1988

Statistics of SSM/I ice concentration minus Landsat ice concentration expressed as a percent for local and global tie-points (TP). (# cases: number of 50- x 50-km grid cells used in the comparison)

	mean	median	sd	min	max	# cases
Local TP	0.3	0.4	1.8	-2.1	2.3	5
Global TP	-3.7	-4.4	1.4	-5.3	1.9	5

#### 5.5.4 Weddell Sea

Comparison of southern hemisphere ice concentrations is limited to two case studies. For the Weddell Sea (Nov. 29, 1987) global tie-points perform quite well, and the mean difference between Landsat- and SSM/I-derived concentrations is only -1.1%. With local tie-points, an improvement was achieved (Figure 5.7). The Weddell Sea case study was the only successful validation for that area. A second Landsat MSS image showed a homogeneous ice cover with only a few percent of open water (less than 5%); whereas, the SSM/I-derived ice concentrations were in the range of 65% to 75% for the entire scene. We could not explain this large discrepancy; none of the remaining 27 cases shows such a constant shift. We speculate that either the SSM/I data had, for some reason, a large geolocation error, or the compact ice surface of that area, which was located near the ice margin, became wet by ocean swell leading to greatly altered emission properties in the passive-microwave frequencies. Because this problem has not been resolved, this case study was not included in the overall statistics of this analysis.

#### Weddell Sea, spring 1987

Statistics of SSM/I ice concentration minus Landsat ice concentration expressed as a percent for local and global tie-points (TPs). (# cases: number of 50- x 50-km grid cells used in the comparison)

	mean	median	sd	min	max	# cases
Local TP	0.8	0.0	3.1	-4.2	5.8	7
Global TP	-1.1	1.0	3.1	-3.2	6.8	7

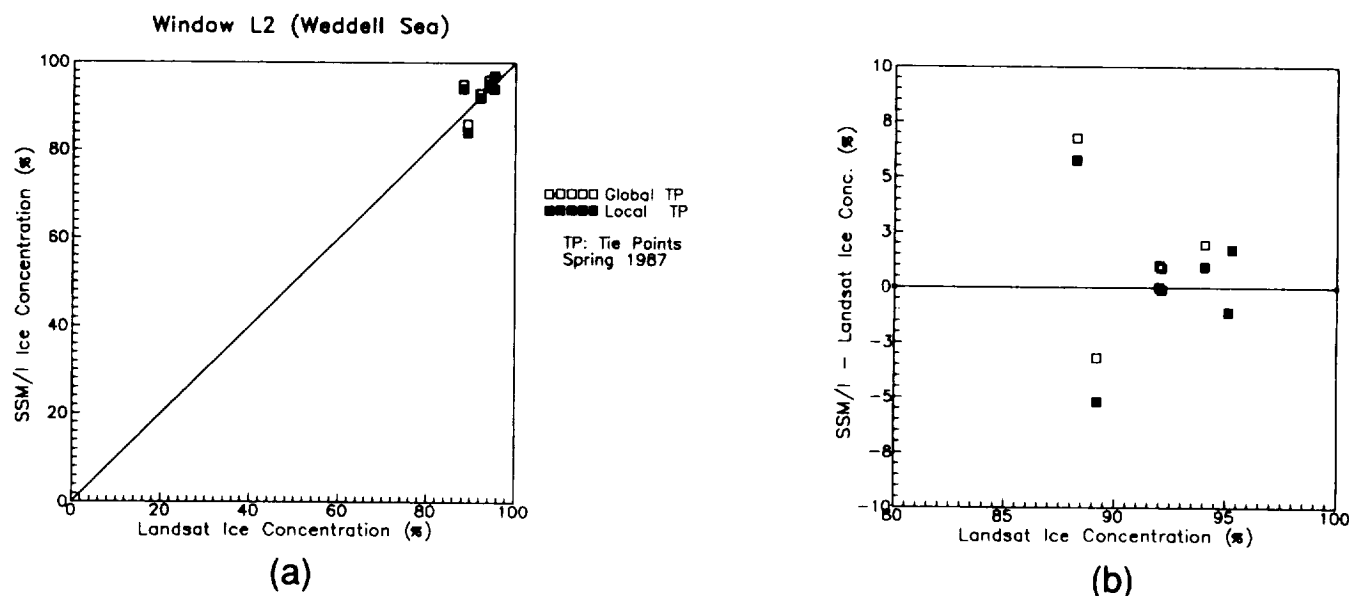


Figure 5.7. Comparison of ice concentration (50-km grid) between NASA Team algorithm using local and global tie-points versus Landsat values for the Weddell Sea spring and summer ice conditions (Window L2 - Nov. 29, 1987).

### 5.5.5 Amundsen Sea

The area of the second case study in the southern hemisphere is located in the Amundsen Sea. The mean difference between Landsat- and SSM/I-derived ice concentrations is 1.0% for local tie-points and 1.3% for global tie-points, respectively (Figure 5.8). Ice floes in the close pack may have been displaced because of wind and ocean currents within the 8 hours between the overpasses of the two satellites, which could account in part for some of the ice concentration difference between Landsat and SSM/I. At the present time, we have no means of compensating for ice displacements between the two satellite overpasses, and consequently we can only state that the NASA Team algorithm performs better than  $\pm 3.7\%$  standard deviations for both local and global tie-points.

The Weddell and Amundsen seas case studies are the only comparisons for the southern hemisphere, which is inadequate, considering the large seasonal change in the Antarctic sea ice cover. Additional case studies for the Weddell Sea, Ross Sea, and Bellingshausen Sea are needed to draw conclusions regarding the accuracy of the NASA Team algorithm for the entire Antarctic region.

#### Amundsen Sea, summer 1990

Statistics of SSM/I ice concentration minus Landsat ice concentration expressed as a percent for local and global tie-points (TPs). (# cases: number of 50- x 50-km grid cells used in the comparison)

	mean	median	sd	min	max	# cases
Local TP	1.0	1.1	3.7	-5.8	5.2	7
Global TP	1.3	1.1	3.6	-4.8	6.2	7

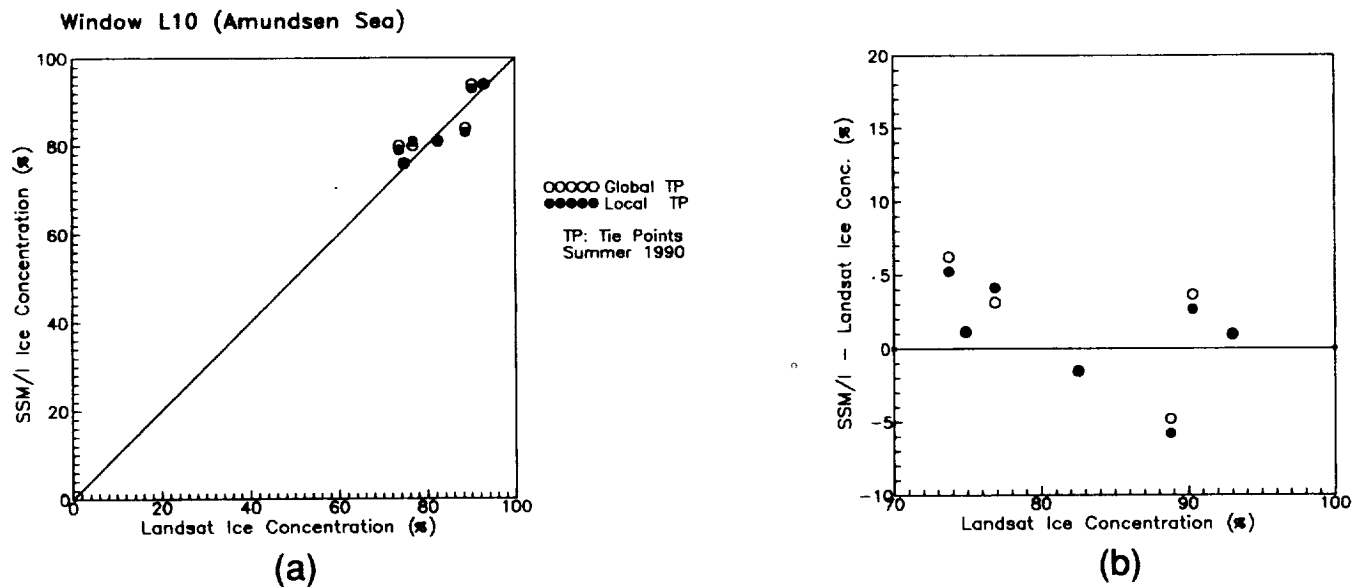


Figure 5.8. Comparison of ice concentration (50-km grid) between NASA Team algorithm using local and global tie-points versus Landsat values for the Amundsen Sea summer ice conditions (Window L10 - Dec. 29, 1990).

## 5.6 Conclusions

Several important conclusions can be drawn from this SSM/I validation. They are highlighted below.

Ice concentrations during fall can be derived from passive-microwave data with a mean difference of less than 0.2% (compared to Landsat ice concentrations) and a standard deviation of 3.1%, using the NASA Team algorithm with local tie-points. With global tie-points, a mean difference of 0.1% and a standard deviation of 6.2% was found. During winter, a comparable performance of the NASA Team algorithm is expected because of similar ice conditions.

In spring, the overall difference between the NASA Team algorithm and Landsat concentrations is more negative compared with fall, with a mean difference of about -2.4% and a standard deviation of about 4.8% for local tie-points. For global tie-points, the mean difference is -5.6% and the standard deviation is 5.9%. However, in areas with higher amounts of nilas and young ice, we found that the SSM/I ice-concentration algorithm underestimates ice concentration by as much as 9% with global tie-points and -4% with local tie-points with standard deviations of 6.4% and maximum differences between SSM/I and Landsat ice concentrations of over -20%. This was observed in two separate Landsat-SSM/I comparisons.

The ice concentration of pack ice in summer is affected by wind and currents, and, therefore, an accurate error estimate seems almost impossible in the absence of truly simultaneous coincident data. Differences between SSM/I and Landsat ice concentrations ranged between -24% and 46%. Part of this difference can be attributed to ice movement between the two satellite passes (6 hours) and part, to surface melt processes.

The performance of the NASA Team algorithm compared with Landsat derived values, for all case studies in spring and fall, gives a correlation of 0.968 using global tie-points (Figures 5.9 and 5.10). The NASA Team algorithm underestimates ice concentration in areas of close pack ice and overestimates ice concentration in areas of open pack ice. Using local tie-points for the same case studies, the correlation coefficient increases to 0.982, and the regression line shows the same characteristic as described for the global tie-points.

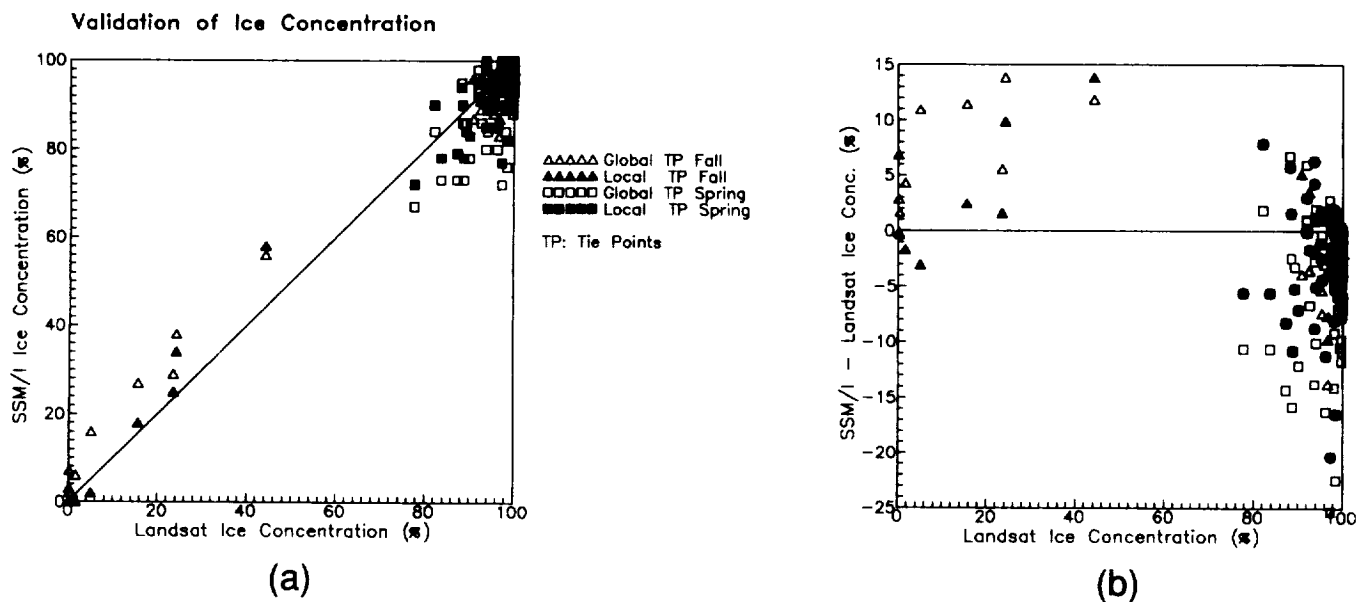


Figure 5.9. Comparison of ice concentration (50-km grid) between NASA Team algorithm using local and global tie-points versus Landsat values for the Beaufort, Chukchi, Weddell and Greenland seas, spring and fall ice conditions (excluding Windows L5 and L6).

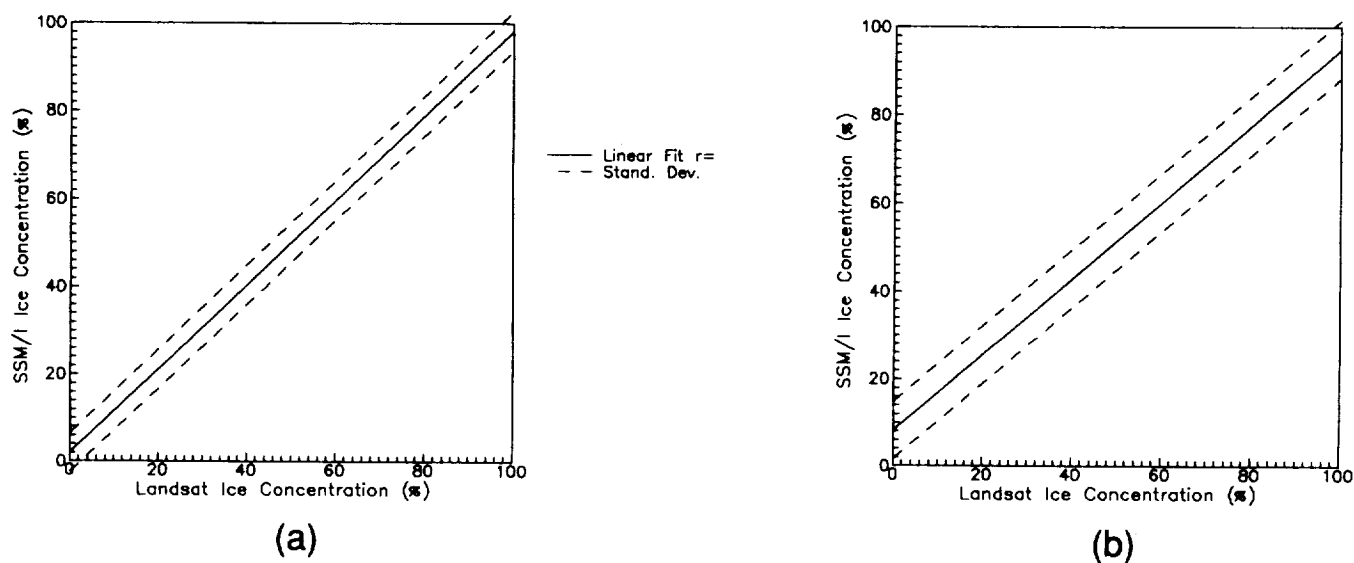


Figure 5.10. Linear regression lines for all case studies in spring and fall (Figure 5.8) for local (left) and global (right) tie-points. The correlation coefficients are 0.982 and 0.968 for local and global tie-points, respectively. The dashed lines depict one standard deviation:  $\pm 4.5\%$  for local and  $\pm 6.6\%$  for global tie-points, respectively.

Beaufort, Chukchi, Weddell, and Greenland seas, spring and fall conditions

Statistics of SSM/I ice concentration minus Landsat ice concentration expressed as a percent for local and global tie-points (TPs). (# cases: number of 50- x 50-km grid cells used in the comparison)

	mean	median	sd	min	max	# cases
Local TP	-1.5	0.0	4.5	-20.3	7.9	95
Global TP	-3.6	-3.2	6.6	-25.3	13.8	95

It appears that seasonal and regional adjusted tie-points (local tie-points) will improve the overall performance of the SSM/I sea ice concentration algorithms. Our work suggests that where the ice has a higher variation of internal characteristics (e.g., salinity), the global tie-points will cause a standard deviation of about 7% for spring and fall ice concentration. Use of local tie-points dropped the standard deviation to 5% for the same cases studied. In the southern hemisphere, where the ice cover is essentially 1 year in age, the global tie-points perform reasonably well.

The geolocation problem in SSM/I data does not greatly affect the 50-km gridded sea ice concentration accuracy when compared to Landsat-derived ice concentrations. Using the UMASS geolocation correction for the SSM/I data, the Landsat-SSM/I comparison improved by 2% to 3%. This is encouraging, because it means that the sea ice concentration grids may not be as sensitive to the geolocation error as previously thought.

## 5.7 References

- Cavalieri, D. J., P. Gloersen, and W. J. Campbell, Determination of sea ice parameters with Nimbus 7 SMMR, *J. Geophys. Res.*, 89, pp. 5355-5369, 1984.
- Comiso, J. C., and H. J. Zwally, Antarctic sea ice concentrations inferred from Nimbus 5 ESMR and Landsat Imagery, *J. Geophys. Res.*, 87(C8), pp. 5836-5844, 1982.
- Comiso, J. C., Sea ice effective microwave emissivities from satellite passive microwave and infrared observations, *J. Geophys. Res.*, 88(C12), pp. 7686-7704, 1983.
- Comiso, J. C., Characteristics of arctic winter sea ice from satellite multispectral microwave observations, *J. Geophys. Res.*, 91(C1), pp. 975-994, 1986.
- Gloersen, P., and D. J. Cavalieri, Reduction of weather effects in the calculation of sea ice concentration from microwave radiances, *J. Geophys. Res.*, 91(C3), 3913-3919, 1986.
- Miller, J. M., and G. J. Burger, Enhancing Landsat data acquired under very low illumination, *Photogrammetric Engineering and Remote Sensing*, Vol. 52, No.6, June 1986, pp. 801-807, 1986.
- Steffen, K., Atlas of sea ice types, deformation processes and openings in the ice, *Zurcher Geographische Schriften*, No. 20, Swiss Federal Institute of Technology, Zurich, Switzerland, p. 55, 1986.
- Steffen, K., and J. A. Maslanik, Comparison of Nimbus 7 Scanning Multichannel Microwave Radiometer radiance derived from ice concentrations with Landsat imagery for the North Water area of Baffin Bay, *J. Geophys. Res.*, 93(C9), 10769-10781, 1988.
- Steffen, K., and A. Schweiger, A multisensor approach to sea ice classification for the validation of DMSP-SSM/I passive microwave derived sea ice products, *Photogrammetric Engineering and Remote Sensing*, 56(1), 75-82, 1990.
- Svendsen, E., K. Kloster, B. Farrelly, O. M. Johannessen, H. A. Johannessen, W. J. Campbell, P. Gloersen, D. J. Cavalieri, and C. Matzler, Norwegian remote sensing experiment: Evaluation of the Nimbus-7 scanning multichannel microwave radiometer for sea ice research, *J. Geophys. Res.*, 88(C5), 2781-2791, 1983.

## Chapter 6

### SSM/I-AVHRR COMPARISON

William J. Emery and Charles W. Fowler  
Colorado Center for Astrodynamics Research  
University of Colorado  
Boulder, Colorado 80309

6.1 Introduction .....	47
6.2 AVHRR and SSM/I Imagery .....	47
6.3 Ice-Concentration Methods .....	48
6.4 Sample Images .....	49
6.5 Statistical Comparisons and Conclusions .....	51
6.6 References .....	53

#### 6.1 Introduction

The goal of the ice-concentration comparisons presented here was to evaluate the measurement of sea ice concentration by the SSM/I as compared to coincident Advanced Very High Resolution Radiometer (AVHRR) imagery for a variety of seasons and locations. The relative ease of acquiring AVHRR imagery, as compared with Landsat data, makes it attractive to compare SSM/I- and AVHRR-derived ice concentrations for a range of locations and seasons. Both near-infrared (channel-2) and thermal infrared (channel-4) AVHRR images were used to compute ice concentrations. In many cases (night or winter imagery), only the thermal infrared AVHRR channel data were available for the computation of ice concentration.

While a great many AVHRR images were acquired for this study, the generally large amount of cloud cover eliminated many of the images for use in the comparisons. This is a common problem, particularly in high latitude regions where persistent cloud cover severely restricts the use of visible and infrared satellite imagery for the study of ice parameters. In spite of these problems, a total of about 12 very good AVHRR images were selected from the following Arctic regions: Beaufort Sea, Davis Strait/Baffin Bay, and Greenland Sea. Images were used from each of the four seasons over 2 years (1987-88), providing comparisons for a wide range of sea ice conditions.

One concern in using AVHRR imagery to evaluate the performance of the SSM/I imagery is the fact that sea ice parameters, computed from AVHRR imagery, have not been validated. As a consequence, we carried out a separate study (Emery et al., 1991) to assess the validity of sea ice parameters computed from AVHRR data. For this assessment, we used AVHRR imagery from the Bering Sea, which was coincident with Landsat imagery used by Steffen and Schweiger (1991), for an independent validation of the SSM/I. In addition, the Bering Sea AVHRR image was coincident with an aircraft survey (Cavalieri, 1988) that collected microwave data for the computation of sea ice concentration.

This comparison with Landsat and microwave aircraft data (Emery et al., 1991) suggested that ice concentrations, computed from AVHRR near-infrared (channel-2) images are accurate to 17%-18%, while ice concentrations computed from thermal infrared (channel-4) AVHRR imagery are accurate to 19%-27%. Thus, a comparison between the AVHRR and SSM/I ice concentrations should yield valuable information, since these comparisons can be carried out for a variety of regions and seasons unlike the Landsat and aircraft validations, which were limited in location and seasonal coverage.

#### 6.2 AVHRR and SSM/I Imagery

The AVHRR data all had a 1-km spatial resolution and were primarily collected at various direct readout sites. The receiving station at Edmonton, Alberta, Canada, operated by the Canadian Atmospheric Environment Service (AES), collected AVHRR data from the Beaufort Sea and the Davis Strait areas. Other Beaufort Sea images were

acquired from a receiving station operated by the University of British Columbia in Vancouver, B.C. Data for the Greenland Sea came from the antenna operated by the University of Dundee in Dundee, Scotland.

All of the AVHRR images were navigated to within  $\pm 1$  km using software described in Emery et al., 1989. In every case, the image was checked by visual inspection of the land marks in the image to ensure the accuracy of the image navigation at these high polar latitudes. Frequently, navigation packages have problems at higher latitudes where the satellite pass switches from ascending to descending. Here, timing errors in the time of data collection must be accounted for in correcting the image for comparison with other independent satellite data. This is a critical requirement for any type of validation comparison study.

In each AVHRR image, land surfaces were masked out to eliminate them from consideration in the computation of ice concentration. Clouds were subjectively identified by inspection of the individual image. A very conservative position was taken in this cloud removal, and any feature suspected of being a cloud was removed from consideration. Experience with a great number of polar AVHRR imagery was involved in this cloud-removal procedure.

All of the SSM/I imagery were taken from the CD-ROM disks distributed by the National Snow and Ice Data Center (NSIDC) (see Chapter 3). All of these data were corrected for geolocation errors prior to gridding (see Chapters 2 and 3); the methods for computing sea ice concentration from the SSM/I data have been discussed in Chapter 4.

While over 20 AVHRR images were analyzed for this study, we will present the statistics from the 12 best images. We believe that these 12 images represent a good cross section of all the conditions that we examined, and the resulting statistics should provide the best evaluation possible with a comparison between AVHRR and SSM/I data. The data are from both 1987 and 1988, but together they cover a series of seasons including winter (2 channel-4 images), spring (2 channel-2 and 4 channel-4 images), summer (2 channel-2 and 1 channel-4 images), and fall (1 channel-4 images). The images are all listed in Table 6.1, along with the comparison statistics between the AVHRR and SSM/I ice concentrations.

Table 6.1. Ice Concentration Comparison Statistics

Location	Date	Channel	# Cells	Threshold Method		Tie-Point Method		Modified Tie-Point Method	
				Mean Diff	Std Dev	Mean Dif	Std Dev	Mean Diff	Std Dev
Davis Strait	880325	4	1090	-10.7	11.7	33.4	14.1	2.5	15.5
Davis Strait	880402	4	729	-11.1	6.2	19.7	13.4	-5.0	11.2
Beaufort Sea	871029	4	1594	-36.1	31.1	-1.5	15.9	-1.5	15.9
Beaufort Sea	871111	4	1860	-7.7	8.1	20.1	13.6	-2.3	6.6
Beaufort Sea	880121	4	1275	-1.1	2.3	25.9	8.8	-1.1	2.3
Beaufort Sea	880325	2	1372	-2.4	7.7	39.2	26.6	-2.4	7.7
Beaufort Sea	880325	4	1372	-3.9	3.2	15.3	10.4	-3.9	3.2
Beaufort Sea	880402	2	1932	-5.1	3.8	22.9	23.2	-5.3	3.8
Beaufort Sea	880402	4	1932	-5.4	3.9	8.4	7.8	-5.4	3.9
Greenland Sea	870725	2	619	-44.7	32.6	-1.1	17.2	-1.1	17.2
Greenland Sea	870825	2	2079	-39.2	29.8	2.8	17.7	-2.0	20.3
Greenland Sea	870825	4	2079	-71.8	17.3	-18.2	15.8	-6.5	13.6

### 6.3 Ice-Concentration Methods

A variety of ice-concentration methods was used in this study to determine which yielded the most favorable comparisons between the AVHRR and SSM/I data. Initially, only the "threshold" technique (Hall, 1980) was used, but

problems during the transition seasons necessitated developing "tie-point" methods (Comiso and Zwally, 1982) as well. For the AVHRR images, both the threshold and tie-point values were subjectively selected by examining the image. In AVHRR images, selection of either open water or white ice is fairly easy. Problems arise, however, in locating new or thin ice with its gray, rather than white, appearance. Nilas and some gray ice types appear as open water in the AVHRR imagery. The clue to selecting the open water value for the AVHRR is to find a brightness value that appears to be in open water and is consistent over a relatively large area. Thus, the open water value is usually constant to within 1 brightness value in the 10-bit AVHRR brightness count.

In addition to the threshold and tie-point methods, a combination technique (called the modified tie-point method) was also employed. Threshold values for open water and gray ice were selected. Ice values above the gray ice threshold were classified as ice, and water values below the open water threshold were classified as water. It was found that the results (Table 6.1) improved markedly with the introduction of this hybrid ice concentration technique. The gray ice tie-point value, in terms of infrared surface temperature, corresponds to 0.4-m ice thickness for winter-spring (Maykut, 1978).

A similar approach with Landsat imagery would not work well at all (priv. comm. Koni Steffen). The success of this technique as applied to AVHRR imagery can be attributed partly to the lower spatial resolution of the AVHRR as compared to Landsat imagery. This leads to the possibility that a 1-km pixel could be only partially filled with ice, but with the threshold-only method, the same pixel would qualify for zero ice concentration. By adding the mid-range tie-point technique, there was an opportunity to map the partial concentrations that occurred under such conditions. We also found that the modified tie-point method worked much better with the channel-4 thermal infrared imagery, which were not available for the Landsat data. Thus it may be that this technique must be introduced when using thermal infrared imagery.

SSM/I ice concentrations were computed using local tie-points as motivated by Steffen and Schweiger (1991) who found that local tie-points performed better than the hemispheric values. The local tie-points were determined by looking at the 19V, 19H, and 37V SSM/I images. By inspection, areas of open water, first-year ice, and multiyear ice were selected, and the tie-point values were set by viewing these same conditions over the entire image.

For all methods, a bin size of 25 km was used for the AVHRR data to be consistent with the resolution of the SSM/I grid. The AVHRR ice concentrations were computed for each 1- x 1-km pixel and then averaged over the 25-km<sup>2</sup> bins. During the times of the AVHRR coverage, it was often necessary to bin SSM/I data over 12- to 24-hour periods. This was caused by the presence of bad SSM/I data in many of the orbits that were nearly coincident with the AVHRR imagery. We therefore chose to simply use the 24-hour SSM/I data provided by NSIDC on their CD-ROMs. While this compositing can affect the ice concentrations significantly, because of strong wind-driven ice motions, we had to assume that the ice concentrations would stay fairly constant over the 12- to 24-hour periods used to composite the SSM/I ice concentrations. In regions such as the western Greenland Sea and Davis Strait, where considerable ice motion can be expected, this assumption is not valid. The resulting noncoincidence of the AVHRR and SSM/I satellite imagery will lead to differences in ice concentrations for these regions where the ice can be moving fairly rapidly. This is an important point to remember when examining the results of the statistical comparisons.

#### 6.4 Sample Images

In this section, we present an example of the AVHRR and SSM/I images that we compared in this study. This example is intended to illustrate the basic character of these two different types of satellite data, and they are not intended to display all of the different detailed differences and similarities that were found between these image types. The channel-2 AVHRR image in Figure 6.1 was collected on August 25, 1987, over the Greenland Sea region. A land mask has been added (broad white lines) on the western side of the image. Latitude and longitudes have been displayed as dotted lines for every degree. The ice appears as gray to white features with a considerable amount of broken and smaller ice floes being present. The edge of the ice can be clearly seen on the eastern side of the image with small tongues protruding eastward into the darker open water.

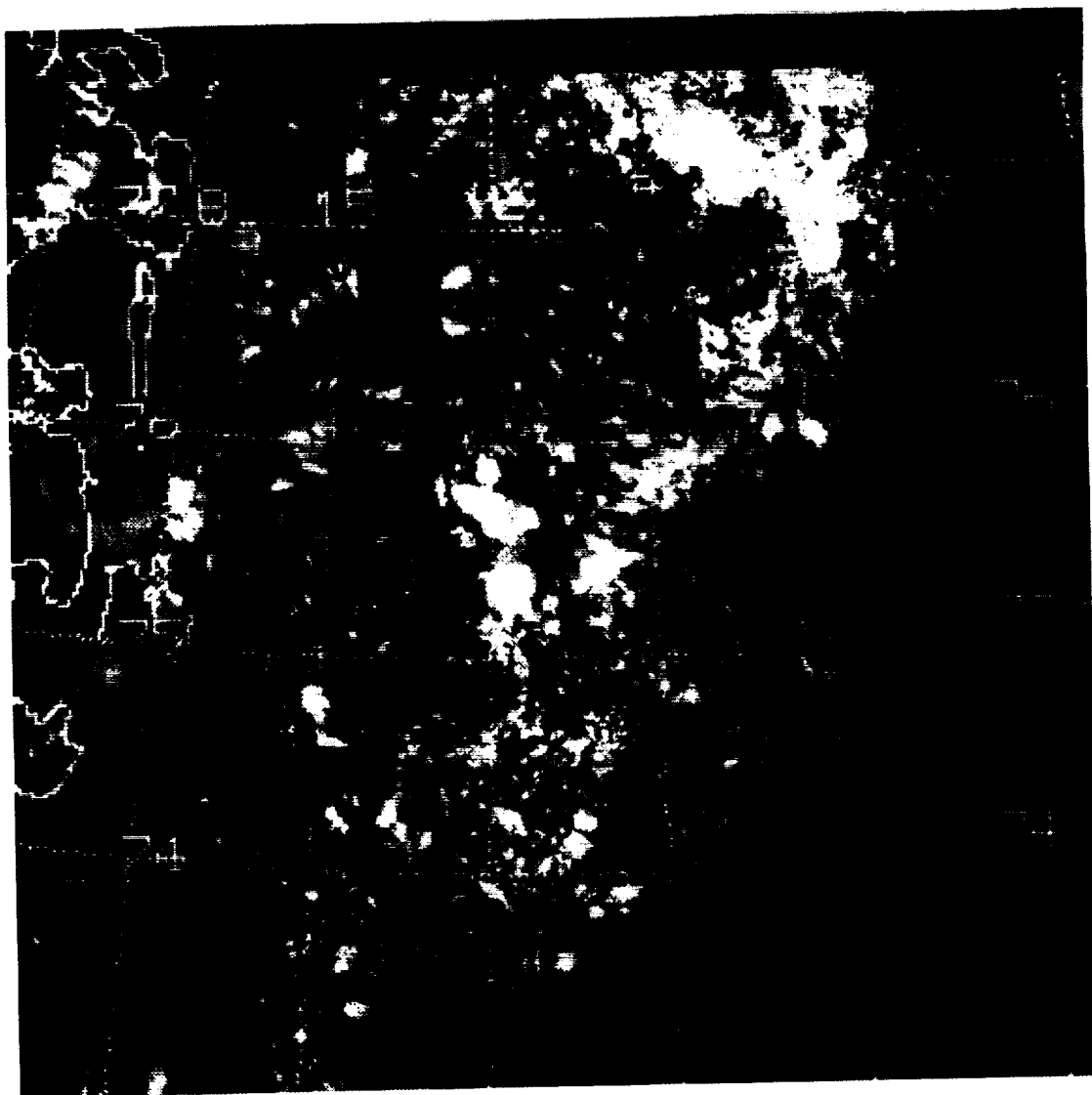


Figure 6.1. AVHRR channel-2 image of the western Greenland Sea on August 25, 1987.

The ice concentrations, computed from this AVHRR image, are shown in Figure 6.2. Here the black colors are regions that have been masked for land and clouds, white indicates 100% ice concentration, while 0% is shown by the dark gray shades (note the open water at the lower right-hand corner). Gray shades in between represent the intermediate ice concentrations. The individual boxes are the 25 km<sup>2</sup> bins that have been used to average the AVHRR ice-concentration values. The corresponding SSM/I ice concentrations are shown here in Figure 6.3. The concentration gradients appear much smoother because of the lower resolution of the SSM/I instrument. The land and cloud mask in Figure 6.2 is not included in this image but was used to select the SSM/I pixels for comparison with the AVHRR concentrations.

There is a broad general agreement in the ice concentrations of Figures 6.2 and 6.3 with higher concentrations in the northeast and lower concentrations in the southwest. Open water occupies the eastern boundary with a larger region in the southeast corner. Ice-concentration differences are most obvious in the lower concentration (gray) areas in the western half of the images. Here there are isolated AVHRR boxes with high concentrations, while the SSM/I shows a consistently lower concentration level.

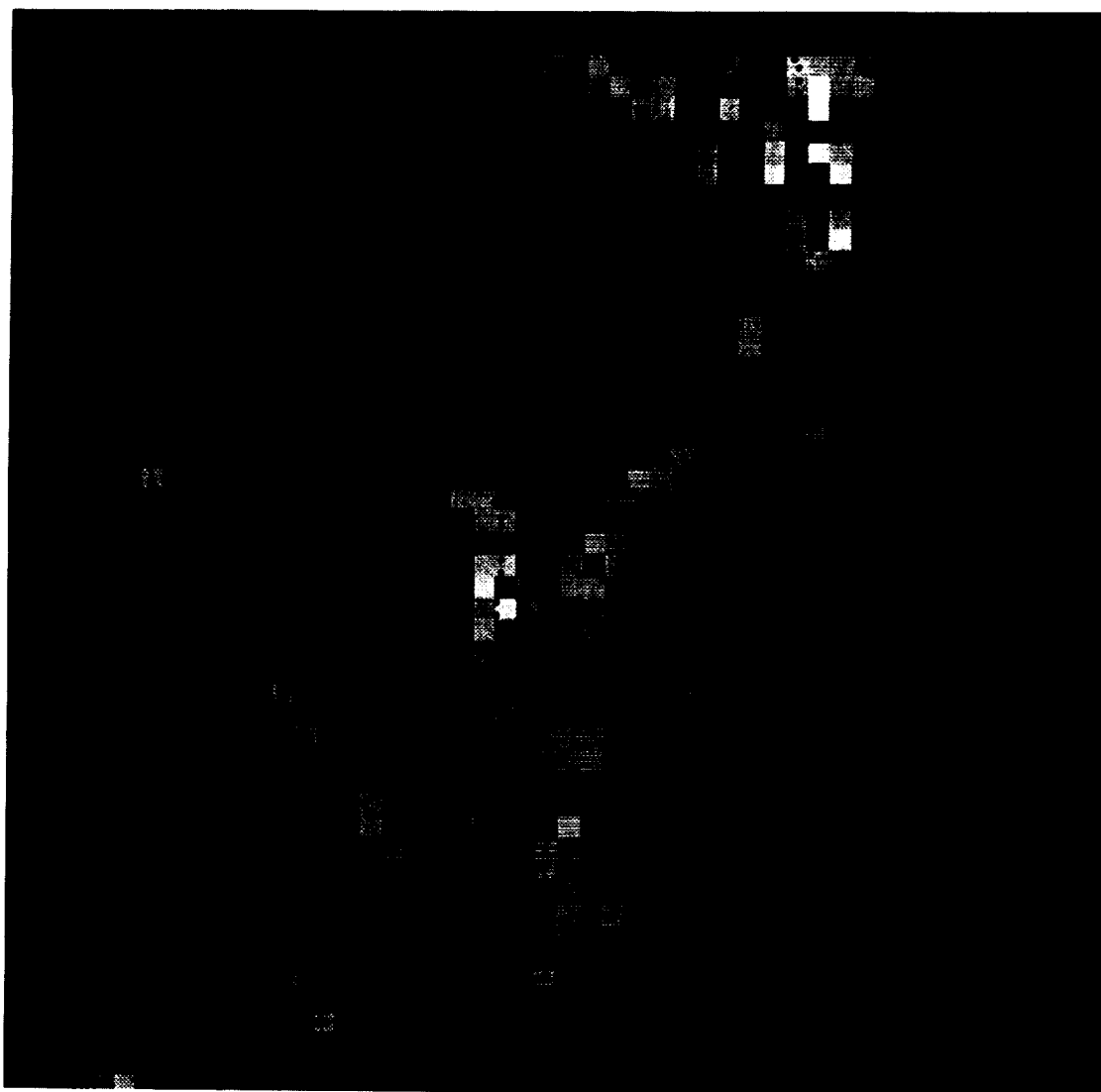


Figure 6.2. Ice concentration computed from the AVHRR channel-2 image in Figure 6.1. Black shades denote land- and cloud-masked portions of the image; white shades are 100% ice concentration, while 0% ice is shown by the dark grey shades (note open water in the lower right-hand corner).

## 6.5 Statistical Comparisons and Conclusions

All of the statistical comparison results are presented in Table 6.1. The geographic location of the image is in the first column, while the second column indicates the date as year, month, and day. The channel designation is given as either 2 for the near-infrared or 4 for the thermal infrared. The number of cells used per image is given in the next column. The mean difference, computed as the mean difference between the SSM/I and the AVHRR ice concentrations (SSM/I-AVHRR) for the  $625 \text{ km}^2$  bins and then averaged over the entire image, and the standard deviation are given for each of the three methods. Note that there are many channel-4 images without matching channel-2 data. These are caused by the AVHRR data being collected at night or during winter when no visible light is available at the near-infrared wavelengths of channel-2.

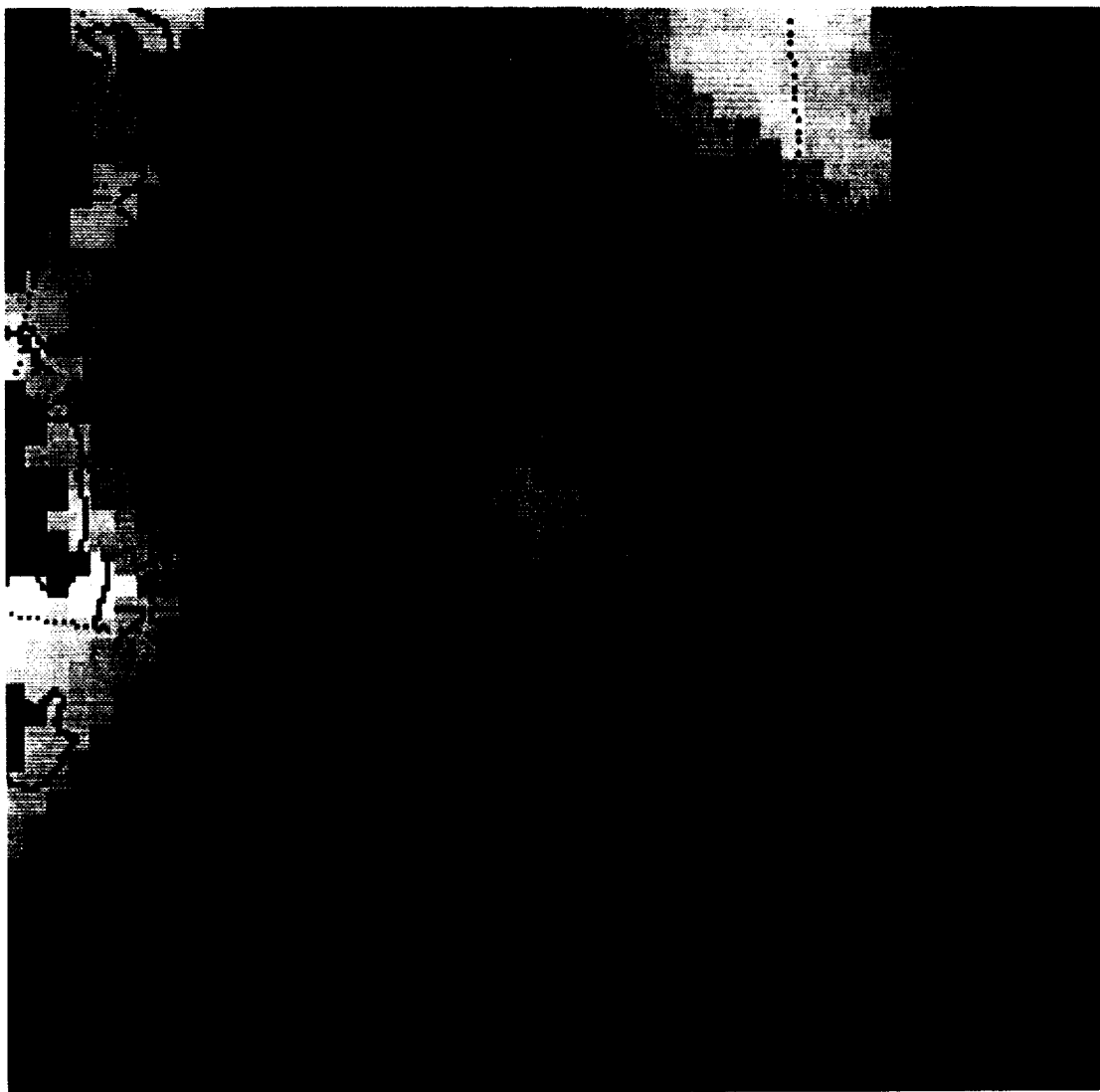


Figure 6.3. Ice concentration computed from the coincident 24-hour SSM/I composite image. Again, high concentration is white; while dark grey corresponds to 0% ice concentration.

All images were approximately the same size (512 x 512 portions of the larger AVHRR images), and the variations in the number of cells compared indicates the continued need for filtering clouds out of the AVHRR imagery. If there had been no clouds present, each image would have had approximately the same number of cells compared each time. In all cases, however, there are enough sample values that all of the statistics are significant at the 99% level. This is an inherent advantage of working with the AVHRR in that it provides a temporally regular sample at a moderately high spatial resolution.

In both the threshold and combined methods, the overall mean differences were generally negative (SSM/I minus AVHRR), indicating that for these methods, the AVHRR yield a typically greater ice concentration than does the SSM/I. The mean differences are considerably smaller for the combined method than for either the threshold or tie-point-only methods. The tie-point method reverses this trend, particularly in winter and early spring, with large positive values indicating that AVHRR ice concentrations are smaller than the SSM/I ice concentrations. During this time of year, the tie-point method is not expected to do as well as the threshold technique for computing the sea ice concentrations.

The standard deviations in Table 6.1 are a measure of the variability of the ice concentration differences. In most cases, the standard deviations are less than 10%. In general, the standard deviations are lower for the combined method, while the largest values occurred with the threshold method in summer and fall. All of the ice-concentration methods had larger standard deviations in the summer images that were all from the Greenland Sea. Unfortunately, it was not possible to have a complete seasonal sample from each of the regions, which makes it difficult to separate seasonal dependence from regional variability.

The smallest standard deviations were for the combined method in winter and spring for the Beaufort Sea. Here the values are all less than 10% with an average standard deviation for 6 images of 4.7%. This same set of results also has the smallest mean difference with a value of -3.4%. At this point, it is not clear if these values are representative of the overall differences between AVHRR- and SSM/I-derived ice concentrations. Only the study of a great many more images from other areas and seasons will be able to resolve the representative character of these results.

## 6.6 References

- Cavalieri, D. J., *NASA Sea Ice and Snow Validation Program for the DMSP SSM/I: NASA DC-8 Flight Report*, NASA Technical Memorandum 100706, 143 pages, September 1988.
- Comiso, J. C., and H. J. Zwally, Antarctic sea ice concentrations inferred from Nimbus 5 ESMR and Landsat imagery, *J. Geophys. Res.*, 87, 5836-5844, 1982.
- Emery, W. J., J. Brown, and Z. P. Novak, AVHRR image navigation: summary and review, *Photo gram. Eng. Rem. Sens.*, 55, 1175-1183, 1989.
- Emery, W. J., M. Radebaugh, C. W. Fowler, D. Cavalieri, and K. Steffen, A comparison of sea ice parameters computed from Advanced Very High Resolution Radiometer and Landsat Satellite imagery and from airborne passive microwave radiometry, *J. Geophys. Res.*, 96, 22075-22086, 1991.
- Hall, R. T., "AIDJEX modelling group studies involving remote sensing data" in: Pritchard, R.S., ed., *Sea Ice Processes and Models*, University of Washington Press, Seattle, 151-162, 1980.
- Maykut, G. A., Energy exchange over young sea ice in the central Arctic, *J. Geophys. Res.*, 83, 3646-3658, 1978.
- Steffen, K., and A. J. Schweiger, NASA team algorithm for sea ice concentration retrieval from Defense Meteorological Satellite Program Special Sensor Microwave Imager: comparison with Landsat satellite imagery, *J. Geophys. Res.*, 96, 21971-21987, 1991.



## Chapter 7

### SSM/I AIRCRAFT UNDERFLIGHTS: INTRODUCTION AND AIRCRAFT SENSOR COMPARISONS

Donald J. Cavalieri

Laboratory for Hydrospheric Processes  
NASA Goddard Space Flight Center  
Greenbelt, Maryland 20771

John P. Crawford and Mark R. Drinkwater

Jet Propulsion Laboratory  
California Institute of Technology  
Pasadena, California 91109

Duane T. Eppler and L. Dennis Farmer

Naval Oceanographic and Atmospheric Research Laboratory  
Hanover, New Hampshire 03755

7.1 Introduction .....	55
7.2 Aircraft Instrumentation .....	56
7.3 Aircraft Data Sets .....	57
7.4 Discussion of Results .....	58
7.5 Conclusions .....	66
7.6 References .....	67

#### 7.1 Introduction

In March 1988, the NASA DC-8 Airborne Laboratory and two Navy P-3 research aircraft made a series of SSM/I underflights to provide data needed to complete the objectives of NASA's Sea Ice Validation Program for the SSM/I (Cavalieri, 1988). While the Landsat analysis provides the best available measure of total ice concentration for comparison with the SSM/I in different regions and for different seasons, no satellite data currently available can provide an accurate measure of multiyear (MY) ice concentration with which to validate the SSM/I product. The only available source of MY ice concentration data for SSM/I validation is from high-resolution airborne microwave sensors. A major goal of these underflights then was to acquire the requisite microwave imagery to validate the MY ice concentrations in different regions of the Arctic.

A key factor in the successful completion of the underflight mission was having access to near real-time SSM/I data during the flight planning sessions. In support of the NASA mission, Capt. Otto Steffin, Chief of NOAA's Ocean Applications Group in Monterey, California, made available near real-time SSM/I data during the underflight period, and Dr. Per Gloersen of the Laboratory for Hydrospheric Processes at the NASA Goddard Space Flight Center (GSFC) in Greenbelt, Maryland, successfully routed these data to the Laboratory computing faculty at Goddard via high-speed data links. Once the data were acquired at Goddard, the radiances were processed with the NASA SSM/I sea ice algorithm and computer-character ice concentration maps were generated. These maps were then transmitted to our flight operations center in Fairbanks, Alaska. The SSM/I data acquisition in Monterey, transmission and processing at Goddard, and receipt of the sea ice concentration maps in Fairbanks all occurred within 12 hours.

A total of fifteen flights were made with both NASA and Navy aircraft covering portions of the Bering, Beaufort, and Chukchi seas. A summary of the flights made by the three aircraft including date, aircraft, region flown, flight objective and satellite coverage is given in Table 7.1. Although most of the flights were at night to obtain coincident observations with the SSM/I, some of the flights were made during daylight, coincident with NOAA-9 and -10 and

Landsat-4 and -5 overpasses. Under clear atmospheric conditions, NOAA AVHRR and Landsat MSS sensors provided visible and infrared sea ice imagery at spatial resolutions of 1 km and 80 m, respectively.

Table 7.1. NASA and Navy Aircraft Flight Summary

DATE	AIRCRAFT	REGION/PATTERN	OBJECTIVE
Mar 8	NRL P-3	Cape Lisburne/Mosaic	UnderflySSM/I; thin & thick FY ice; MY/FY transition.
Mar 11	NASA DC-8 NRL P-3	Beaufort Sea/Transect	Ice camp; sharp MY/FY trans.; MY ice-edge definitions & MY ice variability.
Mar 13*	NASA DC-8 NRL P-3	Bering Sea /Mosaic	Ice-edge definition; new ice formation; total ice-concentration variability.
Mar 14	NASA DC-8 NRL P-3	Chukchi Sea/Mosaic	FY ice-signature variability; FY/MY transition.
Mar 17	NASA DC-8	Prudhoe/Harrison Bay/Transect	Locate & verify MY variability observed in SSM/I sea ice imagery.
Mar 18	NASA DC-8 NADC P-3	Beaufort Sea/Mosaic	Underfly SSM/I; overfly ice camp
Mar 19*	NASA DC-8 NADC P-3	Beaufort Sea/Mosaic	UnderflySSM/I; variability of FY/MY ice concentration.
Mar 21*	NASA DC-8 NADC P-3	Bering Sea/Mosaic	Underfly SSM/I; definition of ice edge; effectiveness of weather filter; ice-concentration variability.
Mar 22	NADC P-3	Chukchi Sea/Transect	Ice-type variability

\*Landsat coverage

Landsat coverage also for 3/12 and 3/16

## 7.2 Aircraft Instrumentation

The NASA DC-8 aircraft was equipped with both active- and passive-microwave sensors. The complement of fixed-beam, dual-polarized radiometers supplied by the GSFC has frequencies and polarizations closely matching those of the SSM/I. The active sensors supplied by the Jet Propulsion Laboratory (JPL) of the California Institute of Technology included fully polarimetric C-, L-, and P-band synthetic aperture radars (SAR). The operating characteristics of these microwave sensors are summarized in Table 7.2. In addition to these microwave sensors, other sensors on the DC-8 were flown in a support capacity (Cavalieri, 1988).

The NASA DC-8 flights were coordinated with two Navy research aircraft also supporting NASA's validation program. An NRL P-3 provided high-resolution (100-m), passive-microwave imagery with the NOARL Ka-band Radiometer Mapping System (KRMS) operating at 33.6 GHz (vertical polarization). The KRMS, which can discriminate among open water, old ice, and a range of first-year (FY) ice types, provides the basis for interpreting the AMMR profiles and SAR images. Each of the three surfaces of interest in this validation effort, open water, FY ice, and MY ice have unique radiometric signatures at the KRMS frequency and can be discriminated unambiguously in KRMS' images (Eppler et al., 1986). This, coupled with KRMS good spatial resolution and wide swath, make the sensor ideal for validating the SSM/I total and MY ice concentration variations.

The NADC P-3 provided wide-swath, high-resolution SAR coverage at C- and X-bands. A description of the operating characteristics of both the NORDA KRMS and the NADC SAR are summarized in Chapters 8 and 9, respectively.

Table 7.2. NASA DC-8 Microwave Sensors

PASSIVE MICROWAVE				
GSFC Aircraft Multichannel Microwave Radiometer (AMMR)				
Freq (GHz)	Polarization	Beam Width (degrees)	Resolution	Look Angle (degrees)
18.0	H & V	6	1/7 alt.	45 L
21.0	V only	6	1/7 alt.	45 L
37.0	H & V	6	1/7 alt.	45 L
92.0	H & V	6	1/7 alt.	45 L
21.0	—	—	—	skyward
37.0	—	—	—	skyward
ACTIVE MICROWAVE				
JPL Synthetic Aperture Radar (SAR): Left side imaging (30° - 70°)				
Band	Wavelength	Polarization	Resolution(Azim/Slant)	
P	67 cm	H & V alt. trans.	10.7/7.5 m	
		H & V simult. rec.	10.7/7.5 m	
L	24 cm	H & V simult. rec.	10.7/7.5 m	
C	5.6 cm	H & V simult. rec.	10.7/7.5 m	

### 7.3 Aircraft Data Sets

The flights provided two basic types of aircraft data sets for validating the sea ice algorithm. The first type resulted from flight patterns that produced parallel swaths of imagery. These parallel swaths were used to form a mosaic image covering several pixels on the SSM/I grid. Ice concentrations derived from these aircraft mosaics provide a direct check on the accuracy of the SSM/I-derived sea ice concentrations. Both the NRL and NADC aircraft flew mosaic patterns measuring approximately 100 km by 200 km in area. The relatively narrow swath width of the JPL SAR made it impractical to produce mosaics with the DC-8. Data from three of the four KRMS flights (Beaufort transect on March 11, Bering mosaic on March 13, and the Chukchi mosaic on March 14) were acquired in conjunction with the NASA-JPL aircraft. Coincident coverage by KRMS, SAR, and AMMR exist for significant sections of these image sets. Additionally, a short section of the Beaufort transect was imaged by the NADC/ERIM SAR 8 days following acquisition of KRMS, AMMR, and JPL SAR data (Figure 7.1). The pack was stable over this period, and the same floes can be identified in KRMS, JPL SAR, and ERIM SAR images. The mosaic flights with the NRL P-3 on March 8 in the vicinity of Cape Lisburne and on March 14 in the northern Chukchi Sea and with the NRL P-3 on March 18 and 19 in the Beaufort Sea are discussed in the next two chapters.

The second type of aircraft data set, discussed in this chapter, is provided by the transect flights. These flights are particularly useful for determining which SSM/I ice concentration contour corresponds best to the ice-edge position as determined from aircraft observations and for assessing variations in MY ice concentration across large portions of the Arctic. The NASA DC-8 with its long range (nominally 3000 nm) and with the coincident measurements made by the JPL SAR and the GSFC AMMR make it ideal for validating the large-scale ice type variations observed in the SSM/I imagery. These flights were unique in that for the first time, SAR and AMMR overlapping data sets were obtained concurrently from the same platform.

## 7.4 Discussion of Results

### 7.4.1 Multiyear Ice Variability

The first transect flight occurred on March 11 from the coast of Alaska to a point north of Ellesmere Island (see Figure 7.1). The outgoing flight line is illustrated on the SSM/I map of MY ice concentration shown in Color Plate 3. An intercomparison of coincident KRMS, SAR cross-polarized C-, L-, and P-band, and AMMR data is presented in Figure 7.2 from a portion of the March 11 flight. Dark areas in both the KRMS and C-band SAR imagery correspond to FY ice; whereas, light areas correspond to MY ice types. A comparison of the KRMS and JPL SAR imagery demonstrates that C-band data provide good discrimination between MY and FY ice types, while the longer wavelength P- and L-bands highlight ridges and structural features, but not ice types.

The AMMR 18-GHz, H-pol. brightness temperature (TB) shown at the bottom of Figure 7.2 delineates the transition from FY ice off the Alaskan coast to MY ice in the central Arctic. A comparison of the AMMR data in Figure 7.2 with the coincident SSM/I MY ice-concentration map (Plate 3) shows that the FY, mixed, and MY ice regions in the AMMR data are coincident with similar regions in the SSM/I data. Arrows on the MY ice image in Plate 3 indicate the position of the transitions as determined from the AMMR data. Although the SSM/I image shown in Plate 3 has not been corrected for geolocation errors and may be in error by a pixel or two, the arrows on the image do correspond to gradients in the MY ice concentration. While the KRMS and SAR imagery shown in Figure 7.2 correspond to only a small portion of the AMMR trace (approximately 2 minutes of DC-8 flight time), they serve to establish the validity of the transition region as one of mixed ice types.

An examination of Plate 3 also indicates that the SSM/I MY ice concentration maps provide good definition of the position of the edge of the MY ice pack if the 30% ice-concentration contour is used as the indicator. There is, however, low-level (<20%) MY ice concentration over FY ice areas off the Alaskan coast and in the Bering Sea. This problem is addressed later.

Representative images acquired with KRMS along the March 11 flight track are shown in Figure 7.3. The first image (A) is at the beginning of the track near the Alaskan coast; the last (J) is at the end, approximately 40 km from the coast of Ellesmere Island. The intervening images (B through I) show ice at equally spaced intervals (approximately 200 km) along the flight track. Ice conditions shown represent at least four distinct zones: a) FY ice along the Alaskan coast (Figure 7.3, A and B), b) the transition zone from FY ice to the MY pack (Figure 7.3, C through E), c) MY pack ice (Figure 7.3, F and G), and d) the region of highly deformed ice adjacent to Ellesmere Island and the northern Canadian archipelago (Figure 7.3, H through J). A small number of scenes show open water and new ice in active leads, but exposed water generally is a minor constituent of the pack along the entire flight track.

A comparison of TBs measured along the entire track (Figure 7.1) with KRMS (33.6 GHz V-pol.) and NASA's AMMR (37 GHz V-pol.) is presented in Figure 7.4. KRMS TBs were derived by computing the mean radiance for consecutive 12-scanline segments along the track, and then using methods described by Farmer et al. (1990) to convert the mean radiances to TBs. High radiometric temperatures such as those at the left of each profile indicate FY ice; lower temperatures such as those towards the right of the profiles indicate MY ice. The location of images in Figure 7.3 is shown as dots below on the KRMS profile for reference.

Both sensors show patterns of variation similar to the 18-GHz AMMR trace in Figure 7.2. The plateau of generally uniform TBs at the left of the profile corresponds to FY ice near the Alaskan coast. Following this comes a zone of alternating high and low TBs that marks the transition zone between FY ice and the MY pack. Cool TBs correspond to rafts of MY floes; warm temperatures represent broad, frozen leads (Figure 7.3, C through E). The third zone, which is marked by decrease in the TB, width, and frequency of occurrence of frozen leads, corresponds to the MY pack (Figure 7.3, F and G). The TB of old ice also is at a minimum in this zone. Finally, the virtual absence of spikes or peaks indicative of significant leads in the TB profiles and a slight increase in the TB of old ice correspond to the region of intense deformation along the northern shore of Ellesmere Island (Figure 7.3, H through J).

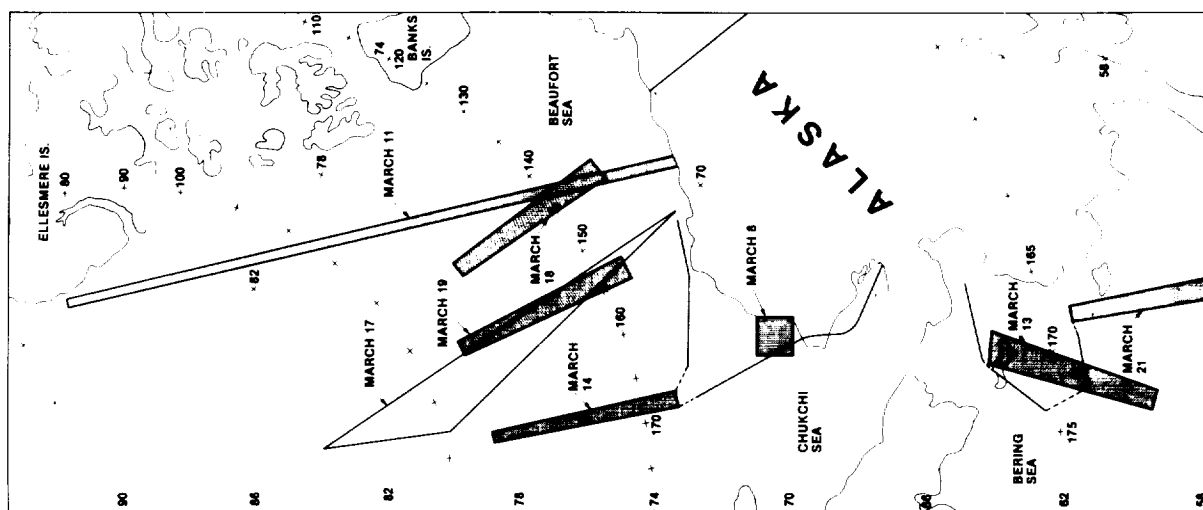


Figure 7.1. Map of Arctic areas covered by the NASA and Navy SSM/I underflights in March 1988.

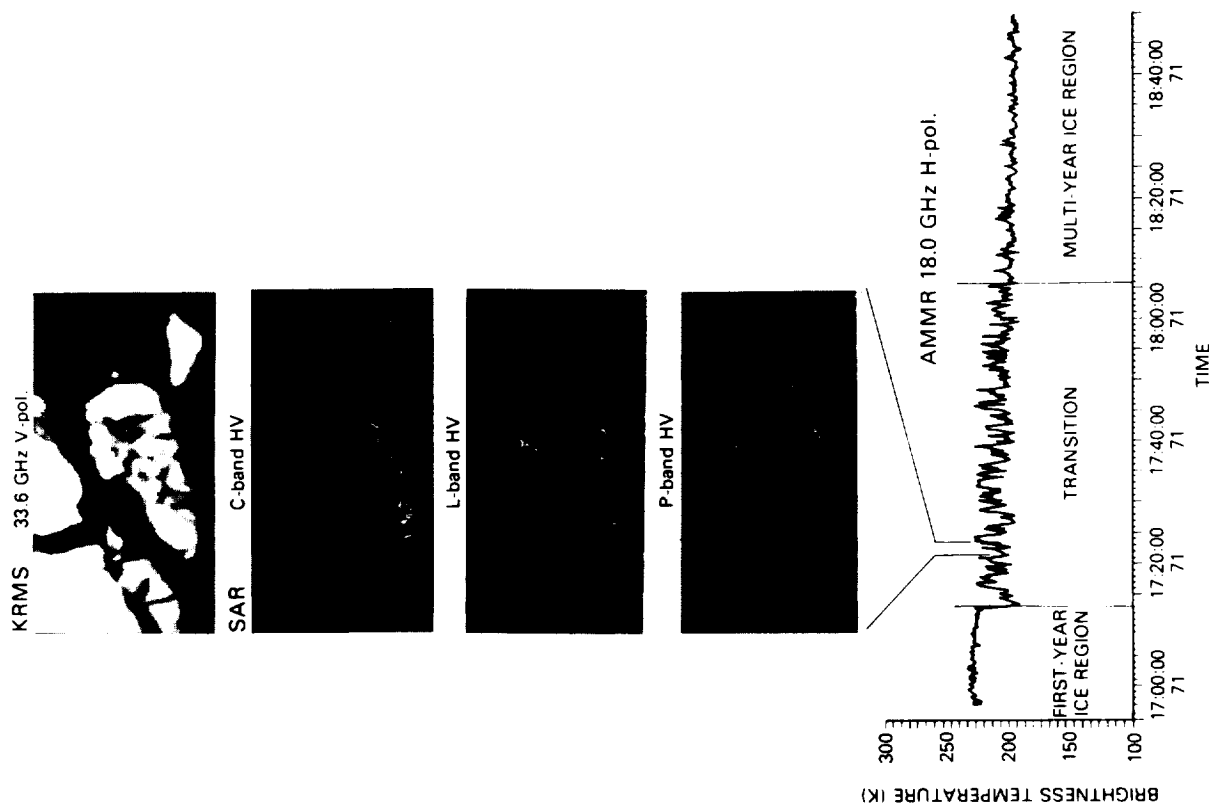


Figure 7.2. Comparison of (top to bottom) KRMS (33.6 GHz V-pol.), SAR (C, L, and P-bands), and AMMR (18 GHz H-pol.) data obtained with NASA and Navy aircraft over a portion of the Beaufort Sea during the March 11 transect flight.

# **BEAUFORT SEA TRANSECT** **11 March 1988**

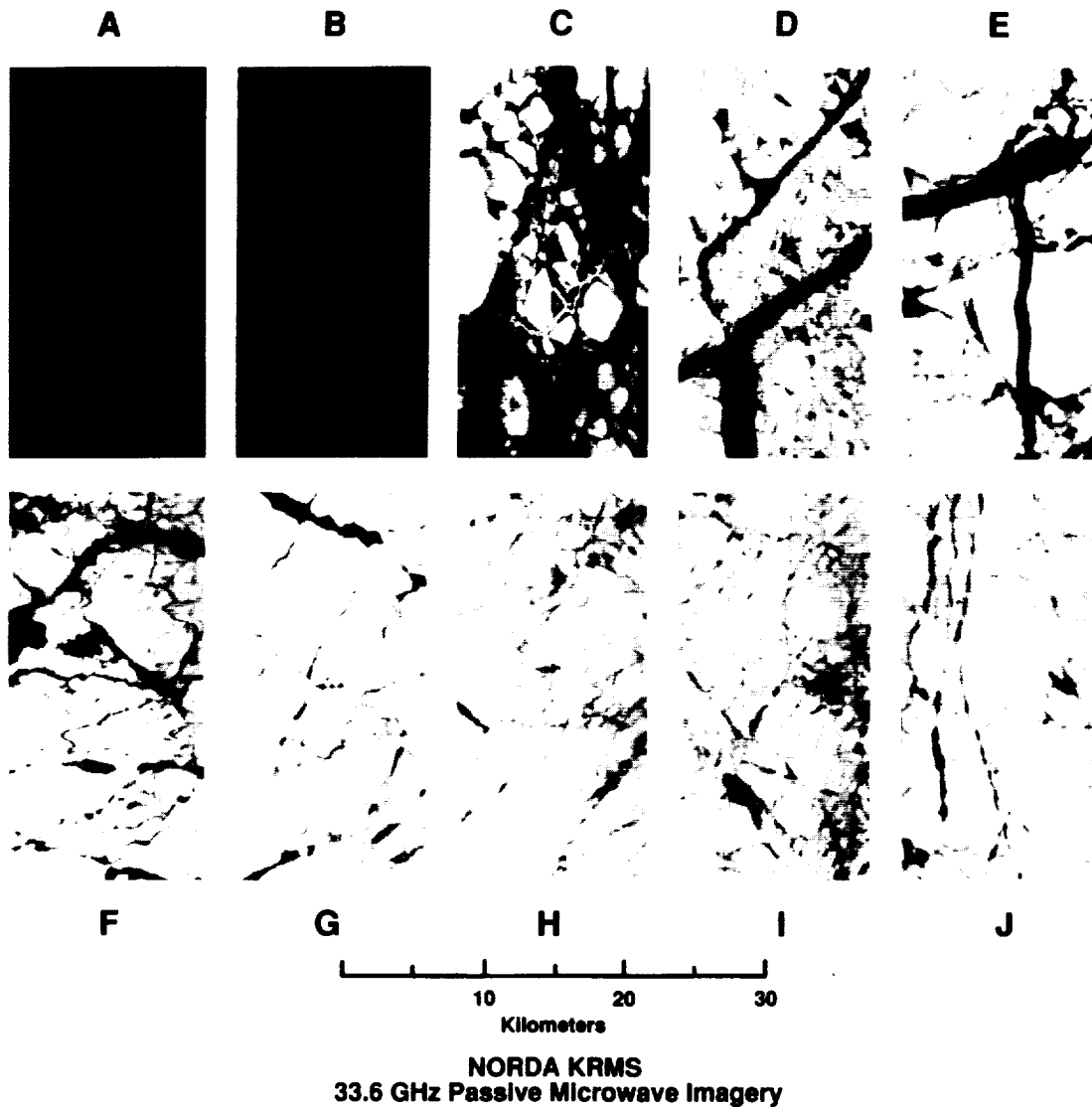


Figure 7.3. Representative KRMS images that show differences in ice characteristics along the Beaufort Sea transect shown in Plate 3 for March 11. Image A is at the beginning of the track near the Alaskan coast; image J is at the end of the track near the coast of Ellesmere Island. Intervening images are located at equally spaced intervals between these two end points. All ten images were printed using the same contrast enhancement so that a given grey tone corresponds to the same radiance in all images.

Ice concentrations along the flight track were calculated for the KRMS imagery using the computer-assisted method described in Chapter 8 and for the AMMR profile using the NASA multichannel sea ice algorithm with coefficients defined for the AMMR calibration. Total ice and MY concentrations were computed for the same 12-scan image segments used for the TB analysis discussed above. These data then were smoothed to reduce resolution of KRMS and AMMR data to the SSM/I scale. At this reduced resolution, total ice concentration is essentially 100% over the entire track, so only the MY concentrations are discussed here. These data are plotted with MY concentration data derived from SSM/I grid cells through which the flight track passes (Figure 7.5).

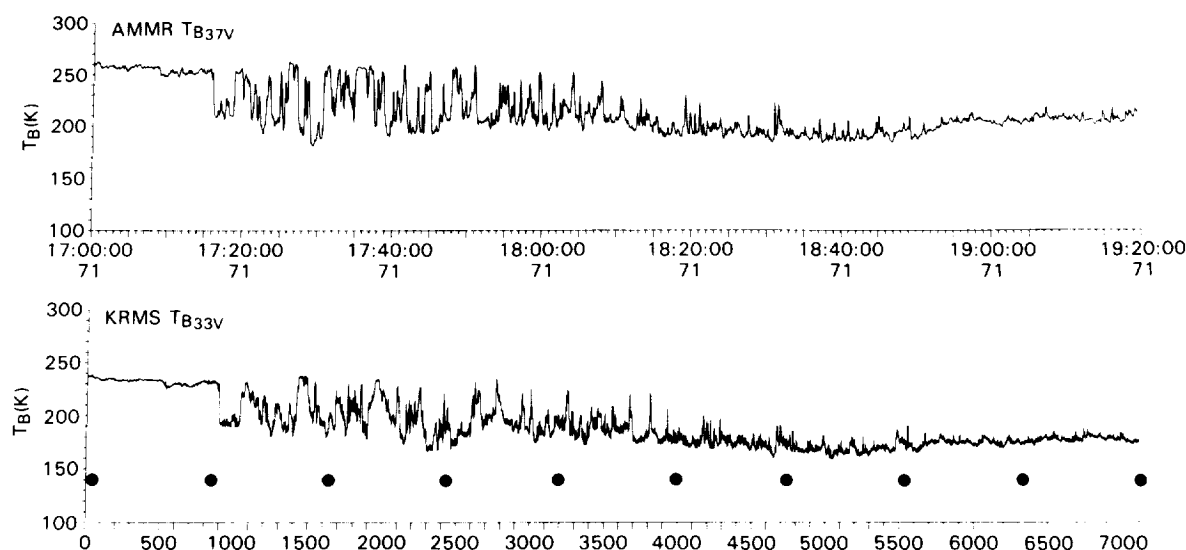


Figure 7.4. Brightness temperature plotted as a function of distance along the Beaufort Sea transect for the NASA's AMMR and NORDA's KRMS. Dots beneath the KRMS trace mark the position of images shown in Figure 7.3.

SSM/I retrievals represent concentrations integrated over the entire sensor footprint, of which the KRMS-AMMR swath represents only a fraction. The SSM/I profile thus lacks sharp changes in concentrations that are typical of the narrow field aircraft data, which are strongly influenced by local fluctuations in concentration caused by frozen leads. Nonetheless, the SSM/I profile mimics general trends shown by both AMMR and KRMS and agrees well over the transition zone and in the region of the MY pack.

All three profiles show a rise in concentration through the transition zone, and consistently high concentrations in the region of the MY pack. SSM/I concentrations, which reach a maximum of 90% and generally range between 80% and 90%, are lower than KRMS concentrations, which remain above 90% for the same interval. In some instances, the lower SSM/I concentrations may be a result of large lead systems present in the SSM/I cell outside the AMMR-KRMS swath. However, the fact that the SSM/I values fall consistently below the aircraft concentrations suggests that the algorithm slightly underestimates MY concentrations in this region.

AMMR and SSM/I retrievals depart significantly from KRMS concentrations both in the region of first-year ice along the Alaskan coast, and in the highly deformed region north of Ellesmere Island. Along the Alaskan coast the SSM/I algorithm consistently overestimates MY concentration, showing up to 20% MY ice where KRMS shows 100% FY ice. Discrepancies of half this magnitude or less were observed for the March 8 Cape Lisburne data set with SSM/I data that had been corrected for geolocation errors. This is discussed in the next chapter.

North of Ellesmere Island differences between SSM/I-AMMR MY concentration retrievals and KRMS ground truth data are more dramatic. KRMS concentrations consistently exceed 90% and approach 100% at several points (Figure 7.3, I and J; Figure 7.5); whereas, SSM/I retrievals drop as low as 40% and AMMR retrievals, as low as 50% over this same interval (Figure 7.5). The point at which the SSM/I concentrations depart from concentrations observed in KRMS images coincides with a 10-K to 15-K increase in minimum MY TB observed in both KRMS and AMMR data (compare Figures 7.4 and 7.5). The observed deviations in algorithm-derived concentrations result from differences between local ice TB at 19 GHz and 37 GHz.

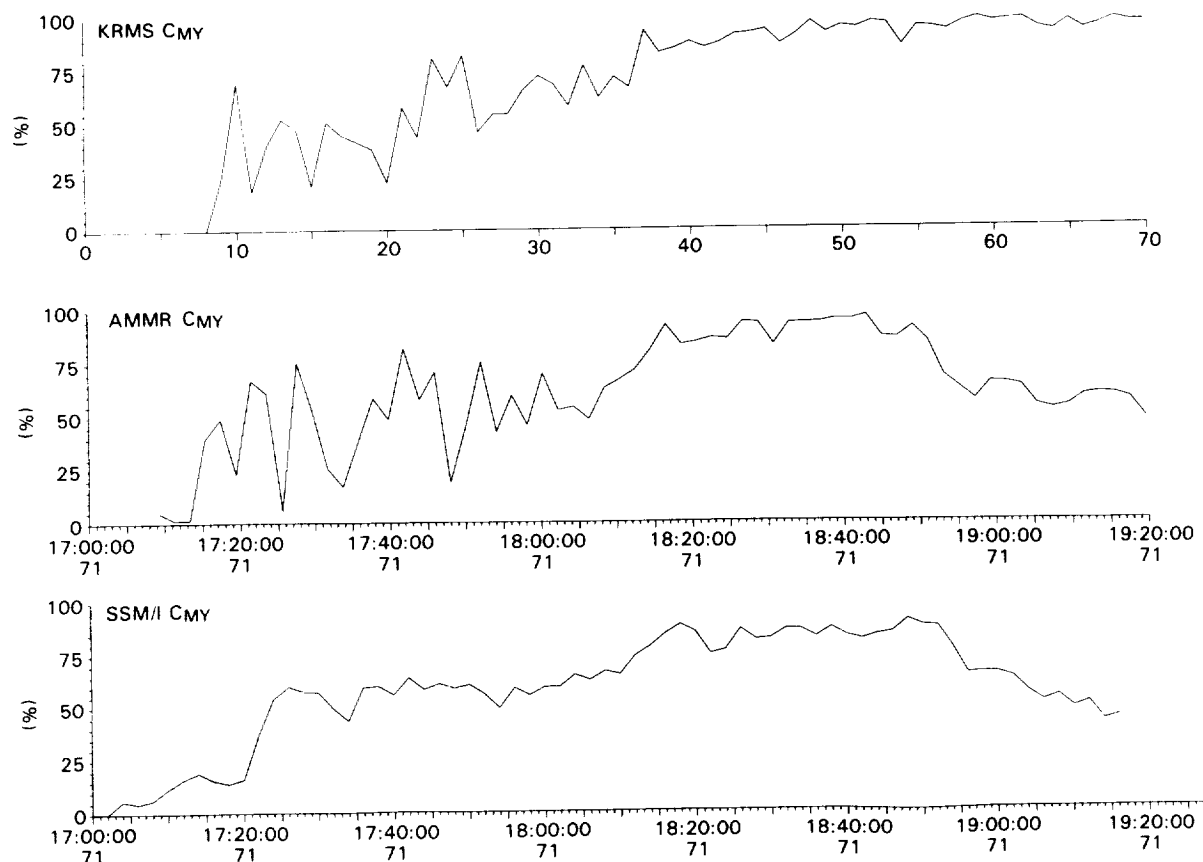


Figure 7.5. Multiyear ice concentrations derived from KRMS, AMMR, and SSM/I plotted as a function of distance along the Beaufort Sea transect.

Anomalously low concentrations of MY ice mapped in coastal regions of Ellesmere Island by the SSM/I algorithm probably are related to radiometric changes in the character of the pack caused by extreme deformation typical of this area. The region is located where the Beaufort Gyre flows shoreward and converges on the coast (Colony and Thorndike, 1984). This shoreward flow maintains pressure on the pack, keeps ice pinned against the coast for much of the year, and enhances deformational processes. Historically, ice here has been reported to be among the roughest, thickest, and oldest in the Arctic; models that incorporate forcing by current and wind fields predict mean ice thicknesses that exceed four meters (Hibler, 1979) and mean ice age in excess of 6 years (Thorndike, 1986).

Radiometric warming of old ice, which the SSM/I algorithm interprets as a mixture of FY ice and MY ice, can be explained in terms of physical changes related to ice deformation. In particular two processes, one related to deformation of old ice floes and the other to collapse of recently formed leads, contribute to this warming.

KRMS images show that where MY ice warms radiometrically, the pack is highly fragmented (Figure 7.3, I and J). Floe sizes are smaller than at other points along the flight track, and a greater percentage of the pack appears to consist of brash that surrounds the many small floes. The brash consists of fragments of both MY ice, abraded from floe boundaries when floes collide or fracture, and FY ice, either formed in place in gaps between the MY chunks or liberated from frozen leads or fractures. The mean TB of this brashy mixture is intermediate between FY ice and MY ice and contributes to the observed warming of TB integrated across SSM/I grid cells.

Frozen leads occur in this region in spite of the high deformational rate. Leads here differ from those imaged farther south along the transect, however, in that typically they are narrower and they extend for shorter distances

(compare Figure 7.3, I and J, with C through G). Shear along leads also appears to be more common, inasmuch as fragments of fractured floes separated by leads seldom occur opposite each other. Pressure exerted on the pack probably closes most leads shortly after they form. As these leads collapse, saline young ice that froze within them is thrust into ridges atop adjacent MY ice. Some saline ice also becomes trapped between adjacent MY floes. We hypothesize that repeated formation and collapse of leads both lifts a significant amount of FY ice onto MY floes and entraps a substantial quantity of FY ice between the floes, increasing the bulk salinity of the MY pack and warming radiometric temperature across SSM/I grid cells throughout the region in which intense deformation occurs.

MY concentrations retrieved from the algorithm for cells in this region thus probably represent, as they do in other regions, the relative proportions of saline and nonsaline ice that are present in the pack. However, the interpretation that must be applied here to concentration retrievals departs from conventional interpretations in which multiyear concentration equates to percentages of the surface area within a cell that consists of MY floes and relatively undeformed FY ice in leads. Instead, MY concentrations in this region represent the degree to which the bulk salinity of imaged surfaces has been raised by incorporation of FY ice into the MY pack as brash and ridges. As such, the degree to which MY retrievals depart from 100% in this region may indicate the relative intensity of deformation that has occurred. This difference in interpretation is significant. The former interpretation provides the user with the ratio between thin FY ice and thick MY ice; the latter offers the opportunity to derive potentially important information regarding ice deformation and pack kinematics.

The JPL SAR and GSFC AMMR sensors on the DC-8 provided, for the first time, a spatially and temporally coincident, fully polarimetric, multispectral active/passive comparison of sea ice characteristics. The fixed-beam AMMR antennas were configured to record TBs inside the SAR swath at 45° incidence. Precision colocation was accomplished during post processing by incorporating aircraft attitude information from the Inertial Navigation System (INS). This enabled registration of the center point of each AMMR-integrated field of view (IFOV) to known SAR pixel locations.

The colocation of the data sets was made possible by indexing the SAR and AMMR data streams using the indicated aircraft time as supplied by the DC-8 housekeeping system. Every second, this system routinely records all pertinent instrument and aircraft parameters including INS navigation, ground speed, and universal time, thus enabling cross-comparison of data and aircraft parameters. To account for changes in aircraft ground speed in the AMMR data, INS, universal time, and radar configuration parameters were recovered for 5 records, each separated by 3-minute intervals along 15-minute radar image segments. These equally-spaced control points were subsequently used to match the data streams by interpolating the location of the remaining AMMR measurements with respect to the motion-compensated SAR data records. The result is that each AMMR data point was matched with every 9th or 10th SAR record depending on the ground speed of the aircraft.

The JPL SAR transmits energy at 0.4 GHz (P-band), 1.25 GHz (L-band), and 5.3 GHz (C-band) simultaneously, transmitting and receiving from separate antennas in HH, VV, HV, and VH polarization combinations and recording amplitude and phase of the returned signal. For the purposes of this study, 26 m resolution-survey processed data were used, since these provided contiguous strips of SAR image data up to 200 km in length. C-band VV-polarization SAR data were chosen and used exclusively for comparison purposes, largely because it gives good contrast between FY and MY sea ice classes. Color Plate 4 shows a segment of C-band VV SAR data (for display purposes the segment has been divided into 4 columns) collected over the March 11 transect of the Beaufort Sea MY/FY ice transition zone. Monochrome strips represent a grey level display of relative backscatter magnitude in which light tones correspond to MY ice (high backscatter) and dark tones to FY ice (low backscatter). Corresponding color-coded strips are the result of a clustering algorithm which separates FY ice (blue) from MY ice (red) in the C-band data. SAR pixels corresponding to the center of the AMMR IFOV are located inside the SAR swath. These points are represented by "+" characters on both the original (black and white) and clustered (color) images. Marks located along either side of the center points correspond to the limits of the 3 dB footprint for each integration period as represented by the AMMR 37-GHz antenna pattern. Values indicated between the corresponding color and black and white image strips represent the 37-GHz TB

times ten for each AMMR 1-second integration period. Zero values indicate instrument calibration cycles (approximately every 60 seconds).

The technique used to obtain accurate MY ice concentrations from the SAR data involved two procedural levels. The first stage involves smoothing the image using a 3 x 3 moving box filter to reduce speckle, and then applying an unsupervised Bayes classifier to separate recognizable subcategories of FY and MY ice. In the second stage of processing, a supervised Bayes maximum likelihood classifier was employed, based on the assumed knowledge of the probability distribution over the range of classes and the known cluster centers. The resulting classification into MY and FY ice is based upon minimum distance of each image pixel to the cluster centers. This operation is carried out on a pixel-by-pixel basis, resulting in MY ice pixels coded in red and FY ice pixels coded in blue. Similar SAR ice classification techniques have recently been employed by Holt et al. (1989; 1990). They used a comparable Bayes maximum likelihood method and compared their classification results with aerial photographic interpretation. This comparison indicates a 3%-7% accuracy for MY ice concentration estimates from the C-band VV-pol. aircraft SAR data.

This coregistration of the AMMR and SAR data is providing the first accurate high-resolution comparison of active- and passive-microwave data sets over Arctic sea ice. Preliminary results comparing C-band SAR with 37-GHz AMMR data from the Beaufort Sea show an unusually strong inverse correlation ( $r = -0.94$ ) across the FY to MY ice transition zone. A comparison of 5.3 GHz mean SAR pixel values (representing relative backscatter magnitude) and AMMR TBs from the IFOV of the 37-GHz antenna is presented in Figure 7.6. Bright C-band radar signatures, associated with low-salinity MY ice, correspond with low TBs, probably because of volume scattering by bubbles within the ice, or a low-density snow-ice layer near the ice surface. In contrast, low backscatter and high microwave emission from young and smooth FY ice results in a low SAR return and high radiometric brightness.

A comparison between MY ice concentrations derived from the SAR classification and from an SSM/I-type algorithm using the AMMR data set is shown in Figure 7.7. The solid line indicates the SAR estimates, and the dashed

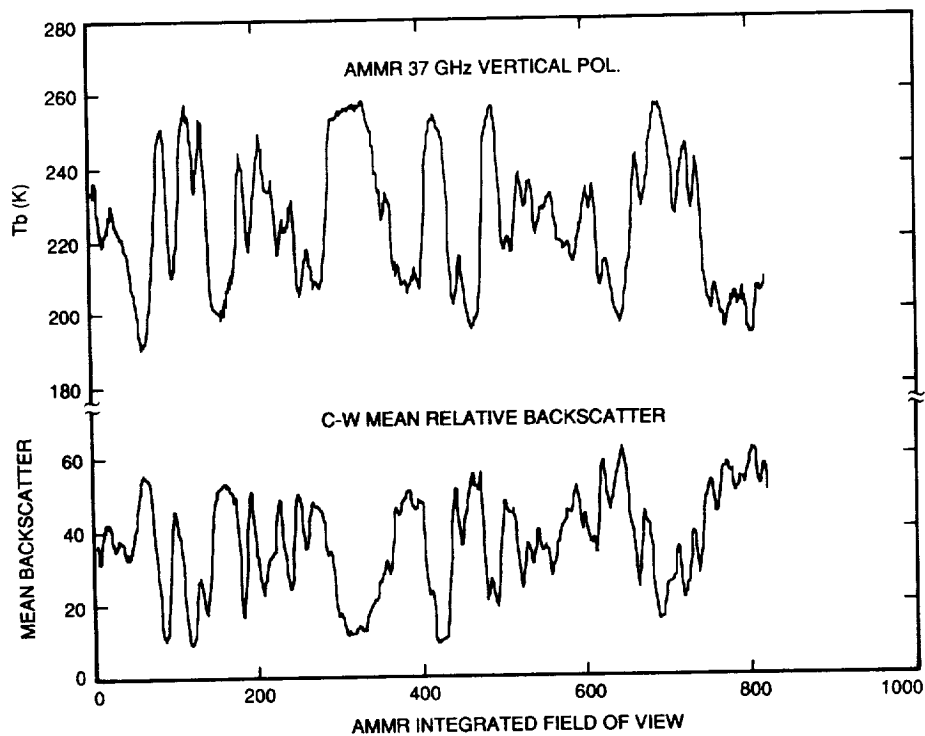


Figure 7.6. Comparison between the AMMR 37 GHz V-pol. brightness temperature (Tb) and the C-band V-V SAR mean backscatter for over 800 AMMR FOVs.

line indicates the AMMR concentrations. Generally there is good correspondence between the two traces that have a linear correlation of  $R = 0.89$ . In many areas estimates appear to be extremely close; whereas, in certain instances departures occur. Differences where SAR-derived concentrations are greater than the AMMR concentrations appear, in some cases, to be the result of small underestimates of the MY ice fraction by the AMMR algorithm. Other errors of unknown magnitude are associated with the AMMR antenna pattern as it overlays the SAR image. These departures require further investigation. The mean difference between the two concentrations is 6% with a standard deviation of the differences of 14%.

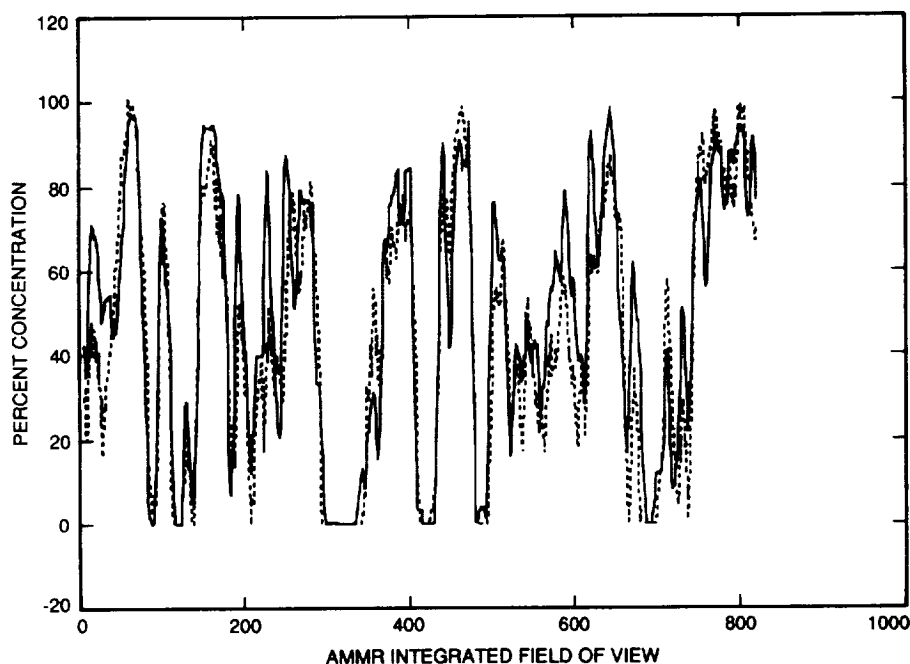


Figure 7.7. Comparison between SAR (solid line) and AMMR (dashed line) MY ice concentrations for the same 800 FOVs shown in Figure 7.6.

#### 7.4.2 Ice Edge Location

Ice-edge crossings were made with the NASA DC-8 during the Bering Sea flights of March 13 and 21. These two flights provided the precise location of ice-edge features required for determining the appropriate SSM/I ice-concentration contour to use for locating the ice edge on the SSM/I grid. The NASA DC-8 carried two GPS receivers, which were used routinely to check the accuracy of the aircraft INS. Typical differences between the GPS and INS aircraft positions for the two Bering Sea flights ranged from 1 to 1.5 km (W. Krabill, priv comm). Thus, the aircraft INS error is small compared to the 25-km SSM/I grid used in this comparison. On March 13, there were three usable crossings of the ice edge by the NASA DC-8. The fourth crossing was contaminated by aircraft roll. On March 21, all four crossings were usable.

Because the ice edge is not a sharp boundary, the definition of the ice-edge location is somewhat arbitrary. For the purpose of comparing the location of the ice edge using the aircraft AMMR data with the SSM/I sea ice concentrations on a 25-km grid, the ice-edge position was defined in two ways. First, the ice edge was defined as the location of the first ice band encountered by the aircraft flying from open ocean to the ice pack; the second ice-edge definition was the position of the edge of the main pack. For each of the two definitions, the SSM/I ice concentration (determined without

the use of the algorithm GR weather filter) corresponding to the 25-km SSM/I grid containing that particular ice-edge location is given in Table 7.3.

On average, the SSM/I ice concentration for the grid containing the initial ice band is about 15%; whereas, the concentration corresponding to the position of the main pack is about 38% (Table 7.3). The importance of this result is that it suggests that the SSM/I 15% ice-concentration contour, on average, locates the outer ice-edge position, defined as the location of the initial ice band. These results also suggest that the use of the GR weather filter, which eliminates ice concentrations of less than 15% on SSM/I grid maps, really eliminates only the spurious ice concentrations associated with the smearing of the ice edge by the finite width of the SSM/I antenna pattern.

Table 7.3. Comparison of SSM/I Ice Concentrations Corresponding to Ice-edge Features as Determined From Aircraft Crossing

Date	Crossing	SSM/I CT (Ice Band)	SSM/I CT (Main Pack)
Mar 13	1	11%	46%
	2	20%	32%
	3	20%	46%
Mar 21	1	13%	28%
	2	15%	61%
	3	15%	28%
	4	13%	25%

## 7.5 Conclusions

The high contrast between FY and MY ice types observed in the KRMS imagery and in the C-band SAR imagery for the March 11 transect of the Beaufort Sea and the excellent agreement in FY/MY ice-type discrimination among the KRMS, SAR, and AMMR sensors (Figure 7.2) provide the basis for using the aircraft data as a validation tool for the SSM/I maps of MY ice concentration.

Comparison of the aircraft passive and active sensor data with the SSM/I MY ice-concentration map for March 11 establishes the validity of the four zones apparent in the SSM/I MY ice concentration (Plate 3). First, the zone of low MY ice concentration (less than 25%) observed in the SSM/I data off the Alaskan coast is an area of FY ice types. This is verified by both active- and passive-microwave sensors. The source of these spurious low MY ice concentrations observed in both the SSM/I imagery, as well as in the AMMR-derived MY concentrations, appears to be FY ice types having different spectral gradient signatures. This is based on an analysis of both the KRMS imagery and the multifrequency AMMR data. The source of this spectral variability is discussed in the next chapter.

The second zone, a transition zone starting near 72.5°N latitude, is identified using both the KRMS and SAR imagery as one of mixed FY and MY ice (Figure 7.2). The SSM/I image is in qualitative agreement showing MY ice concentrations ranging from about 35% to 70%. Direct comparisons between KRMS and SAR mosaics with SSM/I maps provide a quantitative measure of the accuracy of the SSM/I concentrations and are presented in the next two chapters.

The coincident observations of this transition zone by the JPL SAR and the AMMR provide, for the first time, multifrequency, polarimetric active/passive measurements made from the same aircraft platform. The SAR/AMMR agreement was significant ( $r = 0.89$ ) with an average SAR/AMMR MY ice difference of  $6\% \pm 14\%$ .

The third zone, labeled MY ice in Figure 7.2, also qualitatively agrees with the aircraft data that classifies it as a zone of high MY ice concentration. Concentrations greater than about 75% are observed in the AMMR concentrations shown in Figure 7.5, while the SSM/I map indicates concentrations in the range of 70% to 90% (see Plate 3).

The fourth zone, a zone of low MY ice concentration off the coast of Ellesmere Island, is associated with a region of highly fragmented ice in the KRMS imagery. The floes are smaller, and a higher fraction of the pack appears to consist of brash ice. The higher concentration of saline ice (FY ice), as indicated by the SSM/I image, is not inconsistent with the KRMS observations, in the sense that the SSM/I provides an integrated measure of the areal extent of saline ice including areas of saline ice covering some of the older ice floes. In this situation, the SSM/I no longer provides an areal measure of MY ice, but potentially offers a means of observing areas of ice deformation. The problem then is discriminating unambiguously between these two situations.

Aircraft flights across the Bering Sea ice edge on March 13 and 21 provided the precise location of ice-edge features with which to compare SSM/I sea ice concentrations. On average, the SSM/I ice concentration corresponding to the initial seaward ice band encountered by the aircraft is 15%. The concentration corresponding to the position of the main pack is 38%. These results suggest that the use of the GR weather filter, which eliminates ice concentrations of less than 15% on SSM/I grid maps, really eliminates only the spurious ice concentrations associated with the smearing of the ice edge by the finite width of the SSM/I antenna pattern.

## 7.6 References

- Cavalieri, D. J., *NASA Sea Ice and Snow Validation Program for the DMSP SSM/I: NASA DC-8 Flight Report*, NASA Technical Memorandum 100706, 143 pp., September 1988.
- Colony, R., and A. S. Thorndike, An estimate of the mean field of Arctic sea ice motion, *J. Geophys. Res.*, 89, 10623-10629, 1984.
- Eppler, D. T., L. D. Farmer, A. W. Lohanick, and M. C. Hoover, Classification of sea ice types with single-band (33.6 GHz) airborne passive microwave imagery, *J. Geophys. Res.*, 91, 10661-10695, 1986.
- Hibler, W. D. III, A dynamic-thermodynamic sea ice model, *J. Phys. Oceanogr.*, 9, 815-846, 1979.
- Holt, B., R. Kwok, and E. Rignot, Ice classification algorithm development and verification for the Alaska SAR facility using aircraft imagery, in Proceedings, IGARSS '89, vol. 2, *Cat. No. 89CH2768-0*, pp. 751-754, IEEE, New York, 1989.
- Holt, B., R. Kwok, and E. Rignot, Status of the ice classification algorithm in the Alaska SAR facility geophysical processor system, in Proceedings, IGARSS '90, vol. 3, *Cat. No. 90CH2825-8*, pp. 2221-2224, IEEE, New York, 1990.
- Thorndike, A. S., Kinematics of sea ice: in Untersteiner, N., ed., *The Geophysics of Sea Ice*, Plenum Press, New York, p. 489-549, 1986.



## Chapter 8

### SSM/I AIRCRAFT UNDERFLIGHTS: SSM/I-KRMS COMPARISON

Duane T. Eppler and L. Dennis Farmer  
Naval Oceanographic and Atmospheric Research Laboratory  
Hanover, New Hampshire 03755

and

Donald J. Cavalieri  
Laboratory for Hydrospheric Processes  
NASA Goddard Space Flight Center  
Greenbelt, Maryland 20771

8.1 Introduction .....	69
8.2 KRMS Instrument Description .....	69
8.3 SSM/I-KRMS Comparison .....	72
8.4 Discussion .....	76
8.5 Conclusions .....	78
8.6 References .....	79

#### 8.1 Introduction

In this chapter, the results of a direct areal comparison between SSM/I and KRMS sea ice concentrations are presented. KRMS images of sea ice were acquired in four different Arctic areas: the southern Chukchi (Cape Lisburne), northern Chukchi, Beaufort, and Bering sea regions. Aerial mosaics were obtained on three of these four flights. On the evening of March 8, an aerial mosaic was flown over the coastal waters of Cape Lisburne. During daylight hours, mosaics were flown on March 13 in the Bering Sea between St. Lawrence and St. Matthews islands and on March 14 in the northern Chukchi Sea between 73.0° and 75.5°N latitude, centered on 168.0° longitude. Results from an comparison of SSM/I and aircraft ice concentrations for the Chukchi Sea and Cape Lisburne mosaic data sets are discussed in this chapter. The Bering Sea data set is of marginal value to this initial stage of analysis because both the total and MY ice concentrations are invariant over the entire mosaic (total ice concentration is 100%, MY concentration is 0%). These data will figure prominently, however, in subsequent efforts to develop thin ice algorithms for SSM/I data.

The primary objective of the KRMS underflight of March 8 in the vicinity of Cape Lisburne was to verify the persistent pattern of increasing MY ice concentration observed in the SSM/I imagery, which ranged from 0% just off the Cape Lisburne coast to 20% or 30% near 71°N. The March 14 underflight covered an area farther north in the Chukchi Sea from approximately 73°N to approximately 75.5°N latitude. This area was chosen for the purpose of verifying the more gradual gradient in MY ice concentration observed in the SSM/I imagery than that observed in the Beaufort Sea transect flight of March 11 discussed in Chapter 7. In this area of the Chukchi Sea, the SSM/I algorithm shows MY ice concentrations ranging from about 30% to 50%. Analysis of these two KRMS data sets provides not only a measure of SSM/I ice concentration accuracy, but also some physical insight into the sources of error associated with SSM/I ice-type discrimination.

#### 8.2. KRMS Instrument Description

KRMS is a passive, airborne, microwave imager that operates at a center frequency of 33.6 GHz. The instrument is pod-mounted and, in its present configuration, is hung from the bomb bay of a P-3A aircraft. Table 8.1 provides salient engineering characteristics of KRMS. Expanded descriptions of the instrument and methods used to process KRMS data

are provided by Heydlauff and Seybold (1983), Eppler et al. (1984, 1986), Farmer et al. (1989, 1990), and Eppler and Heydlauff (1991).

#### 8.2.1. Scan Geometry

KRMS senses vertically polarized microwave emissions from the Earth's surface through three parabolic antennas. The three antennas, mounted 120° apart on a single shaft, rotate about a horizontal axis that is parallel to the

Table 8.1. KRMS Technical Characteristics

ANTENNAS	
Number	3
Diameter	24 in
Polarization	vertical
Beam Width	1.0°
Isolation (minimum)	40 dB
SCANNER	
Maximum Scan Rate	25.0 rev/s (40 ms/scan)
Minimum Scan Rate	7.5 rev/s (133 ms/scan)
Scan Angle (measured from nadir)	60°
Midscan Incidence Angle	0°
Swath Width	3.46 x altitude
Antenna Position Accuracy	2.5 min. of arc
STABILIZATION	
Method	cross-track roll gyro
Accuracy	0.25°
RF AMPLIFIER	
Type	Superheterodyne (DSB)
Noise	5.0 dB
Bandwidth	1.3 GHz
Gain	60 dB
Loss (maximum)	1.2 dB
RADIOMETER	
Type	Pulse Stabilized, Total Power
Pulse Width	4.0 ms
Local Oscillator Frequency	33.6 GHz
Video Bandwidth (maximum)	1.7 kHz
Video Gain (nominal)	72 dB
Minimum Detectable Signal	0.05 K/s
Sensitivity (nominal)	50 mV/K
Dynamic Range	370 K

direction of flight; they scan in a vertical plane (Figure 8.1). At any given instant, at least one of the antennas faces Earthward. Electronics in the instrument pod switch from one antenna to the next as the antenna assembly rotates so that only the signal from the downward facing antenna is recorded. During each rotation, each antenna, in turn, scans a  $120^\circ$  field of view centered at aircraft nadir, of which only the center  $100^\circ$  is digitized. Resultant crosstrack coverage across this  $100^\circ$  field is equal to 2.38 times the altitude, or approximately 14.5 km at 6.1 km (47,600 ft at 20,000 ft), the altitude from which the KRMS validation data set was acquired.

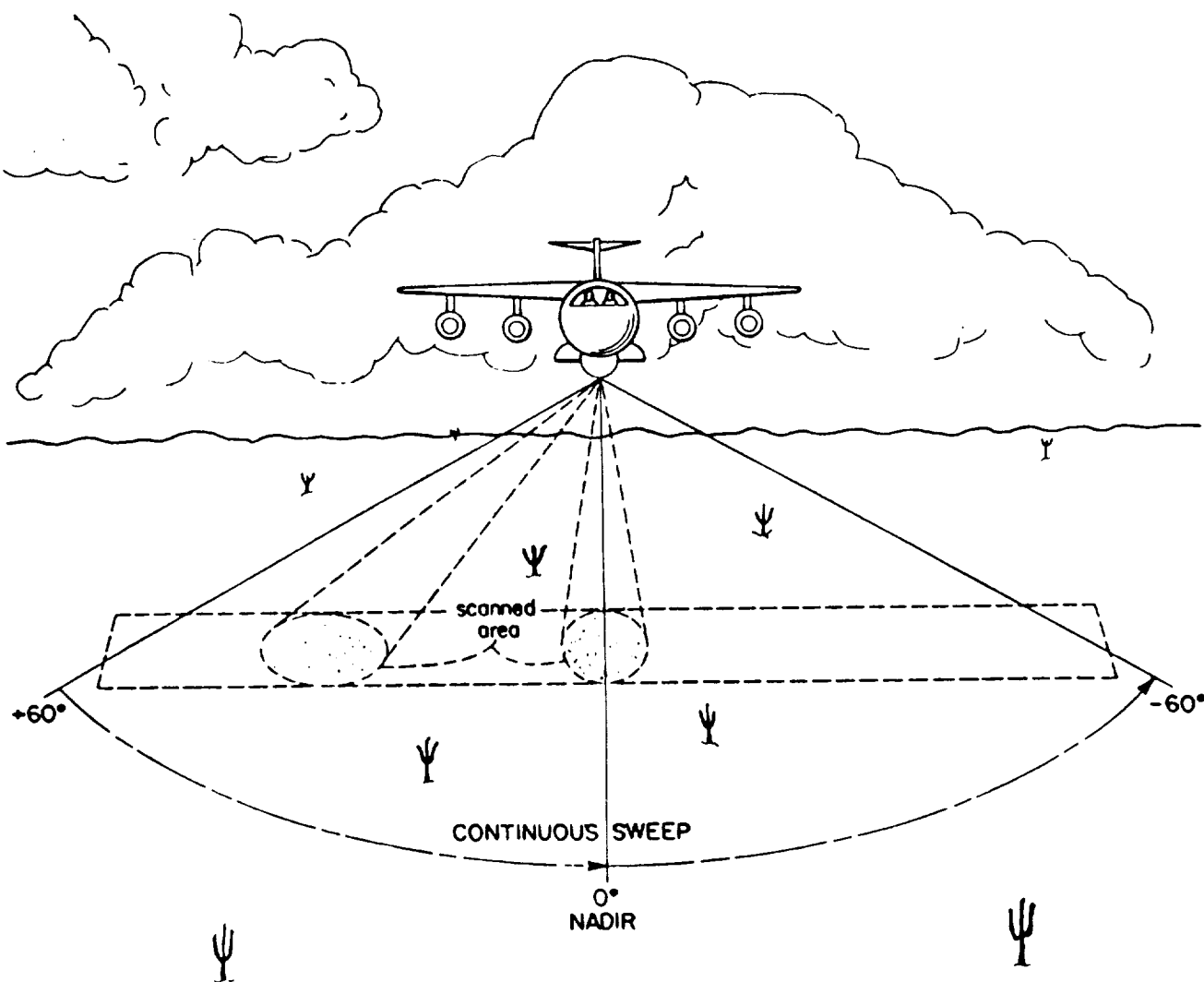


Figure 8.1. KRMS scan geometry. Each scan consists of data collected across a  $1^\circ$ -wide swath that extends across a  $120^\circ$  field of view. Only those data within the central  $100^\circ$  of the swath are digitized. The footprint subtended by the  $1^\circ$  antenna beam increases with the magnitude of the off-nadir pointing angle. Spatial resolution at image limbs is degraded with respect to nadir resolution as a result.

Three scan lines, one from each antenna, are recorded for each rotation of the antenna assembly. Downtrack motion of the aircraft moves the position of the ground swath swept by each successive scan farther along track. An image is built simply by recording successive scans. A trained operator in the aircraft manually adjusts the rate at which the antenna assembly rotates. In this way, scan rate is matched to altitude and ground speed, both to insure adequate oversampling between successive scans (nominally 80%) and to preserve correct image geometry in the downtrack direction.

### 8.2.2. Sensor Resolution

KRMS' minimum detectable signal as measured in the laboratory is 0.05 K/s; operational sensitivity is believed to be 0.5 K or better. The 3-dB beam width of each antenna is 1°, which subtends a circular beamspot on the ground at nadir that is approximately 5.3 m in diameter per 300 m (17.5 ft per 1000 ft) of flight altitude. For the validation data set, which was acquired at 6.1 km (20,000 ft), the nadir beam spot measured approximately 106 m (350 ft).

The size of the beam spot is not constant across the image. Because of the scan geometry, the incidence angle from which the sensor views the surface varies across the 100° field of view. The size of the antenna footprint, its ellipticity, and the surface area subtended by the beam spot increase with off-nadir angle; sensor resolution decreases as a result. At image limbs (incidence angle of 50°) the beam spot size in the crosstrack direction is enlarged by more than a factor of three to 19.9 m (66.3 ft) per 300 m (1000 ft) of altitude. For the validation data set, then, the beam spot at the edge of the image measures 398 m in the crosstrack direction.

### 8.2.3. Image Characteristics

Each scan, which initially is stored in real time aboard the aircraft as an analog signal on magnetic tape, is digitized in the laboratory into 512 pixels (Eppler and Heydlauff, 1991). The ground dimension of nadir pixels in the SSM/I validation image set is approximately 28 m. Digitizing electronics sample the signal nonlinearly with respect to time so that the ground spacing between pixel centers in the resulting image is uniform across the 14.5-km swath (Heydlauff and Seybold, 1983). Information in each of the 512 pixels overlaps that in the previous pixel in the scan by approximately 80%, which matches downtrack overlap and preserves geometric integrity of the image. Pixel values, which represent relative radiances measured by the KRMS radiometer, can be converted to brightness temperatures using methods described by Farmer et al. (1989, 1990).

## 8.3. SSM/I-KRMS Comparison

### 8.3.1. Method of Analysis

Prints of KRMS images from the Cape Lisburne and Chukchi regions were laid as aerial mosaics. Pixel coordinates that delineate areas of overlap between adjacent flight tracks were noted as required to avoid sampling the same area twice during subsequent machine processing. Navigation data from KRMS flight logs (Farmer et al., 1989) were used to construct a latitude-longitude grid on each mosaic. These coordinates were used to locate cell boundaries of the NASA SSM/I grid, which were plotted on the mosaic. The mosaics with the SSM/I grid overlay are shown in Figures 8.2 and 8.3 for the Cape Lisburne and Chukchi Sea regions, respectively. Ice concentrations within each grid cell then were computed from KRMS imagery.

Ice concentrations were derived using two different methods, depending on the distribution of ice types present. In regions where the pack consisted of mixtures of MY and FY ice (Chukchi Sea, Beaufort Sea), a computer-assisted classification scheme was applied to discriminate between open water, FY ice, and MY ice. Where the pack consisted predominantly of FY ice (Cape Lisburne), old ice and open water areas were measured manually using a compensating polar planimeter.

1. Computer-Assisted Classification: Open water, MY ice, and FY ice each are characterized by discrete, non-overlapping ranges of TBs in 33.6-GHz passive-microwave images (Eppler et al., 1984, 1986). KRMS images can be classified into these three surface types by applying conventional level slicing techniques to radiances recorded in KRMS data. Training regions that include the range of radiances observed for each surface type are used to determine minimum and maximum values for each class. These values are used to set break points that define radiance boundaries between classes. Each pixel in the image then is classified with respect to ice type on the basis of its numeric value, and the percentage of the scene composed of different surfaces is derived from counts of the number of pixels assigned to each category.

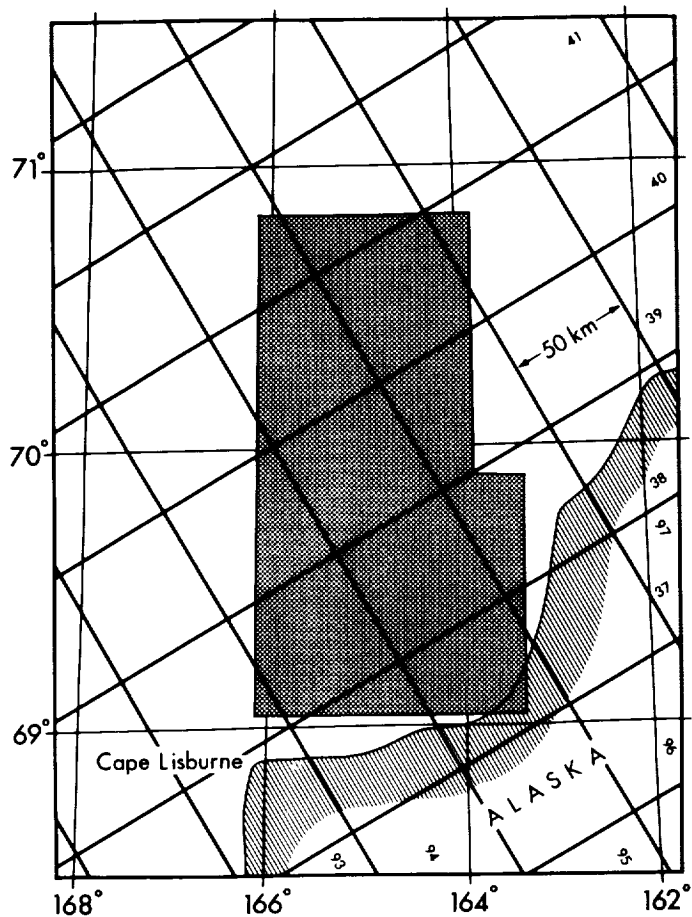


Figure 8.2. Location map of the KRMS Cape Lisburne mosaic. The shaded box encloses the area imaged in the mosaic. These boundaries are approximate; in most instances, the area imaged extends slightly beyond the area shown. Cell boundaries of the NASA SSM/I 50-km grid (heavy lines) are superimposed on the latitude-longitude grid (light lines). Small numbers along the right-hand margin and bottom margin refer to row and column coordinates of the SSM/I grid.

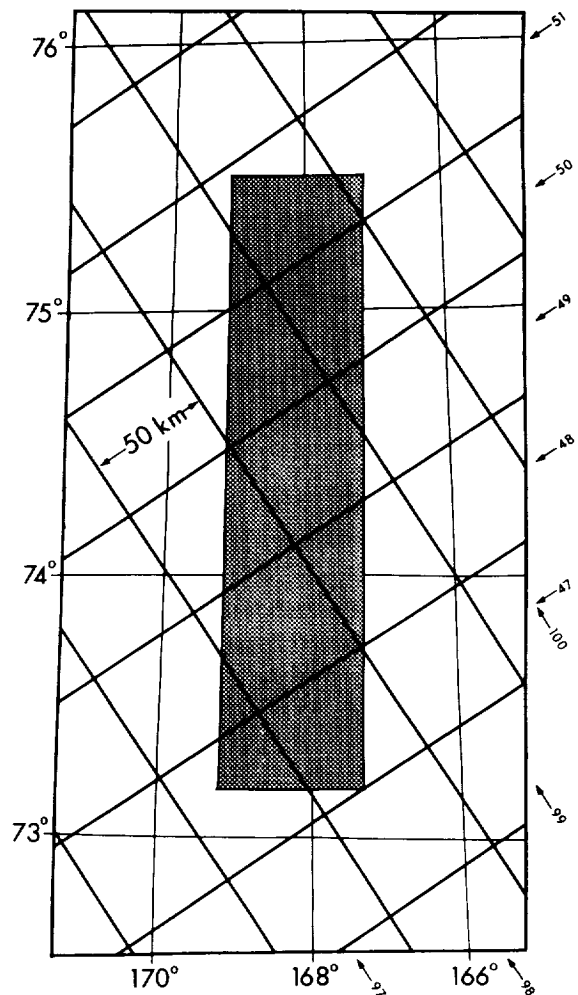


Figure 8.3. Location map of the Chukchi Sea mosaic. Refer to caption for Figure 8.2 for additional explanation.

The procedure is supervised, which reduces error and increases reliability of the results. Classification software permits each scene to be displayed with surfaces classified according to the current set of break points. The analyst can compare the classified image with the original image, verify the accuracy of the classification in real time, and adjust break points as appropriate. Nonetheless, two sources of error persist, one of which is related to radiometric characteristics of new ice at 33.6 GHz and the other, to the resolving power of KRMS' three antennas.

First, radiances typical of new ice (slush, frazil, nilas) coincide with the range of radiances observed for both MY ice and FY ice. Thus, where new ice is present with FY ice and MY ice, it is misclassified as either MY ice or FY ice, depending on the type and thickness of the new ice. New ice occurs in only a few KRMS images of the Beaufort and Chukchi validation data sets. The data were collected during a quiescent period in which pack deformation required

to expose open water and create new ice was minor. In the few instances where new ice does occur, it typically is confined to cracks and narrow leads and comprises a fraction of a percent of the total surface area in any given SSM/I footprint. For the Beaufort and Chukchi images to which computer assisted methods were applied, then, misclassification of new ice is not a significant source of error\*.

The second source of error arises from ambiguities that occur when the KRMS radiometer images feature smaller than the antenna beam spot. Such features include cracks and narrow leads that occur within MY floes and that are filled with FY ice, and small chunks of MY ice frozen in a FY ice matrix. These features do not fill the antenna beam spot, so the measured radiance consists of an integrated value that reflects the relative abundance of the different ice types that fall within the footprint. Thus, if a beam spot consists of 50% FY ice and 50% MY ice, the measured radiance will fall midway between the mean radiances of FY ice and MY ice. In general, if a small, FY ice feature fills more than half of the beam spot, then it is likely to be classified correctly, because the integrated radiance will be high enough to fall within the range of the correct set of break points.

The antenna beam spot for the validation data set was approximately 100 m at nadir. Thus, features smaller than 50 m are likely to be misclassified by the computer-assisted method used to analyze the Chukchi Sea and Beaufort transect data sets. High-resolution SAR data suggest that neither leads and nor isolated chunks of MY ice of this size are especially common in these regions. We conclude, then, that misclassification of ice caused by the occurrence of small features does not contribute significantly to error in sea ice concentrations derived from KRMS data.

2. Compensating Polar Planimeter: Areas imaged in the Bering Sea and Cape Lisburne mosaics consist predominantly of FY ice; water openings and isolated MY floes constitute only a small fraction of the pack. The area of the few occurrences of open water and old ice in these two data sets was measured using a standard compensating polar planimeter. The instrument was calibrated before use. Error associated with the method was evaluated by repeatedly measuring the area of the same ice floe. Precision was determined to be  $\pm 1\%$ .

### 8.3.2. Results

1. Chukchi Sea: The Chukchi pack in the region imaged in the KRMS mosaic (Figure 8.3) consists of MY floes frozen in a matrix of FY ice. Open water does not occur in the area that was imaged. A series of small leads, frozen with highly emissive FY ice, is present at scattered points along the full length of the mosaic. The relative age of these features, as discerned both from their relationship with respect to adjacent floes and leads and from the high emissivity of ice within them, suggests that they formed recently, probably within days of the overflight.

Both total and MY ice concentrations in SSM/I grid cells were derived from the KRMS Chukchi Sea mosaic using computer-assisted methods described above. A comparison of KRMS concentrations with those retrieved from SSM/I data using the NASA algorithm is presented in Table 8.2. KRMS coverage of SSM/I pixels varies from a minimum of 33% for SSM/I pixel 99-48 to a maximum coverage of 93% for pixel 98-48. For the entire mosaic (all pixels) the mean total ice concentration absolute difference between SSM/I and KRMS is 3%. Differences between the total ice concentrations appear to be independent of KRMS coverage, suggesting that the ice cover in this region is very homogeneous.

The mean absolute difference for MY ice concentration computed from KRMS and SSM/I data for the entire mosaic area is 7.7% (Table 8.2). The standard deviation of these differences for all the pixels is 10.4%. In this case also, there is no clear relationship between the KRMS coverage and the MY ice concentration differences. The difference for the pixel with 93% coverage is 8%, while the smallest absolute difference of 2% is found in pixels with KRMS coverages of 57%, 69%, 33%, and 83%. The largest discrepancy of -19% occurs for pixel 100-51, which has a KRMS pixel

---

\*Although machine discrimination of new ice is not possible on the basis of brightness temperature alone, textural signatures of new ice in passive-microwave images and the context in which new ice occurs (in fractures, leads, and polynyas) permit visual discrimination of new ice from other surface types in most instances.

coverage of 69%. The degree to which the lack of good KRMS coverage (>90%) contributes to these discrepancies cannot be determined without additional surface information.

2. Cape Lisburne: The region imaged in the Cape Lisburne mosaic (Figure 8.2) consists almost exclusively of FY ice, although a few small, isolated MY floes occur at the northern end of the mosaic. Areas of the FY pack close to shore show a poorly developed fracture system. This system consists of newly frozen cracks and narrow leads that generally parallel the shoreline. These features comprise a fraction of a percent of the area imaged in the mosaic; open water and new ice thus do not comprise a significant part of the area imaged.

Sea ice concentrations derived from SSM/I data are compared with concentrations derived from the KRMS for the Cape Lisburne mosaic in Table 8.3. For this region, KRMS coverage is considerably better and varies from a low of 53% to a high of 100% with 4 of the 6 pixels having at least a 90% coverage. The SSM/I total ice concentration values fall below those from the KRMS by 0.2% on average. Areas of new ice associated with the coastal fracture system

Table 8.2. Comparison of Sea Ice Concentrations Calculated From SSM/I Radiances With Corresponding Concentrations Derived From the March 14 KRMS Chukchi Sea Mosaic

SSM/I Cell (Row-Col)	SSM/I		KRMS		KRMS Coverage	SSM/I-KRMS	
	C <sub>MY</sub>	C <sub>TOT</sub>	C <sub>MY</sub>	C <sub>TOT</sub>		C <sub>MY</sub>	C <sub>TOT</sub>
97-47	39	97	37	100	57	2	-3
98-47	43	96	45	100	69	-2	-4
98-48	40	96	32	100	93	8	-4
98-49	46	97	31	100	46	15	-3
99-48	48	97	50	100	33	-2	-3
99-49	45	96	47	100	83	-2	-4
99-50	48	97	63	100	78	-15	-3
100-50	43	97	47	100	39	-4	-3
100-51	53	97	72	100	69	-19	-3
					Mean	-2.1	-3.3
					S.D.	10.4	0.5
					Mean absolute difference	7.7	3.3

Table 8.3. Comparison of Sea Ice Concentrations Calculated From SSM/I Radiances With Corresponding Concentrations Derived From the March 8 KRMS Cape Lisburne Mosaic

SSM/I Cell (Row-Col)	SSM/I		KRMS		KRMS Coverage	SSM/I-KRMS	
	C <sub>MY</sub>	C <sub>TOT</sub>	C <sub>MY</sub>	C <sub>TOT</sub>		C <sub>MY</sub>	C <sub>TOT</sub>
95-38	1	97	0	100	100	1	-3
95-39	0	100	0	100	99	0	0
95-40	10	100 (101)*	1	100	91	9	0
96-39	0	100 (101)*	2	100	53	-2	0
96-40	7	100 (103)*	0	100	94	7	0
96-41	14	100 (104)*	4	100	64	10	0
					Mean	4.2	-0.2
					S.D.	5.1	1.2
					Mean absolute difference	4.8	0.5

\*Algorithm modified to allow concentrations in excess of 100%.

typically were too small to measure accurately from KRMS images; total ice concentrations measured for coastal cells are inflated slightly (less than 1%) as a result. SSM/I sea ice concentrations were measured in excess of 100% (through modification of the SSM/I algorithm), especially for the more northern pixels. This variation is related to the ice surface characteristics which also affect the computed MY ice concentrations as discussed below.

MY ice concentrations were derived from the KRMS mosaic using a polar planimeter. MY ice was present in low concentrations in three of the six grid cells from the KRMS analysis. Larger MY concentrations were obtained in two of the cells from the SSM/I algorithm. For the entire mosaic, the mean SSM/I minus KRMS difference is 4.2%; the standard deviation of the differences is 5.1% (Table 8.3). The mean difference for cells with greater than 90% coverage is 4% with a standard deviation of 4%. Cell 96-41, which includes the greatest concentration of MY ice, may in fact contain more than the 4% that KRMS indicates. This cell is located at the north end of the mosaic and is only partially (64%) imaged by KRMS (Figure 8.2, Table 8.3). MY ice imaged in this cell occurs as floes at the northern limit of KRMS coverage. Portions of the grid cell that were not imaged thus almost certainly include additional MY ice, which, if taken into account, could comprise a higher percentage than indicated by the partial KRMS coverage.

#### 8.4. Discussion

Comparison between ice concentrations derived from the KRMS and those derived from the SSM/I algorithm shows that the SSM/I algorithm does a good job in determining the total ice concentration in both the Chukchi Sea and Cape Lisburne regions (Tables 8.2 and 8.3). In the Cape Lisburne region and coastal regions of the Beaufort Sea where MY ice is absent or present only as a minor constituent (<5%; see Table 8.3), the algorithm overestimates the MY concentration by up to 10%.

Anomalous SSM/I-derived concentrations of MY sea ice in coastal regions of Alaska appear to be related to changes in the radiometric characteristics of FY ice that occur with age. Figure 8.4 shows two KRMS images of FY ice acquired along the same flight track in the Cape Lisburne mosaic. The first, image A, shows relatively young ice close to shore; the second, image B, which includes older presumably FY floes, shows ice farther seaward. The mean 33.6-GHz V-pol. TB of ice in the second image is 5.1 K lower than that in the first. This is associated with higher SSM/I MY ice concentrations in the more northern pixels (see Table 8.3). The three northernmost SSM/I pixels, 95-40, 96-40, and 96-41, have excess concentrations of 9%, 7%, and 10%, respectively.

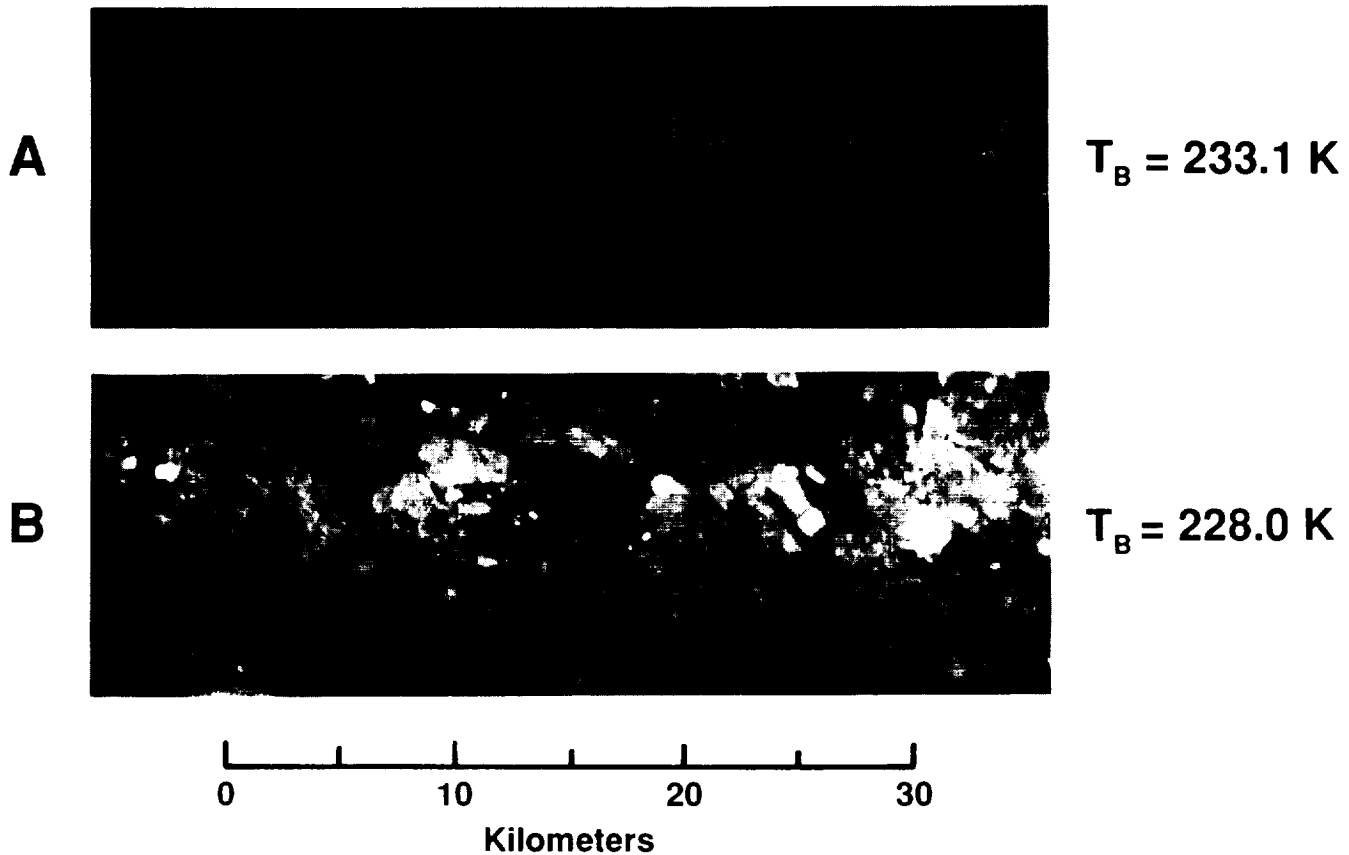
A similar situation occurs in coastal regions of the Beaufort Sea transect where MY ice is not present. Both KRMS data and AMMR data record a drop of 10 K in the TB of FY ice approximately halfway between shore and the first occurrence of MY ice (see Figures 7.4 and 8.5). This drop in TB coincides with a rise in SSM/I MY concentration from less than 10% to approximately 20% (see Figure 7.5). The character of FY ice changes across this boundary in a manner similar to that observed in the Cape Lisburne data. Radiometrically cooler FY ice north of the boundary shows floe structure similar to that observed in cool FY ice in Cape Lisburne images (compare Figure 7.3, B, with Figure 8.4, B). Warmer FY ice south of the boundary lacks well-defined floes, just as warmer ice in the Cape Lisburne region does (compare Figure 7.3, A, with Figure 8.4, A).

We attribute this radiometric difference to differences in the relative age of FY ice in the two scenes, and to variation in scattering properties of snow that this age difference promotes. Volume scattering from snow increases as the snow pack metamorphoses and grain size increases (Ulaby et al., 1986; Hallikainen et al., 1989). Older floes of FY ice thus are likely to appear radiometrically colder than young ice sheets because recrystallization of the snow cover is more advanced, grain size is larger, depth hoar is more common, and microwave energy emanating from underlying ice is scattered more efficiently. Hall (1987) attributes very cold signatures observed in SMMR data over snow-covered regions of northern Alaska to this phenomenon. Snow on young FY ice is likely to scatter less energy because metamorphism is less advanced and grain size is smaller. Additionally, snow covering thin ice sheets is more likely to be wet, highly saline (Takizawa, 1985), and therefore highly emissive. In the absence of significant scatterers, this condition results in higher TBs.

# FIRST-YEAR ICE TYPES

## Cape Lisburne Mosaic

### 8 March 1988



### NORDA KRMS

### 33.6 GHz Passive Microwave Imagery

Figure 8.4. KRMS images showing differences in the character of FY ice in the Cape Lisburne region. Image A shows radiometrically warm FY ice near shore. Image B shows radiometrically cooler FY ice farther northward. Similar differences are observed in FY ice in coastal regions of the Beaufort Sea (see Figure 7.3, A and B).

Applying this interpretation to retrievals from the SSM/I algorithm, anomalous MY concentrations that occur in areas where FY ice predominates indicate the presence of older (and therefore thicker) FY ice (although the sensor actually is measuring differences in snow cover that arise from differences in the physical characteristics of underlying ice related to its age and thickness). This suggests that the algorithm is capable of discriminating between different types of FY ice. Processing SSM/I data with multiple passes of the algorithm, using different sets of global tie-points each pass, might provide additional information concerning the structure of the FY pack.

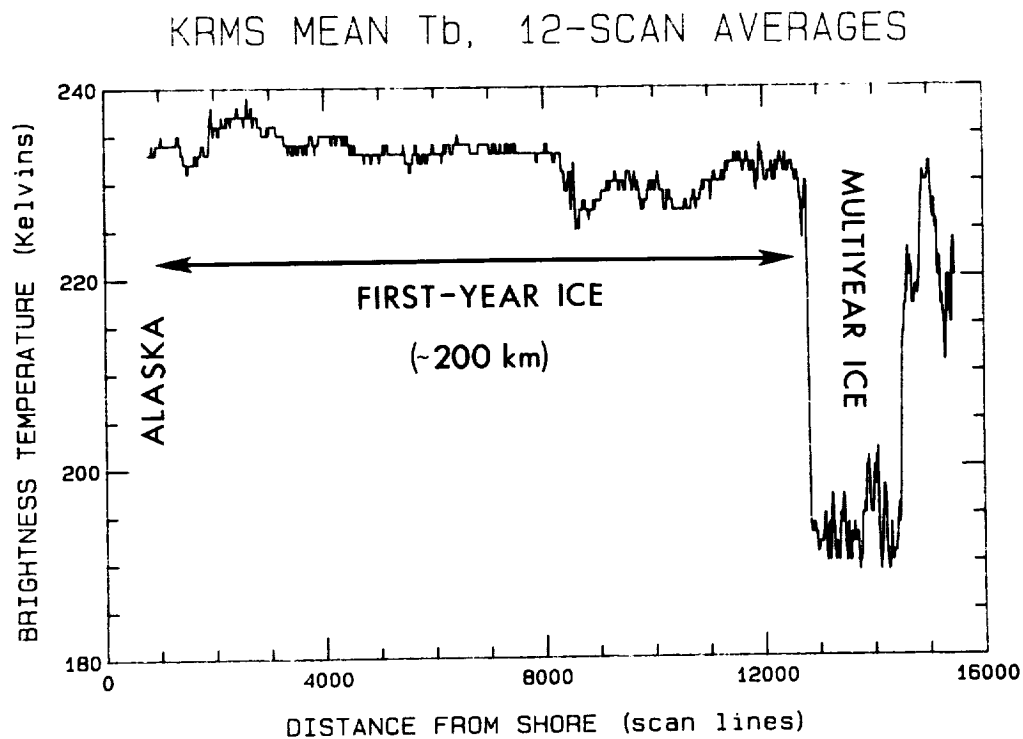


Figure 8.5. KRMS mean TB plotted as a function of distance from the Alaskan coastline from shore to the edge of the MY pack. Note the abrupt decrease in TB at a distance of approximately 8000 scan lines. FY ice shoreward of this point (Figure 7.3, A) is similar in appearance (in KRMS images) to Figure 8.4, A. FY ice packward of this point (Figure 7.3, B) is similar in appearance to Figure 8.4, B.

## 8.5. Conclusions

Comparisons of sea ice concentrations derived with the NASA SSM/I sea ice algorithm with those derived from coincident aircraft passive-microwave imagery are summarized in Tables 8.2 and 8.3 for the Chukchi Sea and Cape Lisburne areas, respectively. Based on these results, the following conclusions are drawn:

1. **Total concentration:** For both the Chukchi and Cape Lisburne mosaics, the SSM/I concentrations compares well with KRMS concentrations. SSM/I determinations were 3% less, on average, than the concentrations as determined by KRMS for the Chukchi mosaic and were 0.5 % less, on average, than KRMS for the Cape Lisburne mosaic.
2. **MY concentration:** For the Chukchi mosaic, the SSM/I average concentration was 2.1% less than that for the KRMS. Differences for individual pixels ranged from -19% to +15%. The variability of the concentrations as determined by KRMS was  $50\% \pm 20\%$ . This large pixel-to-pixel variability indicates that good coverage by KRMS is necessary for a useful comparison. Unfortunately, only one pixel for this region had over 90% coverage. In the Cape Lisburne area, the KRMS indicates that no more than 4% MY ice occurred in any one pixel. The higher SSM/I concentrations are attributed to differences in surface snow characteristics on the older FY ice.

In addition, two types of FY ice are recognized in the KRMS data in coastal regions where FY ice predominates. One is radiometrically warm, lacks indication of floe structure, and typically occurs closest to shore. The other is radiometrically cooler, shows well defined floe structure, typically occurs seaward of the first type, and is presumably

thicker and older. The SSM/I algorithm, which now produces erroneous MY concentrations in FY ice regions, appears to be sensitive to these differences and probably could be modified to map the extent of these two types of FY ice.

## 8.6. References

- Eppler, D. T., L. D. Farmer, A. W. Lohanick, and M. C. Hoover, Digital analysis of passive Ka-band microwave images for sea ice classification, *NORDA Technical Report 51*, Naval Ocean Research and Development Activity, Stennis Space Center, MS, 54 pp., 1984.
- Eppler, D. T., L. D. Farmer, A. W. Lohanick, and M. C. Hoover, Classification of sea ice types with single-band (33.6 GHz) airborne passive microwave imagery, *J. Geophys. Res.*, 91, n.C9, 10661-10695, 1986.
- Eppler, D. T., and B. M. Heydlauff, Digitizing KRMS analog data on a personal computer, *NORDA Technical Report 219*, Naval Ocean Research and Development Activity, Stennis Space Center, MS, 60 pp., 1991.
- Farmer, L. D., D. T. Eppler, B. M. Heydlauff, and D. Olsen, KRMS SSM/I validation March 1988 quick look report, *NORDA Technical Note 385*, Naval Ocean Research and Development Activity, Stennis Space Center, MS, 43 p., 1989.
- Farmer, L. D., D. T. Eppler, and A. W. Lohanick, 1989b, Converting digital KRMS values to Kelvin units of brightness temperature, *NORDA Technical Note 427*, Naval Ocean Research and Development Activity, Stennis Space Center, MS, 16 pp., 1990.
- Hall, D. K., Influence of depth hoar on microwave emission from snow in northern Alaska, *Cold Regions Science and Technology*, 13, 225-231, 1987.
- Hallikainen, M., V. Jaaskelainen, and J. Talvela, Results from ground-based radiometry of snow, *Proceedings of IGARSS'89*, 3, 1231-1234, 1989.
- Heydlauff, B. M., and J. B. Seybold, Cross-track correction circuit (Navy Technical Catalog No. 1723; Navy Case No. 66637), *Navy Technical Disclosure Bulletin*, 9, n.2 December 1983, 43-51, 1983.
- Takizawa, T, Salination of snow on sea ice and formation of snow ice, *Annals of Glaciology*, 6, 309-310, 1985.
- Ulaby, F. T., R. K. Moore, and A. K. Fung, *Microwave Remote Sensing — Active and Passive (3 Volumes)*: Addison Wesley Publishing Company, Reading, Massachusetts, 1986.



## Chapter 9

### SSM/I AIRCRAFT UNDERFLIGHTS: SSM/I-NADC/ERIM SAR Comparison

Robert R. Jentz, Chris C. Wackerman, Robert Shuchman,  
Robert G. Onstott and Andrew Milman  
Environmental Institute of Michigan  
Ann Arbor, Michigan 48107

9.1 Introduction .....	81
9.2 NADC/ERIM SAR Instrument and Mission Description .....	81
9.3 SSM/I-SAR Comparison .....	84
9.4 Discussion .....	87
9.5 Conclusions .....	88
9.6 References .....	89

#### 9.1. Introduction

This chapter presents comparisons of sea ice concentration estimates produced from high-resolution SAR imagery obtained with the SAR system developed by the Environmental Research Institute of Michigan (ERIM) in cooperation with the Naval Air Development Center (NADC) with ice concentrations derived from the multi-channel SSM/I radiances using the NASA Team algorithm (see Chapter 4).

High-resolution aircraft SAR systems have been shown to provide reliable ice concentration estimates (Burns et al., 1985 and 1987). These studies show that the high spatial resolution (approximately 3 m square pixels) associated with SAR imagery provides the ability to delineate individual floes and leads, which makes the determination of ice concentration easier. It has also been shown that sea ice-concentration estimates generated from both passive- and active-microwave sensors over coincident scenes do produce similar results using a single channel linear concentration algorithm (Burns et al., 1987, and Martin et al., 1987). However, the analysis described in this chapter will use sea ice-concentration estimates from high-resolution SAR imagery (where there are approximately 300 million SAR pixels corresponding to each SSM/I pixel) to validate the SSM/I MY ice concentrations. The SAR-derived ice concentration estimates are produced by a manual analysis of mosaicked imagery obtained from data gathered during the March 1988 NASA and Navy SSM/I underflights described previously in Chapter 7.

This chapter is separated into four sections. Section 9.2 provides a description of the SAR system that collected the digital imagery used in this analysis, along with a brief synopsis of the Alaska data collection. A comparison of the SSM/I-SAR sea ice concentrations is presented in Section 9.3. A discussion of the results is presented in Section 9.4 and conclusions are given in Section 9.5.

#### 9.2. NADC/ERIM SAR Instrument and Mission Description

##### 9.2.1. SAR System Description

The NADC/ERIM SAR is a multifrequency, polarimetric SAR installed in a U.S. Navy P-3 aircraft. It is a side-looking SAR that operates in strip-map mode, and is capable of looking out either side of the aircraft. The center frequencies are 9.35 GHz, 5.30 GHz, and 1.25 GHz, corresponding to X, C, and L bands, respectively. The system is capable of recording polarimetric data corresponding to all of the elements of the polarization matrix (i.e., HH, VV, HV, and VH polarizations) where transmit and receive polarizations can be altered on a pulse-by-pulse basis. High-density digital tape (HDDT) is the primary storage medium for the digital data that is collected from each of the four channels.

A block of auxiliary data describing the radar flight path and geometry are also recorded for each pulse and stored with the digital data on HDDT. The data from a single channel, selectable by the users, are also recorded on a real-time image formation processor, along with photographic film, which is used for subsequent optical processing.

The SAR operates in five different swath modes with varying combinations of frequency/polarization. In single-swath-multiplex mode the system collects any four frequency/polarization combinations with each of the four channels containing the same range coverage. The azimuth data are presumed to a rate one-sixth the no-presum rate, and 4096 range bins are recorded per channel. The single-swath-polarimetric mode is similar to the single-swath-multiplex mode with the same range coverage in each of the four channels, hence, the same number of range bins. A single frequency band is used with all four polarization combinations where a constant phase shift, of the transmitted FM chirp, is maintained between the four polarizations. The azimuth records are presumed to one-third the no-presum rate. The single-swath mode also contains a no-presum mode, which records a single frequency band and polarization. The double-swath-multiplex mode records two channels of data with varying combinations of frequency/polarization. The range swath is doubled, so the number of range bins recorded is 8192 and the presum rate is one-sixth the no-presum rate. The quadruple-swath-multiplex mode records one channel of data corresponding to a single frequency band and polarization. The range swath is increased by four over the single-swath mode so that 16384 range bins can be recorded, and the presum rate remains at one-sixth the no-presum rate.

The SAR operates in one of two resolution modes for any of the swath modes previously described. The slant range coverage at high resolution is 4915 m in single-swath, 9830 m in double-swath, and 19660 m in quadruple-swath modes, with azimuth and range resolution being 2.8 m and 1.6 m, respectively. At low resolution, the slant range coverage is 9830 m in single-swath, 19660 m in double-swath, and 39320 m in quadruple-swath modes, with an azimuth resolution of 2.8 m and a range resolution of 3.2 m. An in-depth description of the SAR is given by Kozma et al. (1986).

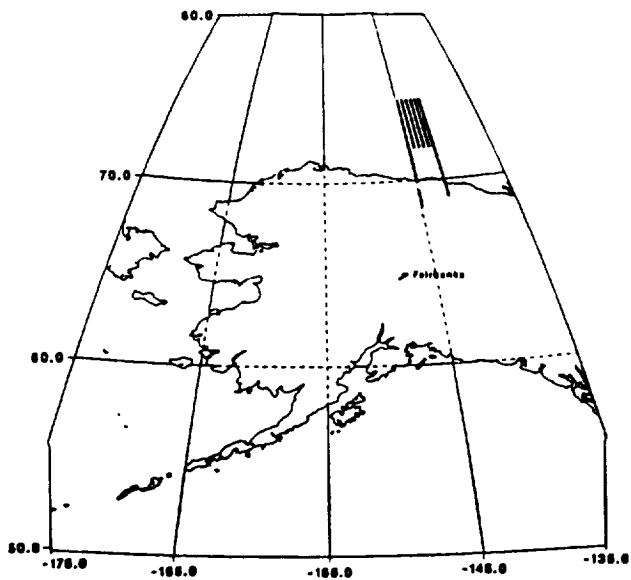
### 9.2.2. Alaska Mission Description

The Alaska survey consisted of data collections on four separate days in and around the Alaskan mainland. Ice data were collected in the Beaufort Sea on the 18th and 19th of March 1988, in the Bering Strait on the 21st of March 1988, and in the Chukchi Sea on the 22nd of March 1988. A diagram indicating these locations can be seen, along with the Alaskan coastline, in Figure 9.1. Figure 9.1 also illustrates the flight-track locations of the SAR for each mission of the Alaska survey during which the sensor was recording data. Notice that on the 18th and 19th of March, the sensor was recording imagery across the northern Alaska coastline at both the first and last pass of each mission. This gives well-known reference points for determining the exact locations of the P-3/SAR data. The Konganevik point, located at 70° 5.12'N latitude and 145° 9.9'W longitude in the Camden Bay, was used as a reference point for the imagery gathered on the 18th of March. This reference point is located at the end of the last pass of data gathered on this day; therefore, any error in the internal navigation system (INS) should be greatest at this point. This reference point revealed a discrepancy in the SAR's swath location of 3.5 nm in longitude and 6.2 nm in latitude, which is well within the SSM/I footprint. The mean drift of the aircraft was computed as the total aircraft drift divided by the flight time to the reference point giving 0.93 knots, which is well within the expected mean drift for this internal navigation system.

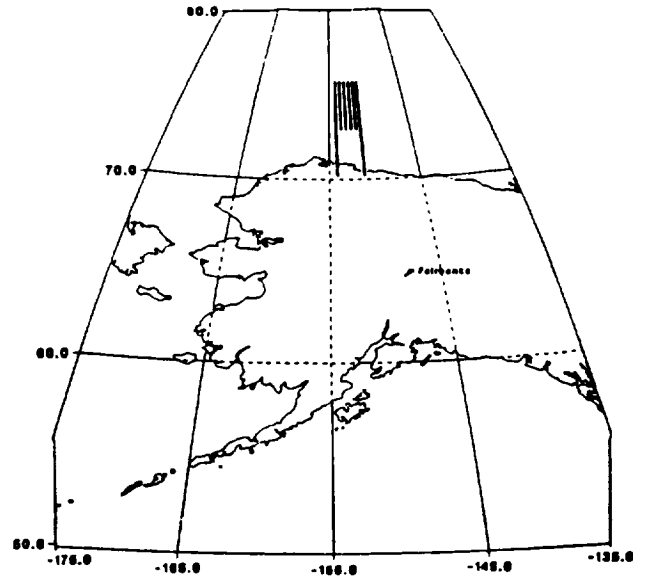
The SAR data were collected in double-swath-multiplex mode at low resolution (approximately 3 meters in both range and azimuth). The two frequency and polarization combinations used consisted of X-band at HH-polarization, and C-band at VV-polarization. The aircraft flew at an altitude of 6098 m, with a mean velocity of 288 knots. The slant range distance to the near edge of the radar swath was 7267 m, which corresponds to an incidence angle of 33°, and the slant range distance to the far edge of the radar swath was 26923 m corresponding to an incidence angle of 77°. This provides 22.270 km of uninterrupted image coverage in the ground plane. The flight lines were planned to provide approximately 3 km of overlap between adjacent passes. This overlap was more than adequate to ensure no gaps in the data coverage, even with navigation errors. Aircraft flight times are presented in both Table 9.1 and ERIM Report No. 202800 (Gineris et al., 1989).

# ALASKA SURVEY

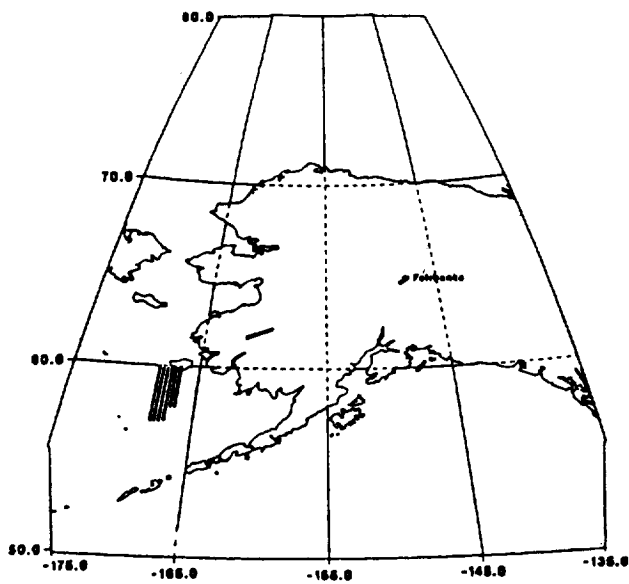
March 18, 1988



March 19, 1988



March 21, 1988



March 22, 1988

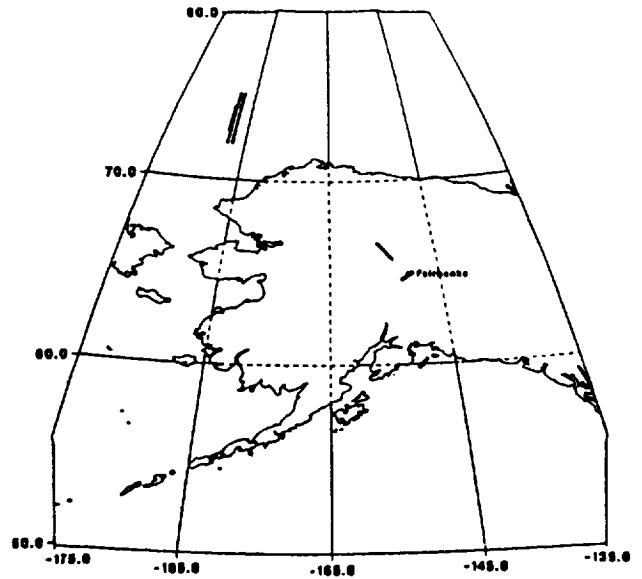


Figure 9.1. March 1988 Beaufort Sea data collection locations with the NADC P-3.

Table 9.1. March 1988 SAR Alaska Collection Flight Times

Flight Date (Local)	Start Time (UT)	Stop Time (UT)	Altitude (ft)	Average Speed (kts)
18 March 1988	02:35:06	10:16:58	20,000	221
19 March 1988	02:59:57	10:27:52	20,000	287
21 March 1988	03:03:34	09:52:51	20,000	293
22 March 1988	04:17:33	11:06:09	20,000	301

### 9.3. SSM/I-SAR Comparison

The SAR sea ice data collected on both the 18th and 19th of March 1988 were used to validate the MY ice-concentration estimates generated from the SSM/I overflights. The SAR ice-concentration estimates were derived manually from a SAR photographic mosaic. The mosaic was produced by optically processing the digital SAR data collected at C-band (5.3 GHz) VV-polarization. Figure 9.2 shows the photographic mosaic for the SAR data collected on the 18th of March after correcting for the location error described in Section 9.2.2, along with boxes representing the SSM/I grid cells. Notice that this mosaic contains the FY/MY ice edge, which covers a wide range of MY ice concentrations. This allows us to analyze the SSM/I produced ice-concentration estimates at the lower extreme values (i.e., no MY ice) as well as the high. Figure 9.3 shows the corrected SAR mosaic for the 19th of March data, again with the SSM/I grid cells. This mosaic shows both FY and MY ice located farther into the MY pack than the mosaic illustrated in Figure 9.2. Here, the mosaic contains a relatively uniform distribution of MY ice.

Each of the SSM/I cells shown in Figures 9.2 and 9.3 represents a 50- by 50-km area on the ground. The SAR MY ice concentration estimates were derived from averaging 400 manually interpreted concentration estimates, each covering a 2.5- by 2.5-km<sup>2</sup> area on the ground. The SAR estimates were produced by dividing each of the 50-km SSM/I cells into a 20 X 20 grid. Each of the 2.5- by 2.5-km areas within the SSM/I cell was analyzed to determine the percentage of MY sea ice. For those SSM/I cells that cross the SAR mosaic boundary (i.e., areas 3 and 10 of Figure 9.2; areas 3, 4, and 9 of Figure 9.3), the SAR MY concentration estimate reflects the average of only the 2.5-km areas within the mosaic boundary. Therefore, the MY ice-concentration estimates of these areas represent only the SSM/I cell area with coincident SAR coverage. These estimates can be compared to the SSM/I estimates only after making the assumption that the partial areas outside the SAR mosaic boundary have MY concentrations consistent with the area within the SAR boundary.

Table 9.2 shows the MY ice-concentration estimates from the SAR and SSM/I sensors on both the 18th and 19th of March 1988. These estimates correspond to the ten coincident areas depicted on each of the mosaics in Figures 9.2 and 9.3. Notice that the concentration estimates generated from the 19th data are within 15%, while much larger errors exist for the 18th. Possible causes for the poor concentration estimates generated from the SSM/I data will be discussed in the next section. The SAR MY ice-concentration estimates shown are averages of four separate manual interpretations by four different individuals and are believed to be precise to within  $\pm 5\%$  (this precision was verified by an analysis of digital SAR data). This table also contains the percent of SAR coverage for each of the ten coincident areas along with the difference in concentration between the two sensors. This difference is computed as the SSM/I concentration minus the SAR estimate. The data in Table 9.2 show that the difference in MY ice concentration is positive for each coincident area. Also, the magnitude between the errors for both the 18th of March (where the imagery crosses the FY/MY ice edge) and the 19th of March (where the imagery represents an area farther into the MY ice pack) is different, being much larger for the 18th. These SAR ice-concentration estimates are plotted against the SSM/I estimates for both data sets in Figures 9.4 and 9.5. A linear regression was performed on the concentration estimates from both data sets, and the results are presented in Table 9.3. The slopes of the linear regression are 0.69 and 0.79, with Y-intercepts of 33.16 and 18.27 for the concentration estimates from the 18th and 19th of March, respectively. Since the correlation coefficient is relatively high for the 18th of March data set, we must believe that the fitted line does represent the linear trend in the concentration

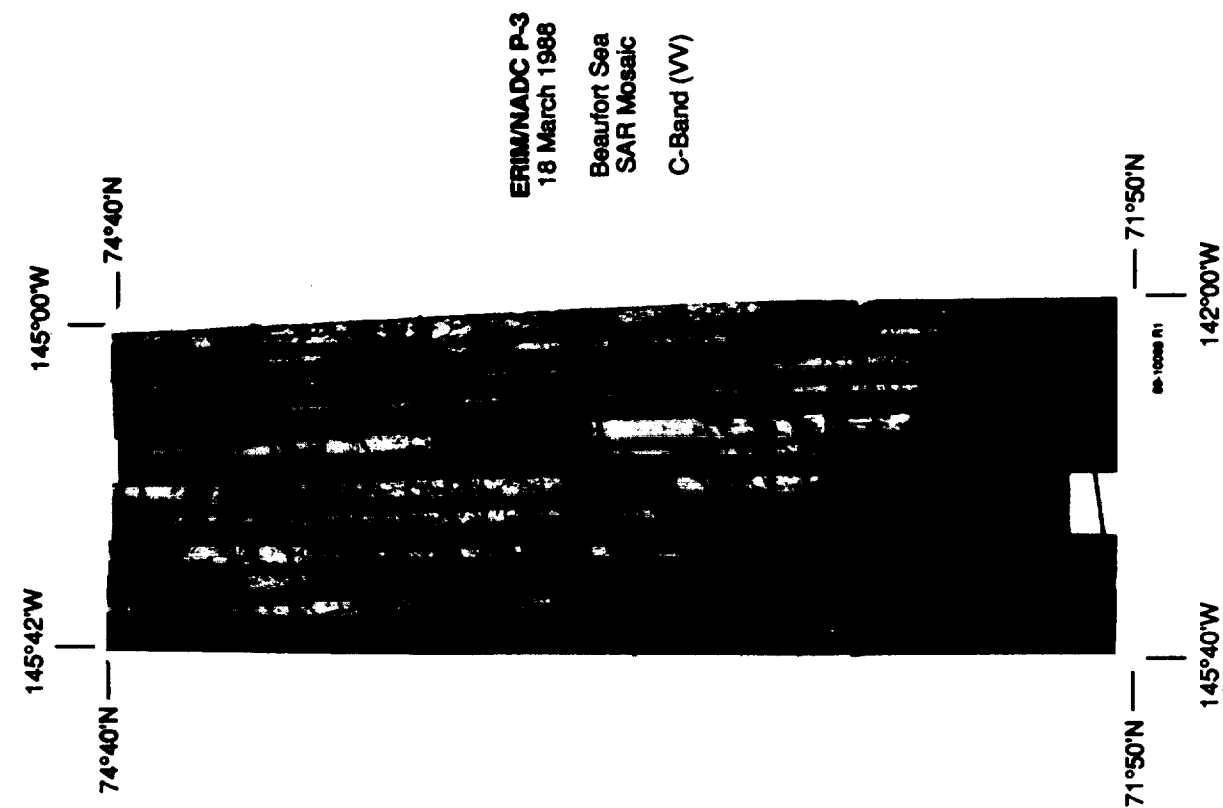


Figure 9.2. Photographic mosaic of digital SAR data collected in the Beaufort Sea on 18 March 1988. The mosaic shows the FY/MY ice transition.

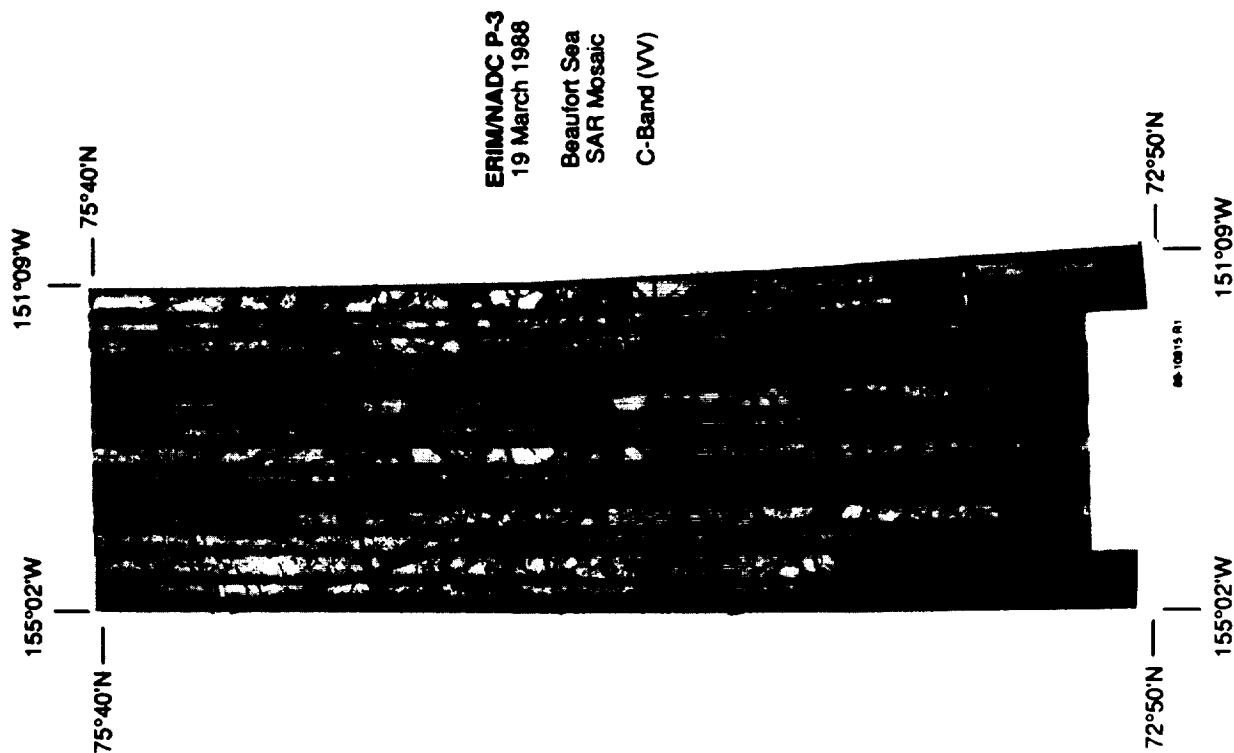


Figure 9.3. Photographic mosaic of digital SAR data collected in the Beaufort Sea on 19 March 1988. The mosaic shows an area of mixed FY and MY sea ice located in the MY ice pack.

estimates. This is unfortunate, because if these concentration estimates were actually similar in value, they would be expected to propagate around a line with a slope of 1.0 and a Y-intercept of 0.0. It should be pointed out that the linear trend shown in Figure 9.5 representing the 19th of March data set might not represent the actual trend in the data, since the range of concentrations, clustered about 55%, is relatively small. Therefore, this analysis will concentrate on the results generated from the 18th of March data. Figures 9.6 and 9.7 show the SSM/I-SAR MY ice concentration errors plotted against the SAR MY estimates for both the 18th and 19th of March data, respectively. Results of the linear regression through these data are given in Table 9.4.

Table 9.2. SAR-SSM/I Multiyear Ice-Concentration Estimates Derived From 50 km Areas of Data Gathered During the March 1988 Alaska Survey

March 18, 1988					March 19, 1988			
Area	SAR Coverage (%)	SAR (%)	SSMI (%)	Dif (%)	SAR Coverage (%)	SAR (%)	SSMI (%)	Dif (%)
1	100	0	37	37	100	58	64	6
2	100	6	41	35	100	55	62	7
3	80	27	57	30	80	57	58	1
4	100	6	28	22	82	52	66	14
5	100	48	50	2	100	52	55	3
6	100	48	66	18	100	49	57	8
7	100	40	62	22	100	57	68	11
8	100	56	78	22	100	72	74	2
9	100	47	69	22	91	56	60	4
10	66	55	74	19	100	64	73	9

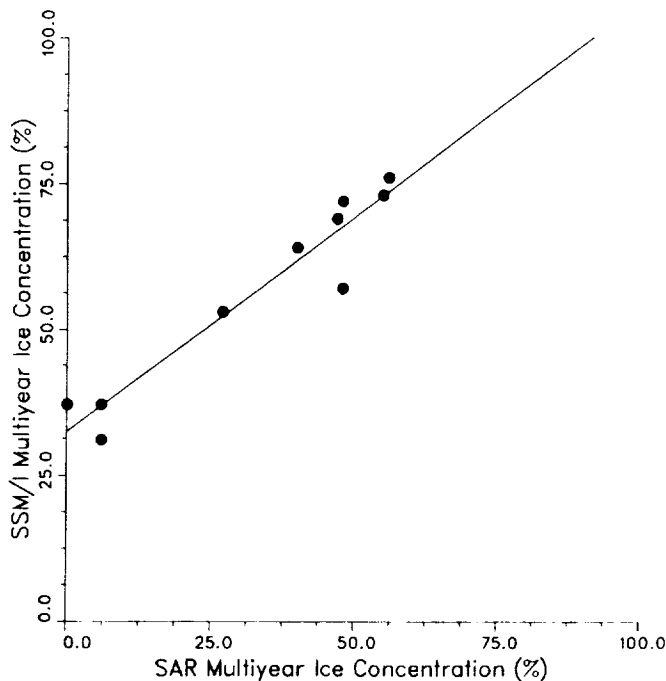


Figure 9.4. Plot of SAR and SSM/I MY ice concentrations for March 18, 1988.

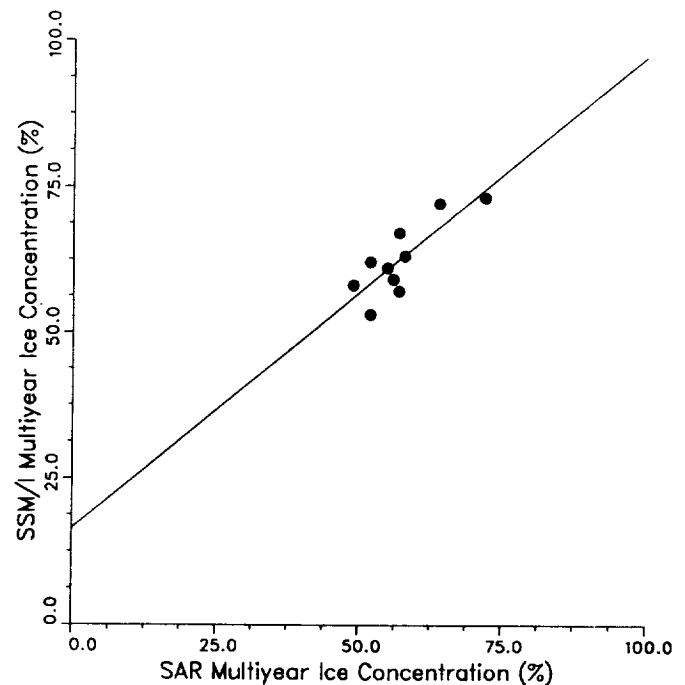


Figure 9.5. Plot of SAR and SSM/I MY ice concentrations for March 19, 1988.

Table 9.3. Linear Regression Parameters for the Plots in Figures 9-4 and 9-5

Collection Data	Slope	Y-Intercept	Correlation Coefficient	MSE
18 March 1988	0.691	33.167	0.903	46.709
19 March 1988	0.794	18.271	0.802	13.783

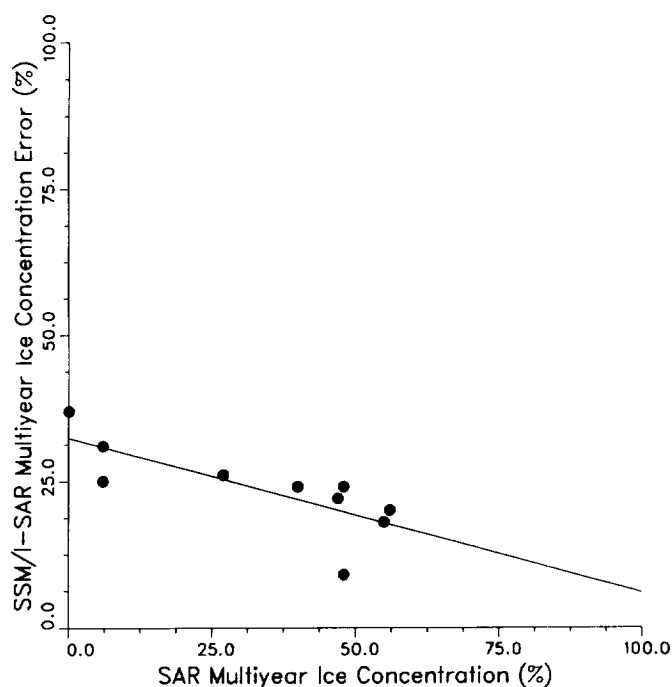


Figure 9.6. MY ice concentration difference (SSM/I minus SAR) versus SAR estimate for the 18 March 1988 Beaufort Sea data.

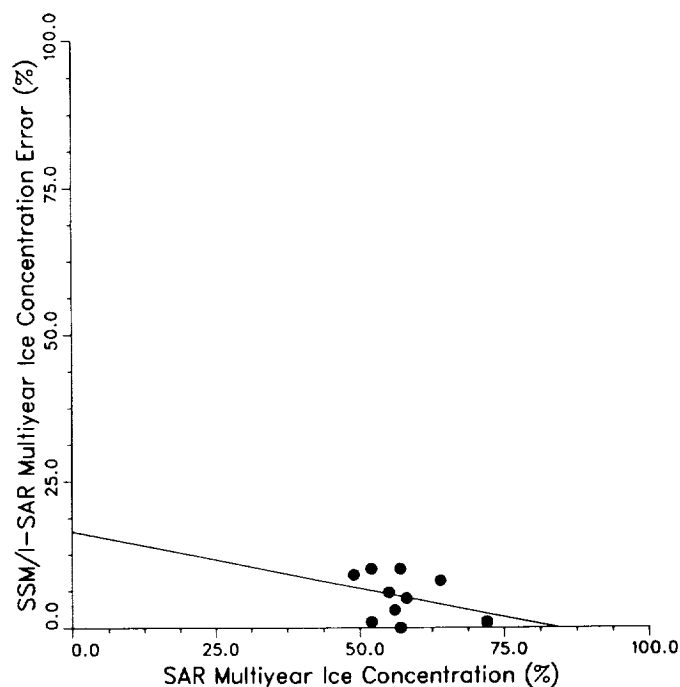


Figure 9.7. MY ice concentration difference (SSM/I minus SAR) versus SAR estimate for the 19 March 1988 Beaufort Sea data.

Table 9.4. Linear Regression Parameters for the Plots in Figures 9-6 and 9-7

Collection Data	Slope	Y-Intercept	Correlation Coefficient	MSE
18 March 1988	-0.308	33.167	-0.672	46.709
19 March 1988	-0.206	18.271	-0.328	13.783

#### 9.4. Discussion

It is quite obvious from the results presented in Section 9.3 that the March 18 SSM/I MY ice-concentrations do not agree well with the corresponding SAR estimates. These differences may result from one or both of two sources of error. These sources of error are: (1) an alignment error between the coincident SAR and SSM/I pixel locations and (2) FY ice pressure ridges which are misclassified as MY ice by the SSM/I algorithm. This hypothesis is based on the assumption that the SAR estimates are accurate to within  $\pm 5\%$  (Section 9.3).

Since the surface area imaged contains only FY and MY ice types, Figure 9.6 and the corresponding regression

parameters in Table 9.4 imply that 30% of the SSM/I MY concentration estimate is caused by the FY ice in the image. If we believe the second part of the hypothesis, then the plot in Figure 9.6 implies that 30% of the MY concentration estimate is caused by the TBs produced from the pressure ridges contained within the FY ice. A simple test was performed on the digital SAR data to determine if these ridge lines could, in fact, constitute 30% of the energy within a given area of FY ice. This test is based on the fact that the total energy received by the SSM/I sensor is the sum of energy returned from both the MY and FY ice in the scene and can be modeled as follows:

$$E_t = pE_{my} + (1 - p)E_{fy} \quad (9.1)$$

where  $E_t$  represents the total energy received by the SSM/I sensor,  $E_{my}$  is the received energy from the MY ice in the scene,  $E_{fy}$  is the received energy from the FY ice in the scene, and  $p$  is the percentage of the received energy classified as MY ice by the SSM/I sensor. The energy associated with FY ice pressure ridges is accounted for as follows:

$$E_{fy} = E_{r1} + E_{ftr} \quad (9.2)$$

where  $E_{r1}$  is the received energy caused by the pressure ridges and  $E_{ftr}$  is the received energy caused by the FY ice without pressure ridges. When the SSM/I sensor is viewing an area containing only FY ice (i.e., Area 1 on the March 18 mosaic where the SAR MY ice estimate is 0% and the SSM/I estimate is 37%), Equations 9.1 and 9.2 will be equal, giving

$$E_t = E_{fy} \Rightarrow p^1 E_{my} + (1 - p^1) E_{fy} = E_{r1} + E_{ftr} \quad (9.3)$$

where  $p^1$ , the percentage of received energy (caused by the pressure ridges in the FY ice) being misclassified as MY ice by the SSM/I sensor, is given as

$$p^1 = E_{r1} / (E_{my} - E_{ftr}) = (E_{ftr} - E_{ftr}) / (E_{my} - E_{ftr}) \quad (9.4)$$

where  $E_{ftr}$  is the energy received from an area of FY ice with pressure ridges. The presence of pressure ridges throughout the FY ice region made finding an adequate area of FY ice without ridges very difficult. Therefore, the energy (measured as the SAR intensity return) associated with an area of FY ice without pressure ridges was determined by thresholding an area of FY ice to remove the pressure ridges. A visual inspection of the digital SAR image was used to determine the appropriate threshold location that would separate the pressure ridges from the FY ice. Substituting the calculated values for  $E_{ftr}$ ,  $E_{ftr}$ , and  $E_{my}$  into Equation 9.4 generated a  $p^1$  value of 0.27, indicating that 27% of the FY energy is produced from the pressure ridge lines.

Another possible explanation for the difference in MY ice-concentration estimates for the 18th of March data would be an accumulated error in the locations of the SAR and SSM/I footprints. The concentration estimates generated from the 19th of March data do not show this large an error (mean difference of 5.3%). However, this data is located farther into the MY ice pack, where a relatively uniform distribution of both FY and MY ice exist. Therefore, location errors would not have as severe an effect as in the area crossing the FY/MY ice edge. The mosaic representing the 18th of March data, illustrated in Figure 9.2, shows a monotonically increasing amount of MY ice with increasing latitude. This information was used to determine a possible shift in the SSM/I pixel locations, which brought the mean difference between the concentration estimates down to 9% from 23%. This shift corresponds to approximately 1°N in latitude and 1°E in longitude. Thus, for location errors to be the cause of the ice concentration errors, they would have to be on the order of 60 nm.

## 9.5. Conclusions

The MY ice-concentration estimates produced from the NASA Team algorithm discussed in Chapter 4 do not agree with MY estimates generated by a manual interpretation of the optically processed digital SAR data gathered on the 18th of March. However, the concentration estimates generated from the 19th of March data are similar (5.3±3.9%).

Assuming that the SAR estimates are correct, a possible explanation for this disagreement includes (1) an alignment error in the pixel locations between both the SAR and SSM/I sensors and (2) the fact that pressure ridges associated with FY ice are being misclassified by the SSM/I sensor. The 19th of March data is located farther into the MY ice pack, where a relatively uniform amount of MY sea ice exists at higher concentration levels than on the FY/MY ice edge. Therefore, concentration errors caused by either pressure ridges or pixel location would not be as severe as for the 18th of March data, which crosses the FY/MY ice edge. The backscatter energy produced by the pressure ridges in the digital SAR data closely correspond to the 30% error seen in the 18th of March concentration results. Also, a 1° error in the SSM/I pixel locations seems to account for the discrepancy in the concentration results for the 18th of March data. As mentioned previously, the location error associated with the SAR system is 6.2 nm in latitude and 3.5 nm in longitude, corresponding to a mean drift of 0.93 knots. This error by itself is negligible in terms of its effect on the MY ice concentration estimates, but by adding a possible 10-km location error associated with the SSM/I system, a small difference in concentration estimates would be expected. However, the combined location error between both sensors is still much smaller than the 1° shift described in Section 9.4.

## 9.6. References

- Burns, B. A., D. J. Cavalieri, M. R. Keller, W. J. Campbell, T. C. Grenfell, G. A. Maykut, and P. Gloersen, "Multisensor Comparison of Ice Concentration Estimates in the Marginal Ice Zone," *J. Geophys. Res.*, 92, 6843-6856, 1987.
- Burns, B. A., R. R. Jentz, C. G. Caruthers, J. D. Lyden, and P. L. Jackson, "Computer-assisted techniques for geophysical analysis of SAR sea-ice imagery," *Proceedings of the Nineteenth International Symposium on Remote Sensing of the Environment*, Environmental Research Institute of Michigan, Ann Arbor, Mich., pp. 947-959, 1985.
- Gineris, D., R. Shuchman, J. Lyden, A. Milman, E. Kasischke, *Environmental Research Institute of Michigan Informal Informational Report No. 202800-1-T*, Advanced Concepts Division, January 1989.
- Kozma, A., A. Nichols, R. Rawson, R. Shackman, C. Haney, and J. Schanne Jr., "Multifrequency-Polarimetric SAR for Remote Sensing," *Proceedings of the IEEE Geoscience and Remote Sensing Society*, 8-11, pp. 715-719, September 1986.
- Martin, S., B. Holt, D. J. Cavalieri, and V. Squire, "Shuttle Imaging Radar B (SIR-B) Weddell Sea Ice Observations: A Comparison of SIR-B and Scanning Multichannel Microwave Radiometer Ice Concentrations," *J. Geophys. Res.*, 92, 7173-7179, 1987.



## Chapter 10

### SUMMARY, CONCLUSIONS, AND RECOMMENDATIONS

Donald J. Cavalieri  
Laboratory for Hydrospheric Processes  
NASA Goddard Space Flight Center  
Greenbelt, Maryland 20771

10.1 Summary and Conclusions .....	91
10.2 Recommendations .....	94
10.3 References .....	95

#### 10.1 Summary and Conclusions

The launch of the first DMSP SSM/I in June 1987 has provided the polar research community with a new passive microwave imager with which to study polar ocean processes. As an operational sensor, the SSM/I series will continue to provide data well into the 1990's and beyond (Hollinger et al., 1989), thereby extending the time series of sea ice observations that started with the launch of the Nimbus 5 ESMR in December 1972 and continued until August 1987 with the Nimbus 7 SMMR. Thus, the SSM/I is expected to contribute significantly to the data base needed to study global climate change.

A key requirement for obtaining scientifically useful geophysical measurements from any instrument is knowing both the precision and accuracy of the data obtained from that instrument. To this end, much credit is due Jim Hollinger and his SSM/I Team at NRL. Except for the 85-GHz channels, the SSM/I noise equivalent temperature differential, a measure of sensor precision, was found to be quite stable over the first 2 years of operation, and the absolute accuracy of the calibrated TBs was found to be within  $\pm 3$  K (Hollinger et al., 1989). The greatest concern to users of the data was the large geolocation errors that were discovered shortly after launch. For the purpose of reducing these errors in as short a time as possible, Cal Swift and Mike Goodberlet, members of the NASA Team, developed an empirical procedure for correcting about half of the observed 20-km to 30-km geolocation error (see Chapter 2), thus bringing the geolocation uncertainty into the 10- to 15-km range. Further work by the NRL team promises to reduce this uncertainty below the 10-km level.

Early development of the SSM/I processing software for NASA by NODS at JPL and the transfer of this software to NSIDC for subsequent processing, archival, and distribution of the gridded SSM/I radiances ensures the ready access of these data to the research community. At this writing, 2.5 years of SSM/I gridded TB data on CD-ROMS have been distributed to the user community by NSIDC.

The main objective of NASA's Sea Ice Validation Program was to provide the research community with a measure of the accuracy of the sea ice concentrations derived from the SSM/I calibrated radiances with the NASA Team algorithm. The following discussion summarizes the results presented in the previous chapters and provides an estimate of the accuracy for each sea ice parameter. Summary statistics of the sea ice parameters are provided in Table 10.1.

**Sea Ice Edge:** Aircraft flights across the Bering Sea ice edge provided data to determine the best SSM/I sea ice-concentration contour to use for accurately mapping the location of the ice edge. On average, the SSM/I ice concentration for the SSM/I 25-km map grid containing the initial seaward ice band is 15%. The concentration corresponding to the position of the main pack is 38%. The importance of this result is that it supports the use of the SSM/I 15% ice-concentration contour as the definition of the location of the ice edge, the convention used previously in the analysis of sea ice data sets from satellite microwave radiometers. These results also suggest that the use of the GR weather filter,

which eliminates ice concentrations of less than 15% on SSM/I grid maps, really eliminates only the spurious ice concentrations associated with the smearing of the ice edge by the finite width of the SSM/I antenna pattern.

Table 10.1. Summary Results From the DMSP SSM/I Sea Ice Validation

Sea Ice Parameter:

Ice-edge location (AMMR/SSMI):	15% SSM/I concentration contour is within 25 km of initial ice band; 38% concentration is within 25 km of main ice pack.	
Total sea ice concentration	<u>Global TP</u>	<u>Local TP</u>
Landsat/SSMI:		
All Winter Cases:	Mean -3.6%	-1.5%
	S.D. 6.6%	4.5%
Aircraft/SSMI:		
All March data:	Mean -2.4%	
	S.D. 2.4%	
Multiyear sea ice concentration		
Aircraft/SSMI:		
All March data:	Mean +12.0%	
	S.D. 11.0%	
w/o March 18 data:	Mean +2.8%	
	S.D. 8.1%	

**Total Sea Ice Concentration:** The Landsat MSS-SSM/I ice-concentration comparisons provided a full range of cases covering different regions and different seasons. Except for the summer results, which were in error because of ice drift (see Chapter 5), the mean difference for all spring and fall cases was -3.6% with a standard deviation of 6.6%. There are two important results from the Landsat MSS intercomparisons. First is that with the global set of tie-points, the overall accuracy under winter conditions is 7% with a mean bias of -4%, indicating that the SSM/I underestimates ice concentration relative to Landsat. Second, the use of local and seasonal tie-points improves the accuracy by reducing the standard deviation of the observed differences for all but the summer cases (Table 10.1). While the global set of algorithm tie-points results in a lower accuracy because of interregional variability of the microwave signatures of sea ice, it does provide a coherent picture of the hemispheric ice cover and its temporal variability needed for monitoring climate change.

The results from the aircraft-SSM/I comparisons for total ice concentration are consistent with the Landsat results obtained with the global set of algorithm tie-points. The mean difference between aircraft concentrations (consistently 100%) and those calculated from the SSM/I radiances is  $-2.4\% \pm 2.4\%$ , while the results obtained from the March 1988 Landsat-SSM/I comparisons are  $-2.1\% \pm 3.1\%$  for the same region. Results from Chapters 8 and 9 show that the SSM/I ice concentrations for individual pixels range from a minimum of 95% to a maximum of 100%. This range of variability falls within two standard deviations (6.2%) as determined by the Landsat analysis. Based on the Landsat

comparisons for different regions during fall, winter, and spring, the one standard deviation measure of the SSM/I ice concentration accuracy using the global set of tie-points is  $\pm 6.6\%$  (Table 10.1). Locally, the accuracy may be much better, as indicated by the regional Landsat and aircraft results.

**Multiyear Sea Ice Concentration:** High-resolution microwave images obtained from the SSM/I underflights were used for validating the SSM/I MY ice concentrations. A summary of the statistics from the comparison between the SSM/I concentrations and those derived from the Beaufort and Chukchi sea aircraft mosaics is also given in Table 10.1. A comparison of these data (Figure 10.1) shows that for 3 of the 4 days, the agreement between the SSM/I and aircraft concentrations is fairly good. The reason for the large bias in the March 18 data is uncertain at this time; thus, we have no basis for deleting the data. Using all the data, the linear correlation coefficient is 0.86 and the standard error of estimate is 12.0%; without the March 18 data, the correlation increases to 0.94 and the standard error decreases to 8.1%. The mean difference with all the data is 8.5%, and the standard deviation of the differences is 12.5%. Without the March 18 data, the mean difference drops to 2.8% and the standard deviation to 8.1%.

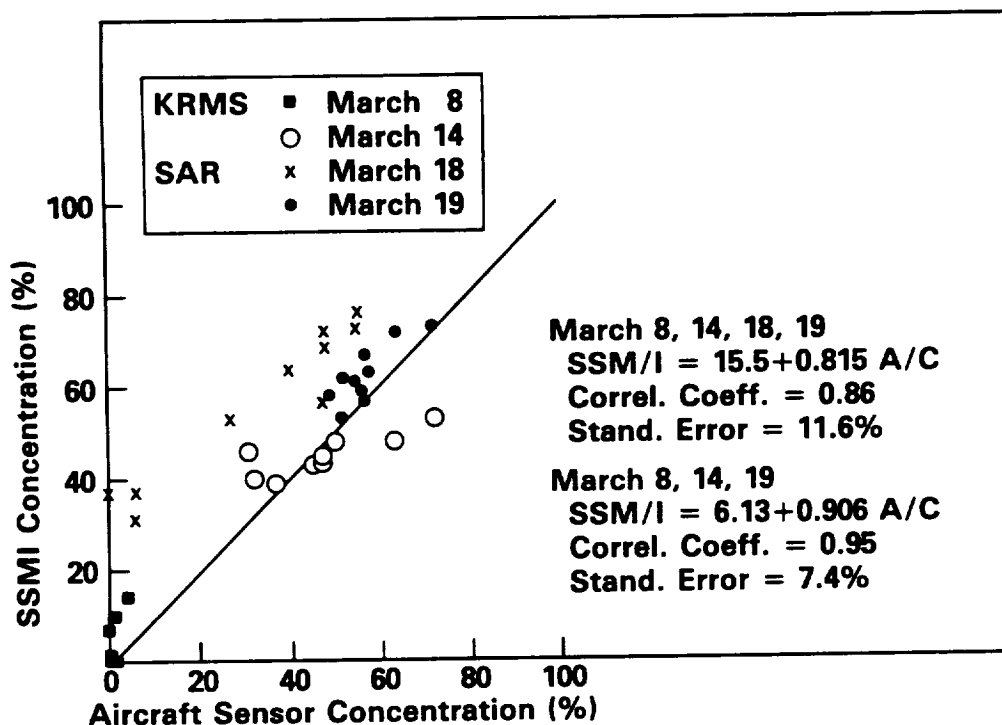


Figure 10.1. Comparison of MY sea ice concentrations derived from SSM/I radiances using the NASA Team algorithm and from airborne active- and passive-microwave sensors.

Examination of Arctic MY ice-concentration maps shows low (generally less than 20-25%) concentrations in areas known to be free of MY ice, for example, as in the Bering Sea and Baffin Bay regions. These false indications of MY ice may result from the same effect as that causing the false concentrations in the FY ice regions of the Chukchi Sea discovered in the KRMS-SSM/I comparisons for March 8 and in the AMMR-KRMS comparisons for March 11. For March 11, the AMMR data from the poleward portion of the region of first-year ice off the Alaskan coast show a 5-8 K drop in TB at 37-GHz V-pol., but not at 18 GHz. A similar drop in TB was also observed in the KRMS imagery for both the March 11 and March 8 flights. In both cases where a drop in TB occurred, the KRMS imagery showed an area of older FY ice with presumably an aged snow cover. We speculate that the older snow cover has larger grains, resulting

in greater volume scattering of the upwelling short-wavelength microwave radiation. This selective scattering results in a more negative spectral gradient ratio (GR) and thus tends to mimic the GR value of MY ice.

An algorithm sensitivity analysis shows that a decrease of 10 K in the 37.0-GHz V-pol. TB results in a 28% increase in the MY concentration and a 1.5% increase in total ice concentration. These results are consistent with the observed changes in the AMMR data and in the KRMS imagery, although increases of up to 8% in total ice concentration have been observed (see Chapters 8 and 9).

Finally, a comparison of MY ice concentrations in the Beaufort Sea ice pack derived from the NASA DC-8 SAR and AMMR data sets showed that the average difference of over 800 samples was 6% and the standard deviation of the differences was 14%, results consistent with the KRMS and NADC comparisons. The over-all measure of MY ice concentration accuracy from the direct comparisons between the SSM/I and the aircraft concentrations is taken as 11%, which is one standard deviation using all four aircraft flights. The observed 20% to 25% error in areas of the Bering Sea and Baffin Bay falls within approximately two standard deviations.

## 10.2 Recommendations

Based both on the results of the NASA multisensor validation effort and on user-community feedback, several algorithm problems have been identified and, in some cases, quantified. These problems arise from two basic sources of error. The first source is the sensitivity of the SSM/I at 19.35 GHz to atmospheric water vapor. As noted in Chapter 4, the algorithm weather filter is less effective for the SSM/I than it was for the Nimbus 7 SMMR because the SSM/I 19.35-GHz channels are closer to the peak of the 22.2-GHz water-vapor line. During winter, the weather-related errors are most pronounced at low latitudes, but are serious at all latitudes during summer. The second source of error results from the inability of the algorithm to distinguish more than two radiometrically different sea ice types or ice-surface conditions. In order of importance, the major algorithm errors are

- 1) False indications of sea ice over open ocean and near the ice edge at high latitudes during summer resulting primarily from the microwave emission of atmospheric water vapor.
- 2) Negative biases in sea ice concentration resulting from the presence of new and young sea ice types. Negative biases as large as 25% have been observed in the Bering Sea.
- 3) False indications of multiyear-ice concentration resulting from a deep or aged snow cover and from variable surface conditions resulting in negative GRs on FY ice. Errors of up to 25% in MY-ice concentration and a few percent in total ice concentration have been observed locally near shore.
- 4) Underestimates in summer-ice concentration resulting from the presence of melt ponds. Other summer melt conditions include moist snow covers and nonlinearities in surface emissivity when temperatures are near the melt point. The Landsat summer comparisons were inconclusive because of problems with ice drift. Clearly, additional validation studies are needed to provide a measure of algorithm accuracy under summer melt conditions.

It is strongly recommended that a focused effort be made to address these problems, using existing data sets and, if needed, newly acquired field and laboratory data. There is potential for reducing some of these errors through the use of additional SSM/I channels, and the combined SSM/I and ERS-1 SAR spaceborne observations which have recently become available. Specifically, techniques are needed to

- improve the ice-weather discrimination capability of the algorithm. Use of the SSM/I 22.2-GHz channel in the algorithm may lead to the needed improvement.
- correct the low-concentration bias resulting from the presence of new and snow-free young ice types. A spin-off of this work is likely to be an algorithm to map areas of new ice production.

- discriminate between snow-cover effects on FY ice and actual FY-MY ice-type variations. A focused effort is needed to study the variation in TB over FY ice as a snow cover accumulates and ages. Additional validation studies of multiyear ice are needed to understand more fully the variability of this parameter in other regions of the Arctic.
- differentiate unambiguously between melt ponds and open-water areas during summer. Progress here will be made through the development of synergistic active/passive algorithms. Additional validation studies are needed during summer in both hemispheres.

Work is under way in the sea ice community to develop the techniques needed to make these improvements. In addition, totally new approaches in sea ice-algorithm development are being explored. One such approach uses the traditional "snap-shot"-type algorithm, together with information on the time history of the ice cover. Computer models used in conjunction with multisensor data sets, hopefully, will provide an improved set of ice parameters from satellite observations.

Finally, in anticipation of improved and new algorithms, the question of changing algorithms is an important one. In December 1985, the NASA Sea Ice Algorithm Working Group developed a set of ground rules for modifying or replacing sea ice algorithms for the SSM/I. The ground rules, which are summarized in the NASA Sea Ice and Snow Validation Plan for the Defense Meteorological Satellite Program Special Sensor Microwave Imager (Cavalieri and Swift, 1987), are based on the philosophy that a substantial improvement in the sea ice products would have to be proven to justify changing the algorithm. Arbitrary changes or changes for little scientific gain only serve to disrupt what is probably the most useful tool: the continuous, long-term time series of global sea ice measurements.

### 10.3 References

- Cavalieri, D. J., and C. T. Swift, *NASA Sea Ice and Snow Validation Plan for the Defense Meteorological Satellite Program Special Sensor Microwave Imager SSM/I*, NASA Technical Memorandum 100683, National Aeronautics and Space Administration, Goddard Space Flight Center, Greenbelt, MD, September 1987.
- Hollinger, J., *DMSP Special Sensor Microwave Imager Calibration/Validation*, Final Report Volume 1, 20 July 1989, Naval Research Laboratory, Washington, D.C.



## **APPENDIX A**

### **Geolocation Correction Software - PIXFIX**

**Mark Goodberlet and Calvin T. Swift  
Department of Electrical and Computer Engineering  
University of Massachusetts  
Amherst, Massachusetts 01003**



```

C   PROGRAM NAME: PIXFIX.FOR                LAST UPDATE:15JUL89
C   This short main program shows you how to use the
C   subroutines "PIXFIX" and "DELAC" to correct the
C   LAT/LON associated with the SSM/I footprints.
C
C   CHARACTER HEADER*10,FIN*10,FOUT*10
C   REAL ALT2(128),ALN2(128)
C
C   REAL ALAT(128),ALON(128),DELA(128,9),DELC(128,9) !XLL common block
C   COMMON/XLL/DELA,DELC,ALAT,ALON,ICALL             !XLL common block
C
C   WRITE(6,1000)
1000  FORMAT(/' ENTER INPUT FILE NAME: ', $)
      READ(5,1010)FIN
1010  FORMAT(A10)
      WRITE(6,1020)
1020  FORMAT(/' *****'
&      ' ** CORRECTION IS VALID ONLY FOR DATA FROM **'
&      ' ** THE TIME PERIOD 1JUL87 (JULIAN DAY 152)**'
&      ' ** THROUGH 31MAR89 ( JULIAN DAY 90). **'
&      ' *****'//
&      ' ENTER JULIAN DAY AND YEAR OF THIS DATA',
&      ' FILE(eg. 191 88): ', $)
      READ(5,*)JDAY,IYR
      WRITE(6,1030)
1030  FORMAT(/' ENTER OUTPUT FILE NAME: ', $)
      READ(5,1010)FOUT
C
C   SPECIFY SCAN TYPE AND VARIABLE ICALL
C
C   ITYPE = 2
C   ICALL = 0
C
C   OPEN(UNIT=1,STATUS='OLD',NAME=FIN)
C   OPEN(UNIT=10,STATUS='NEW',NAME=FOUT)
C   READ(1,1010)HEADER
C   READ(1,1010)HEADER
C   WRITE(10,1040)
1040  FORMAT(' OUTPUT FROM PROGRAM PIXFIX.FOR'
&      ' (ORIG LAT/LON) (CORRECT LAT/LON) PIX')
      DO 10 I=1,64
          READ(1,*)ALAT(I),ALON(I)
          ALT2(I)=ALAT(I)
          ALN2(I)=ALON(I)
      10  CONTINUE
          CALL PIXFIX(ITYPE,IYR,JDAY,IERR)
          WRITE(6,1050)IERR
1050  FORMAT(' ERROR FLAG=',I2)
      DO 20 I=1,64
          WRITE(10,1060)ALT2(I),ALN2(I),ALAT(I),ALON(I),I
      20  CONTINUE
1060  FORMAT(' ',4(F7.2,X),I4)
      STOP
      END

```

PRECEDING PAGE BLANK NOT FILMED

**A2** INTENTIONALLY BLANK

```

C *****
C * SUBROUTINES FOLLOW *
C *****
C SUBROUTINE PIXFIX(ITYPE,IYR,JDAY,IERR)
C *****
C * SUBROUTINE USED TO CORRECT THE LAT/LON VALUES *
C * ASSOCIATED WITH PIXELS OF THE SSM/I SCAN *
C *
C * LAST UPDATE: 13 APRIL 1988 *
C *
C * DEVELOPED AT: *
C * MICROWAVE REMOTE SENSING LABS *
C * MARCUS HALL *
C * UNIVERSITY OF MASSACHUSETTS *
C * AMHERST, MA 01003 *
C *
C * POC: CALVIN SWIFT OR MARK GOODBERLET *
C * OMNET ==> C.SWIFT *
C * PHONE ==> (413) 545-4675 *
C *****
C
C ==> INSTRUCTIONS FOR USE: <==
C * LOAD COMMON BLOCK ARRAYS ALAT(.) AND ALON(.) WITH THE
C LAT/LON PAIRS CORRESPONDING TO THE PIXELS IN A SINGLE
C SSM/I SCAN
C
C * SPECIFY ITYPE, ICALL, IYR AND JDAY (DESCRIBED BELOW)
C
C * SUBROUTINE WILL CALCULATE THE CORRECTED LAT/LONS AND PLACE THEM
C IN THE ARRAYS ALAT(.) AND ALON(.)
C
C ==> VARIABLE DESCRIPTIONS:<==
C ALAT(.)=> ARRAYS WHICH ARE USED TO STORE THE UNCORRECTED AND
C ALON(.) CORRECTED VALUES OF LATITUDE AND LONGITUDE FOR THE
C PIXEL IN THE SSM/I SWATH.
C LATITUDE RANGE = (-90,90)
C LONGITUDE RANGE = (0,360) EAST
C
C ICALL ==> A VARIABLE WHICH IS USED TO DETERMINE WHETHER
C THIS IS THE FIRST TIME THE MAIN PROGRAM HAS CALLED
C THIS SUBROUTINE. ONLY ON THE FIRST CALL WILL
C THE SUBROUTINE "DELAC" WILL BE CALLED WHICH FILLS THE
C CROSS-SCAN AND ALONG-SCAN CORRECTION ARRAYS CALLED
C DELA( ) AND DELC( ). USER SHOULD INITIALLY SET ICALL
C EQUAL TO ZERO IN THE MAIN PROGRAM.
C
C IERR ==> VARIABLE CONTAINING ERROR FLAG.
C 1 ==> ERROR IN PROCESSING. USER IS CAUTIONED ABOUT
C USING THE CORRECTED LAT/LON OF THIS SCAN
C 0 ==> SUCCESSFUL COMPLETION OF SUBROUTINE PIXFIX
C
C ITYPE ==> SWATH TYPE. 1 = SDR (PIXELS 2 THRU 63)
C 2 = TDR (PIXELS 1 THRU 64)
C 3 = SDR (PIXELS 2 THRU 127, 85 GHZ)

```

```

C                                     4 = TDR (PIXELS 1 THRU 128, 85 GHZ)
C
C
C   IYR   ==> YEAR OF THE DATA (ie. 87 or 88)
C
C   JDAY  ==> JULIAN DAY OF THE DATA
C
C   APITCH ==> SSMI PITCH ANGLE IN DEGREES
C
C   AYaw  ==> SSMI YAW ANGLE IN DEGREES
C
C   AROLL ==> SSMI ROLL ANGLE IN DEGREES
C
C   INTEGER BEGPIX(4),ENDPIX(4)
C   REAL DIST1(4),DIST2(4)
C
C   REAL ALAT(128),ALON(128),DELA(128,9),DELC(128,9) !XLL common block
COMMON/XLL/DELA,DELC,ALAT,ALON,ICALL                !XLL common block
C
C   DATA R/6371./,PI/3.1415927/,BEGPIX/2,1,2,1/,ENDPIX/63,64,127,128/
C   DATA DIST1/20.,20.,10.,10./,DIST2/30.,30.,15.,15./
C   IERR = 1
C   IF(ICALL .EQ. 1)GO TO 30
C
C   C
C   FILL THE CORRECTION ARRAYS ON FIRST CALL TO THIS SUBROUTINE
C
C   IF(IYR.LT.87)JDAY=JDAY-365
C   IF(IYR.GT.87)JDAY=JDAY+365
C   IF(IYR.GT.88)JDAY=JDAY+366
C   IF(JDAY.GT.151.AND.JDAY.LT.456)GO TO 10
C   WRITE(6,1030)
1030  FORMAT(////////'*** CORRECTION IS NOT VALID',
&      ' FOR THIS TIME PERIOD ***')
C   RETURN
10  CONTINUE
C   DO 20 ILAT=1,9
C   XLAT=(ILAT-1)*10.+5.
C   CALL PYR(JDAY,XLAT,APITCH,AYAW,AROLL)
C   CALL DELAC(ITYPE,APITCH,AYAW,AROLL,ILAT)
20  CONTINUE
30  CONTINUE
C
C   SPECIFY WHICH COLUMNS OF THE CORRECTION ARRAYS ARE TO BE USED
C
C   ILAT=1+ABS(INT(ALAT(ENDPIX(ITYPE)/2)/10.))
C
C   DO 100 I=BEGPIX(ITYPE),ENDPIX(ITYPE),2
C   IP1 = I+1
C
C   CONVERT LAT/LON FROM DEGREES TO RADIANS
C
C   ALAT(IP1) = ALAT(IP1)*PI/180.
C   ALAT(I) = ALAT(I)*PI/180.
C   ALON(IP1) = ALON(IP1)*PI/180.
C   ALON(I) = ALON(I)*PI/180.

```

```

C
C COMPUTE COMPONENTS OF THE ALONG-SCAN DIRECTION VECTOR
C
      VA = R*(ALAT(IP1)-ALAT(I))
      HA = R*COS(ALAT(I))*(ALON(IP1)-ALON(I))
      XMAG = SQRT(VA*VA+HA*HA)
C
C NORMALLY THE VALUE OF XMAG WILL BE ABOUT 25 (12.5 FOR 85GHZ) KILOMETERS
C WHICH IS THE DISTANCE BETWEEN SSMI PIXELS. IF THIS IS NOT TRUE THEN
C EITHER THE LAT/LON DATA IS BAD (IN WHICH CASE THE ERROR FLAG, IERR,
C IS SET AND THE PROGRAM RETURNS CONTROL TO THE MAIN PROGRAM) OR
C THE SWATH HAS PIXELS ON BOTH SIDES OF THE 0/360 LONGITUDE LINE (IN
C WHICH CASE THE CALCULATION CAN BE CORRECTED AS SHOWN BELOW).
C
      IF(XMAG.LT.DIST2(ITYPE) .AND. XMAG.GT.DIST1(ITYPE))GO TO 40
      IF(ALON(I) .LT. PI) ALON(I) = ALON(I)+2.*PI
      IF(ALON(IP1) .LT. PI) ALON(IP1) = ALON(IP1)+2.*PI
      HA = R*COS(ALAT(I))*(ALON(IP1)-ALON(I))
      XMAG = SQRT(VA*VA+HA*HA)
      IF(XMAG.GT.DIST2(ITYPE) .OR. XMAG.LT.DIST1(ITYPE))RETURN
40  CONTINUE
      DO 50 J=1,2
      JI = J+I-1
      DTHET = (DELA(JI,ILAT)*VA-DELC(JI,ILAT)*HA)/(R*XMAG)
      DPHI = DELA(JI,ILAT)*HA+DELC(JI,ILAT)*VA
      DPHI = DPHI/(R*COS(ALAT(JI))*XMAG)
C
C CALCULATE NEW LAT/LONS AND CONVERT BACK TO DEGREES
C
      ALAT(JI) = (ALAT(JI)+DTHET)*180./PI
      ALON(JI) = (ALON(JI)+DPHI)*180./PI
C
C CHECK FOR LONGITUDES THAT ARE OUT OF (0,360) RANGE
C
      IF(ALON(JI) .LT. 0.0 )ALON(JI)=ALON(JI)+360.
      IF(ALON(JI) .GT. 360.)ALON(JI)=ALON(JI)-360.
50  CONTINUE
100 CONTINUE
      IERR = 0
      RETURN
      END
C
      SUBROUTINE DELAC(ITYPE,APITCH,AYAW,AROLL,ILAT)
C *****
C * SUBROUTINE USED TO FILL THE CROSS-SCAN AND ALONG- *
C * SCAN CORRECTION ARRAYS, DELC(.) AND DELA(.). *
C * * *
C * LAST UPDATE: 13 APRIL 1988 *
C * * *
C * DEVELOPED AT: *
C * MICROWAVE REMOTE SENSING LABS *
C * MARCUS HALL *
C * UNIVERSITY OF MASSACHUSETTS *
C * AMHERST, MA 01003 *

```

```

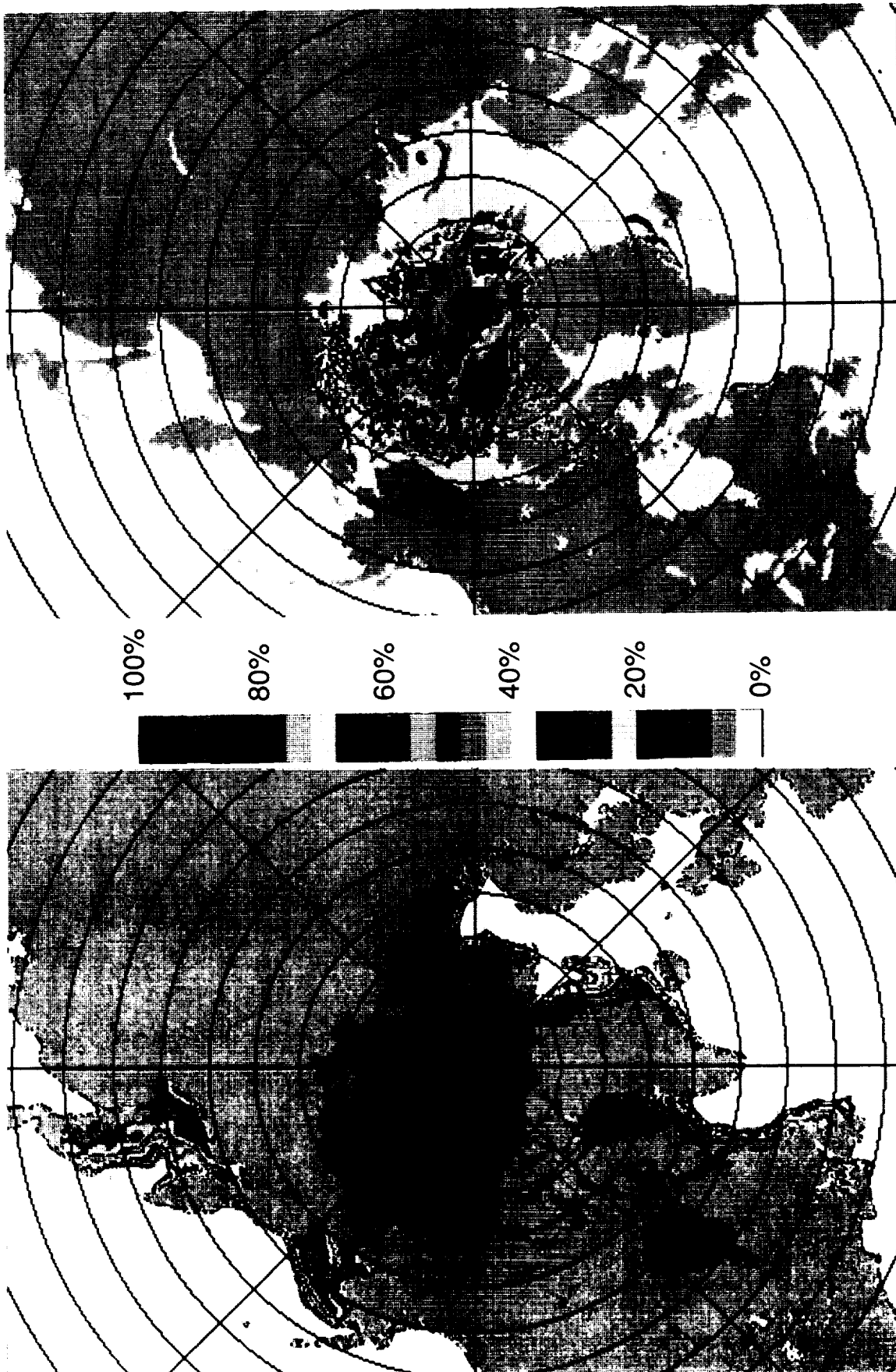
C  *
C  *      POC: CALVIN SWIFT OR MARK GOODBERLET
C  *      OMNET ==>  C.SWIFT
C  *      PHONE ==>  (413) 545-4675
C  *
C  *****
C
C  ==> VARIABLE DESCRIPTIONS <==
C      APITCH  = PITCH ANGLE IN DEGREES
C      AYAW    = YAW ANGLE IN DEGREES
C      AROLL   = ROLL ANGLE IN DEGREES
C      C_TRACK = CROSS-TRACK SHIFT OF SCAN AXIS IN KILOMETERS
C      A_TRACK = ALONG-TRACK SHIFT OF SCAN AXIS IN KILOMETERS
C      R       = EARTH RADIUS IN KILOMETERS
C      H       = SSM/I ALTITUDE ABOVE EARTH IN KILOMETERS
C      NPIX    = NUMBER OF PIXELS IN THE SSM/I SCAN
C      ILAT    = VARIABLE INDICATING IN WHICH COLUMN OF DELC(.,.)
C               AND DELA(.,.) THE CALCULATED CORRECTIONS ARE
C               TO BE STORED
C      DELC(N,I)= CROSS-SCAN SHIFT(KILOMETERS) OF PIXEL "N"
C                 FOR LATITUDE RANGE (10(I-1),10(I))
C      DELA(N,I)= ALONG-SCAN SHIFT(KILOMETERS) OF PIXEL "N"
C                 FOR LATITUDE RANGE (10(I-1), 10(I))
C      ITYPE   = SWATH TYPE
C                 1,2 ==> 64 PIXEL SWATH
C                 3,4 ==> 128 PIXEL SWATH (85GHZ)
C
C      REAL ALAT(128),ALON(128),DELA(128,9),DELC(128,9) !XLL common block
C      COMMON/XLL/DELA,DELC,ALAT,ALON,ICALL              !XLL common block
C
C      DATA PI/3.1415927/,R/6371./,H/833./
C      NPIX=64
C      IF(ITYPE.GT.2)NPIX=128
C
C      PROGRAM WAS ORIGINALLY DESIGNED TO CALCULATE CROSS-SCAN AND
C      ALONG-SCAN SHIFTS DUE TO SPACECRAFT TRANSLATIONS ALONG OR
C      ACROSS THE GROUND TRACK.  THE OPTION IS STILL AVAILABLE BUT IS NOT
C      BEING USED IN THIS VERSION WHICH IS WHY C_TRACK AND A_TRACK ARE
C      SET EQUAL TO ZERO BELOW.
C
C      C_TRACK=0.0
C      A_TRACK=0.0
C
C      CONVERT ANGLES FROM DEGREES TO RADIANS
C
C      THP=APITCH*PI/180.
C      THY=AYAW*PI/180.
C      THR=AROLL*PI/180.
C
C      CALCULATE ANGULAR SHIFTS CORRESPONDING TO A_TRACK AND C_TRACK
C
C      THA=A_TRACK/R
C      THC=C_TRACK/R
C

```

```

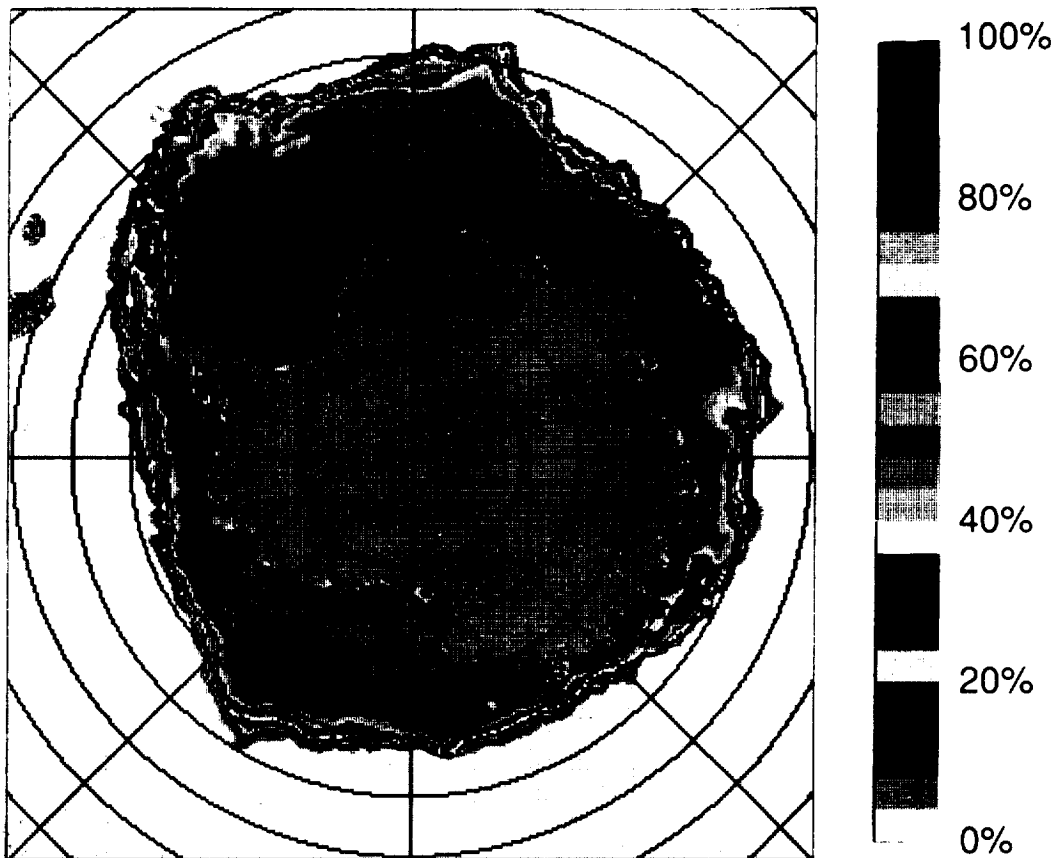
C  SSMI CONE HALF-ANGLE = 45 DEGREES
C
    THVII=45.*PI/180.
    CTVII=COS(THVII)
    STVII=SIN(THVII)
C
C  SCAN SECTOR OF SSMI IS 102.4 DEGREES (FROM 128.8 DEGS TO 231.2 DEGS)
C
    ASCAN=102.4*PI/180.
    APIX=ASCAN/127.
    IF(NPIX.EQ.64)APIX=2.*APIX
    PHVII=PI-ASCAN/2.
    DO 10 I=1,NPIX
        CPVII=COS(PHVII)
        SPVII=SIN(PHVII)
        T1=(1.+H/R)*CTVII
        T2=SQRT(1.-((1.+H/R)*STVII)**2)
        P0=R*(T1-T2)
        ALPH=1.-(R+H)*CTVII/P0
        GAMM=1.-(R+H)/(P0*CTVII)
        DTHET=-(ALPH*THA-THP)*CPVII-(ALPH*THC+THR)*SPVII
        DPHI=(THR+GAMM*THC)*CPVII+(THP-GAMM*THA)*SPVII
        DPHI=THY-DPHI*CTVII/STVII
        ST=SIN(THVII+DTHET)
        CT=COS(THVII+DTHET)
        T1=(1.+H/R)*CT
        T2=SQRT(1.-((1.+H/R)*ST)**2)
        DELC(I,ILAT) = -R*(T1/T2-1.)*DTHET
        DELA(I,ILAT) =  R*(T1-T2)*ST*DPHI
        PHVII=PHVII+APIX
10  CONTINUE
    ICALL = 1
    RETURN
    END
C
    SUBROUTINE PYR(JDAY,XLAT,PITCH,YAW,ROLL)
C  SUBROUTINE USED TO CALCULATE THE VALUES OF THE PITCH
C  YAW AND ROLL ANGLES (DEGREES).
C  ** CALCULATIONS VALID ONLY FROM JULY 87 THRU MARCH 89 **
C  ** ASSUMES THAT SOUTHERN HEMI IS MIRROR IMAGE OF NORTH**
    REAL P(4),Y(4),R(4)
    DATA P/-1.551,0.00549,0.0040,-0.0000078/
    DATA Y/0.395,0.0012,-0.0029,-0.0000020/
    DATA R/0.204,-0.00277,0.00300,0.0000046/
C
    XL=ABS(XLAT)
    PITCH=P(1)+P(2)*JDAY+P(3)*XL+P(4)*JDAY*JDAY
    YAW=Y(1)+Y(2)*JDAY+Y(3)*XL+Y(4)*JDAY*JDAY
    ROLL=R(1)+R(2)*JDAY+R(3)*XL+R(4)*JDAY*JDAY
    RETURN
    END

```



Arctic monthly mean maps of total and multiyear sea ice concentration derived from DMSP SSM/I radiances for March 1988.

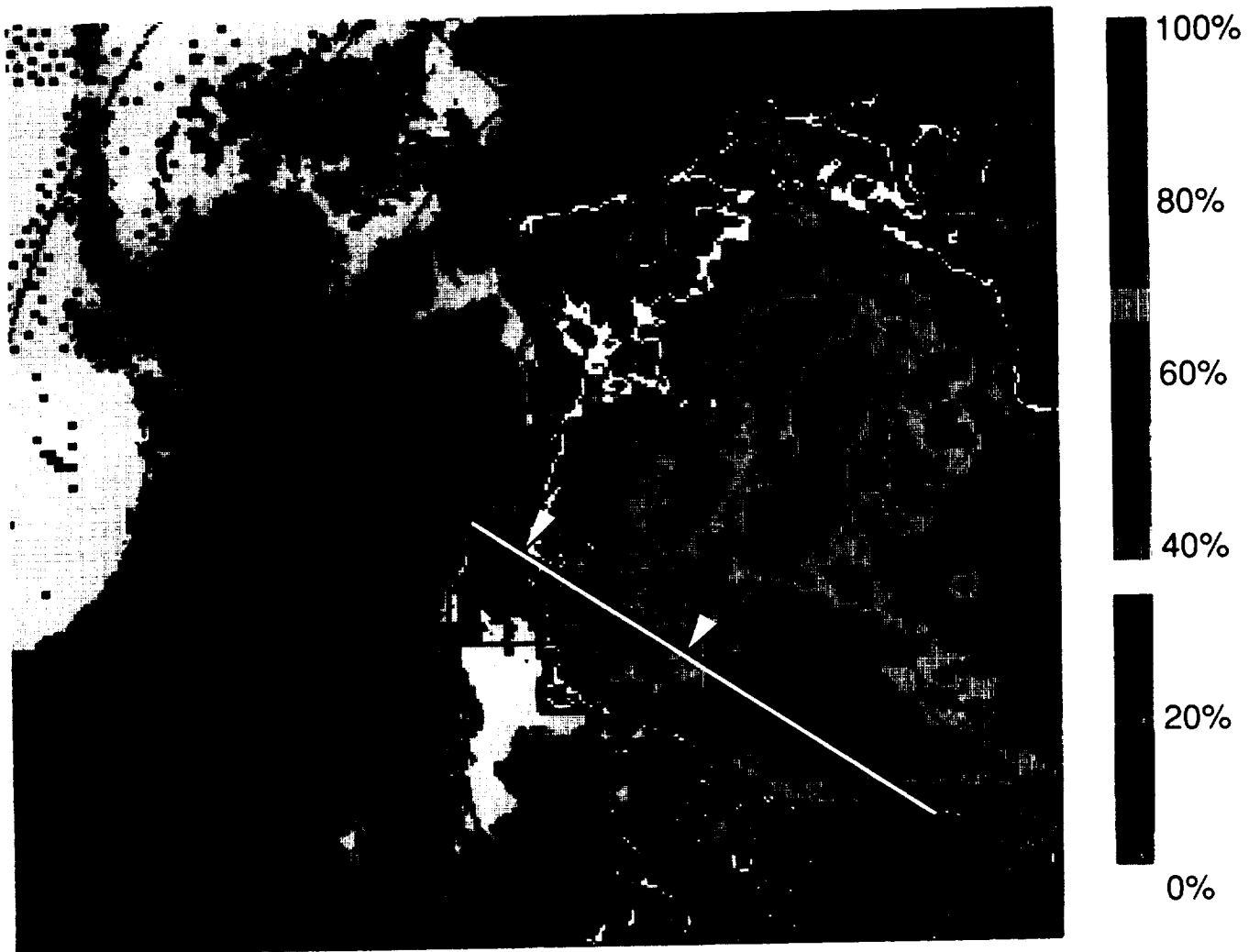




Antarctic monthly mean map of total sea ice concentration  
derived from DMSP SSM/I radiances for September 1987.

ORIGINAL PAGE  
COLOR PHOTOGRAPH

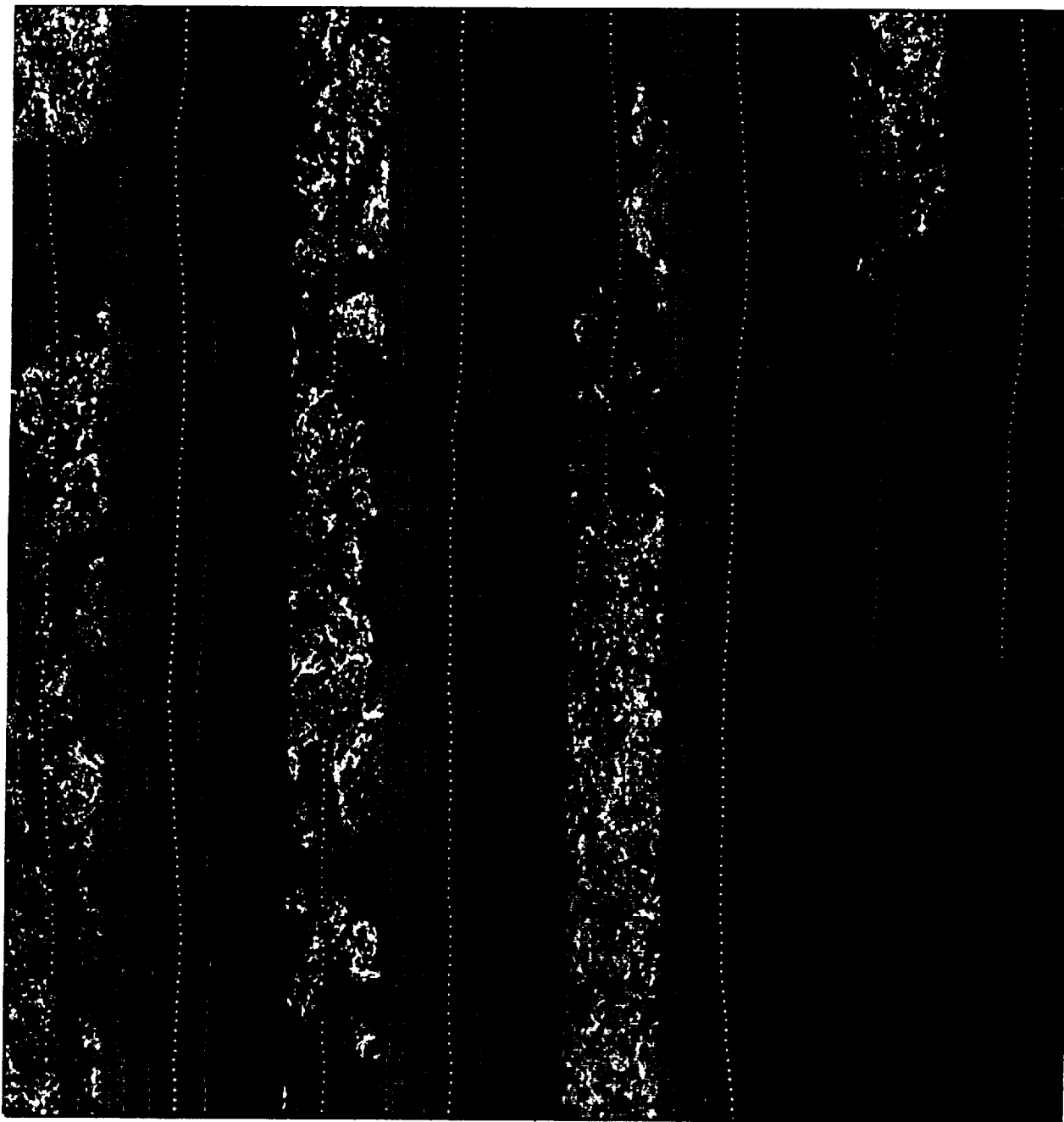




DMSP SSM/I multiyear ice-concentration map showing the outbound leg of the NASA DC-8 flight track for March 11, 1988. Arrowheads mark the transition from first-year ice to a region of mixed first-year and multiyear ice and the transition from the mixed region to a region of high multiyear ice concentration.

OPPOSITE PAGE  
COLOR PHOTOGRAPH





JPL C-band SAR images for a portion of the March 11 Beaufort Sea flight track illustrated in Plate 3. The small crosses indicate the position of the center of the AMMR footprint and the numerical value to the right of each image is the brightness temperature value times ten for the 37-GHz V channel. The colorized image shows multiyear ice as red and first-year ice as blue.

